Faculté des bioingénieurs

Mapping and monitoring seagrass meadows in Seychelles using Sentinel-2 imagery: Model training at Anse-aux-Pins and transferability to nearby lagoons

Auteur	Peugeot Mattis
Promoteur	Hanert Emmanuel (ELIE)
Co-promoteur	Culot Alexis (ELIE)
Lecteurs	Delhez Baptiste (ELIE)
	Harlay Jérôme (BERI)

Année académique 2025-2026

Mémoire de fin d'études présenté en vue de l'obtention du diplôme de Bioingénieur: Chimie et Bioindustries

Acknowledgements

I would first like to thank Emmanuel Hanert, my thesis supervisor, for his guidance, availability and support throughout this year. Thank you for always listening, for your good advice and for helping me move forward during the different steps of this thesis.

I also want to thank Alexis Culot, my co-supervisor, for his help, patience and enthusiasm. Thank you for always being easy to contact, for your advice and for the positive atmosphere you brought during the year.

I also sincerely thank Jérôme Harlay, my main contact in Seychelles, for his availability, time and kindness, but especially for giving me the opportunity to work on this subject. His help and local knowledge were very valuable for this work.

I am also grateful to Quinten Vanhellemont, the creator of ACOLITE, for the useful advice he gave me by email. I really appreciated his clear explanations, his kindness and his willingness to help.

I would also like to thank the whole SLIM team for their advice, help and good mood throughout the year. Thank you for always being available and for making the laboratory a pleasant place to work. I would also like to thank all the people at the ELIE department who helped me get through this year in the best possible conditions.

A big thank you to all the other thesis students who shared this year with me. Thank you for the working sessions, the discussions, the help, the laughs and the memes. This year would not have been the same without you guys.

I would also like to thank my colleagues at IKEA for their understanding, energy, good mood and humor during this busy period. Thank you for always showing interest in my thesis, for asking how it was going even when the subject was not always easy to explain and for encouraging me during the more difficult moments.

I also would like to thank my friends and my volleyball teammates for their support, presence and encouragement during this year. Thank you for the moments outside the thesis and especially for helping me take breaks and for reminding me that there was also life outside this work.

A very special thank you to Aurélie and Newton. Thank you for being by my side every day, for your love, patience and support. Thank you for helping me keep balance during this intense year, for being there during the stressful moments and for making the good moments even better. I would not be the person I am today without you two.

Finally, I want to thank my family for their absolute support throughout my studies. Thank you for always believing in me, for encouraging me in the difficult moments and for giving me this invaluable chance to follow my path. I know that I would not have reached this point without you all.

Distribution of contributions

CRediT role	Mattis Peugeot	Other contributor(s)	Artificial intelligence
Conceptualization	X	Emmanuel Hanert and Alexis Culot: guidance on research framing and objectives; Jérôme Harlay: local context and relevance of the Seychelles study area	ChatGPT: support for clarifying research questions and structuring ideas
Methodology	X	Emmanuel Hanert, Alexis Culot and Jérôme Harlay: methodological guidance; Quinten Vanhellemont: technical advice on ACOLITE processing	ChatGPT: assistance with coding, debugging, code structuring and interpretation of error messages. All scripts were reviewed, adapted and executed by the author; DeepL/DeepL Write: language support
Investigation	X	Jérôme Harlay: local knowledge and contextual information; SLIM team: practical and technical advice	Limited use: assistance in organizing workflows and checking scripts
Formal analysis	X	Emmanuel Hanert and Alexis Culot: advice on interpretation and analysis	ChatGPT: Python/script assistance, debugging, figure creation support
Validation	X	Emmanuel Hanert and Alexis Culot: feedback on validation strategy and interpretation of model results	ChatGPT: support for checking consistency of validation procedures and explaining metrics
Writing - original draft	X	Louis Didier (Mat&Met), Julien Monfils (Intro), Emmanuel Hanert: scientific feedback on structure and content	ChatGPT: language support, reformulation; DeepL and DeepL Write: translation, grammar and English style support
Writing - review and editing	X	Emmanuel Hanert: comments, corrections and scientific feedback	ChatGPT: grammar, clarity, reformulation, shortening expanding text; DeepL/DeepL Write: English correction and translation support
Visualization	X	Emmanuel Hanert, Alexis Culot, Jérôme Harlay: advice on figure readability and scientific presentation	ChatGPT: assistance with plotting scripts, captions checking, readability improvements and wording
Supervision		Emmanuel Hanert: supervisor; Alexis Culot: co-supervisor	/

The contributions reported above follow the CRediT contributor role taxonomy. The thesis work was primarily carried out by the author, including the processing of Sentinel-2 data, implementation of the analysis workflow, production of results, interpretation of the mapped seagrass dynamics and preparation of the thesis. The supervisor and co-supervisor contributed through scientific guidance, methodological advice, feedback on the interpretation of results and revision of the manuscript. Additional contributors provided local or technical advice when relevant.

Generative artificial intelligence tools were used in support of this thesis. We used ChatGPT for coding support, debugging, section structuring, reformulation, grammar correction, improvement of clarity, captions checking and explaining methodological or analytical concepts. We used DeepL and DeepL Write for translation support, grammar corrections and English style improvements. These tools were used only as assistance tools. The scientific goals, methodological decisions, data processing, analyses, interpretation of results, validation and decisions on the final manuscript were all done by the author. The author is entirely responsible for the content and presentation of the submitted thesis.

Contents

List of Figures

List of Tables

List of Acronyms and Abbreviations

AOI Area of Interest

CV Cross-Validation

DII Depth-Invariant Index

DSF Dark Spectrum Fitting

EEZ Exclusive Economic Zone

EIO Eastern Indian Ocean

ENSO El Niño-Southern Oscillation

ESA European Space Agency

F1 F1-Score

Fmask Function of Mask

FN False Negative

FP False Positive

GCS Geographic Coordinate System

HLS Harmonized Landsat-Sentinel

IOD Indian Ocean Dipole

IQ95 95% Interquantile Range

L1C Level-1 Collection product

L2W Level-2 Water Product

LODO Leave-One-Date-Out

MACCE Ministry of Agriculture, Climate Change and Environment

Macro-F1 Macro-Averaged F1-Score

MSP Marine Spatial Plan

NDWI Normalized Difference Water Index

NICFI Norway's International Climate and Forest Initiative

NIR Near-Infrared

RAdCor Remote Sensing Adjacency Correction

RF Random Forest

Rrs, Rrs_* Remote Sensing Reflectance

S2 Sentinel-2

S2-MSI Sentinel-2 Multispectral Instrument

SeyCCAT Seychelles Conservation and Climate Adaptation Trust

SIDS Small Island Developing States

SST Sea Surface Temperature

SWIR Shortwave Infrared

TN True Negative

TOA Top of Atmosphere

TP True Positive

TSDSF Top-of-Atmosphere Surface Dark Spectrum Fitting

UTM Universal Transverse Mercator

WGS84 World Geodetic System 1984

WIO Western Indian Ocean

XGBoost Extreme Gradient Boosting

1. Introduction

1.1 Seagrasses are a key coastal ecosystem

Seagrasses (*Fig.1)* are marine angiosperms that colonize shallow, well-lit coastal environments across tropical and temperate regions in the world. They form structural complex benthic meadows composed of different species such as *Thalassodendron ciliatum*, *Thalassia hemprichii*, *Cymodocea serrulata*, *Halodule uninervis*, *Halophila ovalis* and *Zostera noltei* (Nordlund et al., 2018; Unsworth et al., 2019). Their root-rhizome system and vascular tissues allow for efficient nutrient transport, strong anchorage in sediments and resilience to hydrodynamic constraints. These characteristics allow seagrasses to act as ecosystem engineers, modifying sediment dynamics, light availability and local hydrodynamics (Orth et al., 2006).

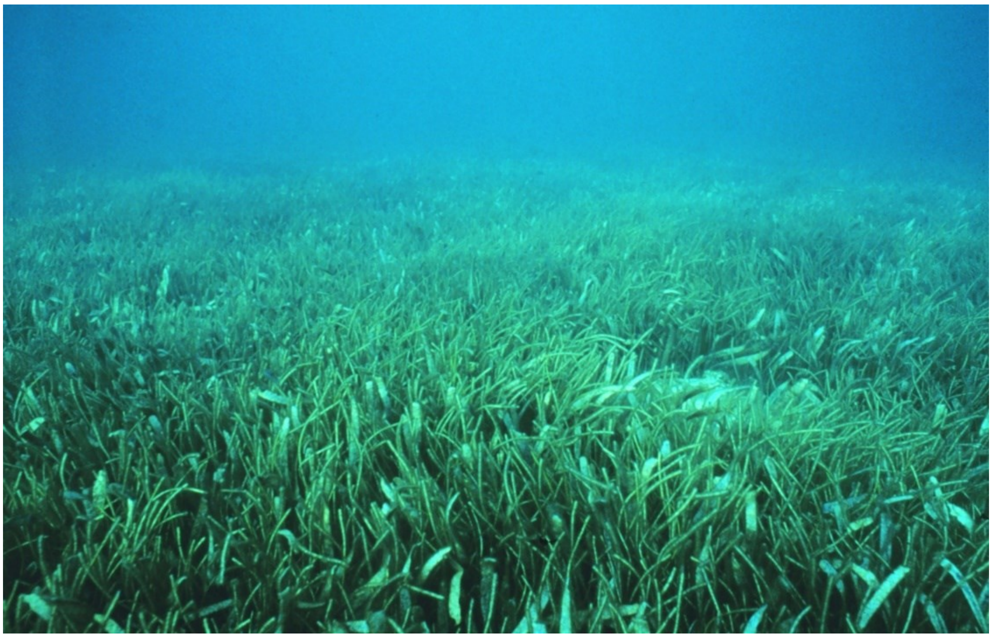

Figure 1 - Coastal waters with a tropical seagrass meadow made up of Thalassia and Cymodocea. In addition to improving water clarity and providing habitat for a variety of marine life, seagrass canopies also trap sediments. Photo: NOAA (public domain). Photographer: Heather Dine

Seagrass ecosystems support ecological processes. Their dense canopies improve water clarity by reducing turbidity, encouraging sediment deposition and attenuating wave energy. By shaping local hydrodynamic conditions and stabilizing sediments, seagrass meadows help maintain stable coastal environments and support adjacent ecosystems such as coral reefs and mangroves. From a biological point of view, seagrass meadows provide key habitat, nursery areas and foraging grounds for a wide variety of taxa, including reef fish, crustaceans, echinoderms and megafauna such as green turtles and dugongs (Nordlund et al., 2018; Unsworth et al., 2019). These functions explain why seagrass ecosystems are often referred to as the pillar of coastal productivity in tropical regions.

Seagrasses are classified as "Blue carbon ecosystems" because of their major contribution to carbon sequestration and storage. Despite covering <0.5% of the seafloor, their high primary productivity and capacity to trap organic matter in anoxic sediments result in significantly high carbon burial rates (Duarte et al., 2005; Fourqurean et al., 2012). According to a number of studies, their capacity to store carbon, over decadal to millennial timescales, can surpass many terrestrial forests (Macreadie et al., 2021). This capacity is especially relevant for small island developing states (SIDS), such as the Seychelles, where terrestrial carbon sinks are limited. These coastal ecosystems therefore contribute strongly to SIDS' carbon budgets (Macreadie et al., 2021).

The UNEP/GRID-Arendal map (*Fig.2*) provides a global view of seagrass distribution, showing that seagrass meadows can be found all over the world. This global presence highlights their ecological importance and their contribution to coastal functioning on all continents. However, the map also shows clear differences in data coverage between regions. Some areas, particularly in the Western Indian Ocean (WIO), show fewer and more scattered seagrass records compared to other parts of the world, indicating that these regions are less well-documented. These gaps suggest historical limitations in field observations and the challenge of regularly monitoring underwater vegetation in areas with little or scarce datasets (GRID-Arendal, 2020).

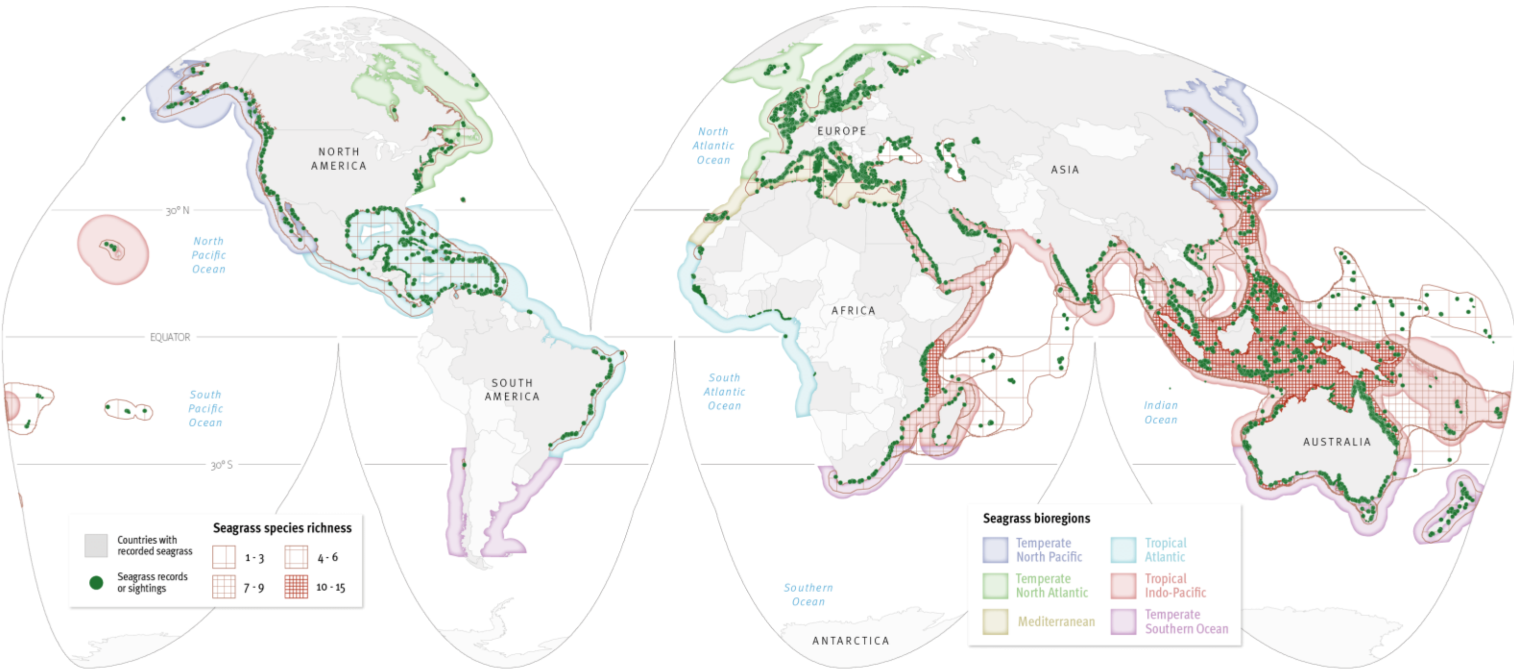

Figure 2 - Global distribution of known seagrass meadows and species richness across bioregions. The map highlights globally uneven reporting, with sizable data gaps in the Western Indian Ocean, including Seychelles. Source: UNEP/GRID-Arendal (CC-BY-NC-SA 3) Cartographer: Hisham Ashkar https://www.grida.no/resources/13590

1.2 Global decline of seagrass ecosystems

Despite their ecological importance and global distribution, seagrass ecosystems have experienced massive decline over the past century. Recent global studies merging historical records and spatial data reveal different regional trajectories, with an overall decrease in seagrass extent observed in most oceans (*Fig.3*) (Duarte et al., 2025).

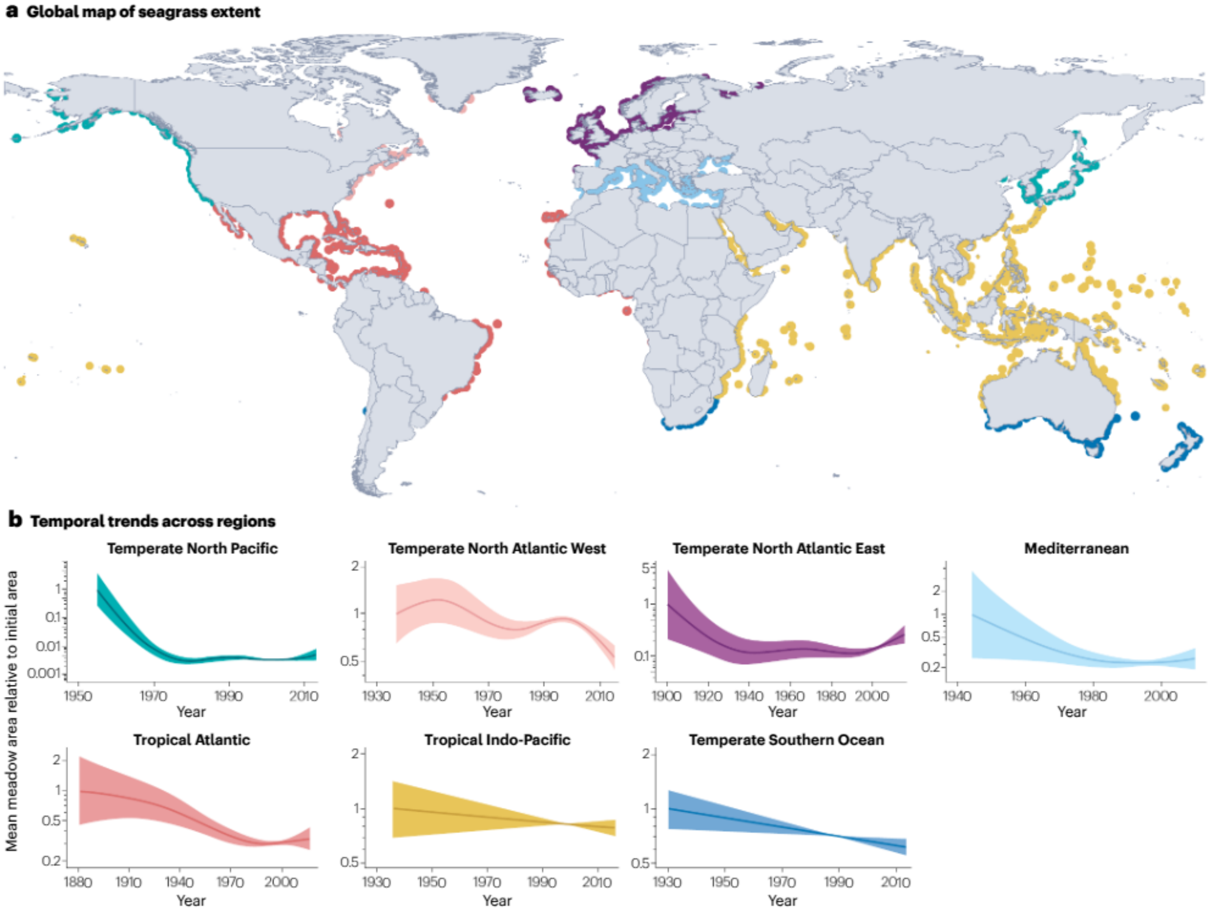

Figure 3 - Seagrass' global distribution and temporal trends. (a) A global map showing the seagrass meadows' spatial distribution across the main oceanic regions. (b) Long-term trends in the mean area of seagrass meadows compared to their initial extent for various biogeographic regions, highlighting both regional variation and a general decrease in seagrass extent over time. Source: Duarte et al. (2025).

Seagrass meadows are threatened by both anthropogenic and climate-related pressures. Although earlier global estimates suggesting losses of ~7% per year (Waycott et al., 2009), recent global studies show that current seagrass decline rates average ~3% annually, with a high local variability that can exceed ~7% (Cavanaugh et al., 2025; IPBES, 2019; Unsworth et al., 2019).

Accordingly, it has been estimated that the cumulative loss of seagrass area worldwide since the 1990s has been ~50% (Duarte et al., 2005; Waycott et al., 2009). More recent multi-decadal studies reported canopy thinning, fragmentation and shifts in species composition, particularly in regions where the quality of the water is continuously declining (Cingano et al., 2024; R.-R. Li et al., 2003).

1.3 Seagrasses in the Seychelles

Seychelles is an archipelago of 115 islands located in the WIO, northeast of Madagascar (*Fig.4*). As a typical SIDS, the country is characterized by a very large Exclusive Economic Zone (EEZ) relative to its land area, making coastal and marine ecosystems particularly important at the national scale. Its position on the Seychelles Plateau, a shallow submarine bank extending over 40,000 km^2, creates large areas of suitable habitat for seagrass development. The archipelago's combination of warm tropical waters, stable light conditions and large shallow lagoons provides favorable conditions for the formation of diverse seagrass communities (Nordlund et al., 2018; Palacios et al., 2021).

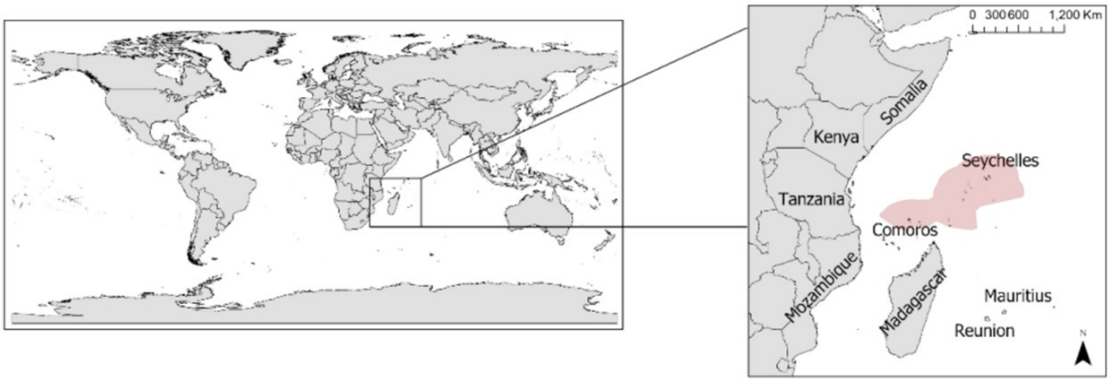

Figure 4 - Location of the Seychelles EEZ (red) within the Western Indian Ocean. The country is situated on the Seychelles Plateau, a large shallow submarine bank that provides extensive areas of suitable habitat for seagrass development. Adapted from (Palacios et al., 2021)

In this context, the Seychelles are home to some of the region's largest seagrass meadows. Recent national-scale mapping using Norway's International Climate and Forest Initiative (NICFI) PlanetScope and Sentinel-2 (S2) imagery (C. B. Lee et al., 2023) revealed large, continuous beds distributed across the plateau, especially around the inner granitic islands (*Fig.5*). The resulting wall-to-wall map shows that seagrass cover in the Seychelles EEZ is considerably larger than previously reported and highlights the ecological importance of these habitats.

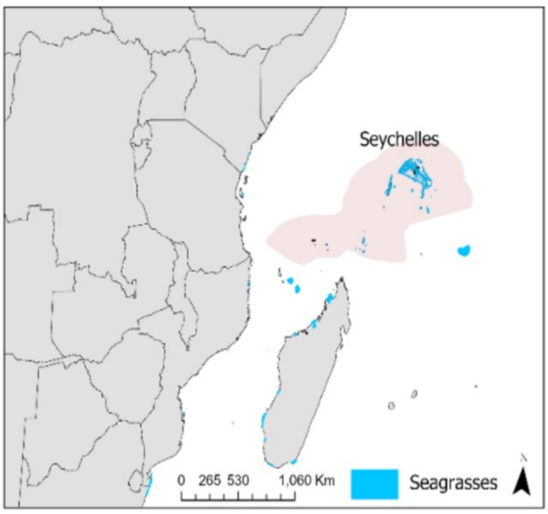

Figure 5 - Distribution of seagrass meadows (Smith et al. 2020, UNEP-WCMC and Short) in the tropical WIO region and Seychelles' EEZ (red) (Global Mangrove Watch, reference year: 2016; Bunting et al. 2018). Adapted from (Palacios et al., 2021)

In addition to their ecological roles, seagrasses are getting more acknowledged for their importance in national climate strategies. The Seychelles Blue Carbon Roadmap (Rowlands et al., 2024) states that seagrass ecosystems store over 95% of the nation's total blue carbon stock. Their big spatial extent and capacity to trap and accumulate organic carbon in sediments over long time periods explain their strong contribution to national carbon stocks (Macreadie et al., 2021).

As a result, seagrass conservation is now closely linked to Seychelles' commitments to climate mitigation, marine spatial planning and biodiversity conservation.

1.4 National framework supporting seagrass monitoring in Seychelles

Seychelles has established a number of national frameworks that offer robust institutional support for monitoring marine habitats, including the seagrass ecosystems. According to Bennett et al. (2024) and the Seychelles Conservation and Climate Adaptation Trust (SeyCCAT) and the Ministry of Agriculture, Climate Change and Environment (MACCE), these frameworks encourage the development of long-term, spatially explicit analyses, which are becoming mandatory for effective marine management.

A key component of this landscape is the Seychelles Marine Spatial Plan (MSP), the first comprehensive MSP in the WIO. The plan organizes the country's 1.37 million km^2 EEZ into a system of spatially designated zones in order to balance biodiversity conservation, sustainable resource use and economic activity (MSPglobal, 2021; Seychelles MSP, 2020). The spatial organization of the MSP provides a national framework within which coastal and marine habitats, including seagrass meadows, can be monitored and managed in a spatially explicit way (*Fig.6*).

In parallel with the MSP, Seychelles has made significant commitments to marine conservation. In 2020, Seychelles achieved a major milestone by protecting 30% of its EEZ as marine protected areas, reaching a national biodiversity target related to the MSP and the earlier debt-for-nature swap (The Nature Conservancy, 2018; Republic of Seychelles, 2020b). These protected areas include large offshore regions and a number of nearshore zones where ecological important habitats like coral reefs and seagrass meadows are taken into account in conservation planning.

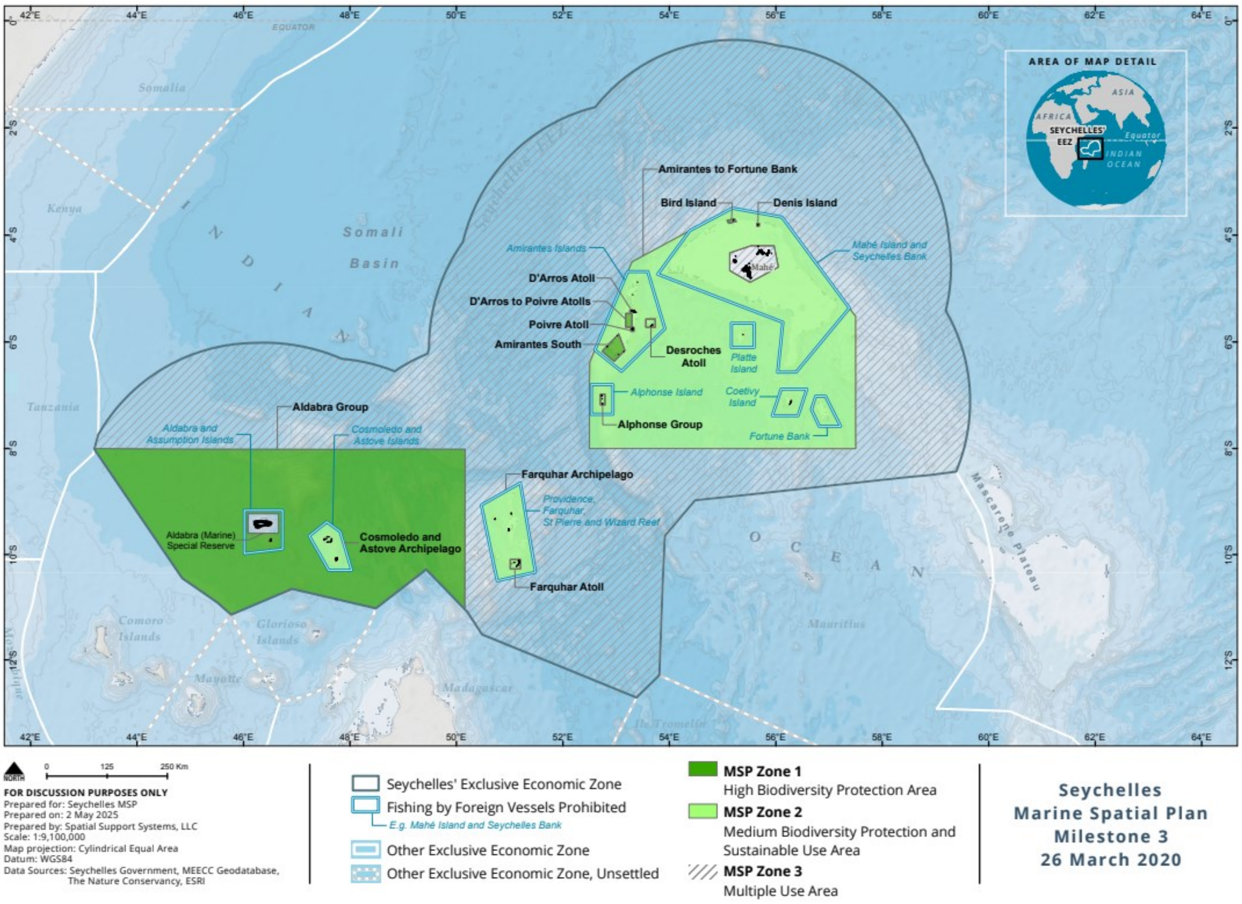

Figure 6 - Zoning of the Seychelles MSP showing the composition of conservation and sustainable-use areas across the 1.37 million km² Exclusive Economic Zone. The MSP enabled Seychelles to achieve its 2020 milestone of designating 30% of the EEZ as protected waters. Map adapted from (Seychelles MSP, 2020), prepared 2 May 2025.

Beyond spatial planning and conservation targets, Seychelles has also played a pioneering role in linking marine conservation to innovative blue-finance and blue-economy initiatives. The 2018 sovereign Blue Bond, developed with support from the World Bank, raised $15 million USD to fund sustainable fishing and marine conservation (March et al., 2024; World Bank, 2018). In parallel, the 2016 debt-for-nature deal redirected part of the national debt service toward marine conservation and allowed the creation of the Seychelles Conservation and Climate Adaptation Trust (Republic of Seychelles, 2020b; SeyCCAT, 2024). These financial processes funds national efforts to increase marine data, monitoring capacity and enhance nature-based solutions (Baker et al., 2023).

Along with these policy developments, several national institutions contribute directly to coastal and marine monitoring. The University of Seychelles, the Seychelles Parks and Gardens Authority and the Seychelles Fishing Authority collaborate with international partners on habitat mapping, biodiversity assessments and coastal monitoring programs (Bennett et al., 2024; SeyCCAT, 2024). The nation's growing capacity to conduct ecological assessments is shown by recent national projects that focused on mapping seagrass and classifying habitats (C. B. Lee et al., 2023; Palacios et al., 2021).

1.5 Seagrass change at Anse-aux-Pins (Mahé)

The Anse-aux-Pins lagoon, located on the eastern coast of Mahé (*Fig.7*), is a typical shallow-water environment of the Seychelles. It forms a long, very shallow bay protected by an offshore reef, where water depth over the lagoon platform is often low enough to walk close to the reef edge at low tide (SeyVillas, 2025). Its location and geomorphological features make it representative of many nearshore habitats across the archipelago. Its sandy substrate and shallow platform make it ideal for the growth of vast seagrass meadows (Palacios et al., 2021).

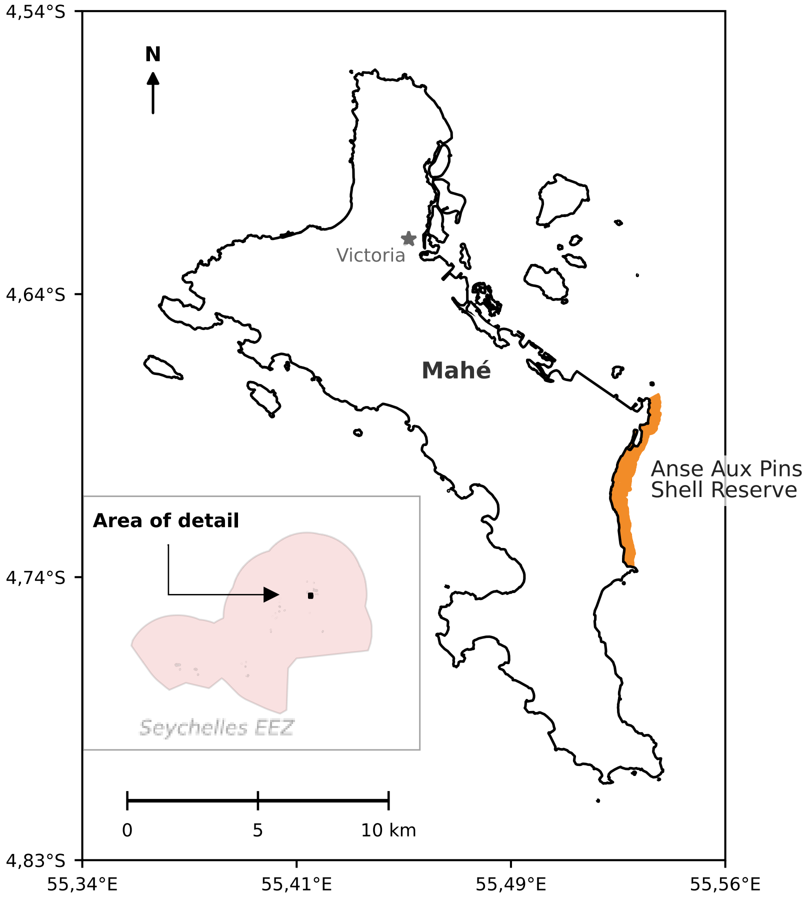

Figure 7 - Location of the Anse-aux-Pins lagoon (orange) on the east coast of Mahé, Seychelles. The site is in the shallow Seychelles Plateau and represents a typical lagoon setting of the inner islands.

In addition, the Anse-aux-Pins Shell Reserve (*Fig. 7*), a local marine reserve covering about 3.3 km^2 was created to preserve coastal habitats and promote sustainable resource use (Republic of Seychelles, 2020a). Although the reserve was first created to protect shellfish, it now includes shallow benthic zones and incorporate the lagoon into Seychelles' larger conservation strategy. Recent national-scale mapping using NICFI PlanetScope mosaics and S2 imagery (C. B. Lee et al., 2023) confirms that the lagoon hosts large, continuous seagrass meadows.

From a scientific view, Anse-aux-Pins can be considered a lab site to analyze seagrass dynamics. Its partial-enclosed design makes it sensitive to changes in nearshore pressures, sediment inputs and water clarity which are known to affect seagrass health in small-island coastal systems (Ingram et al., 2001; Unsworth et al., 2019). At the same time, the lagoon's shallow depth improves the visibility of benthic features in medium and high-resolution optical satellite imagery, making the lagoon well-suited for remote-sensing analysis (C. B. Lee et al., 2023).

The motivation to look at long-term trends is also further backed by observations made by local experts, who state that the seagrass cover at Anse-aux-Pins has changed over time. This proves that the site is interesting for assessing long-term seagrass change.

1.6 Long-term monitoring of coastal marine ecosystems

Long-term monitoring is essential to understand how coastal ecosystems respond to environmental change. Coastal systems such as coral reefs, mangroves, salt marshes, macroalgae and seagrass meadows face similar climatic and anthropogenic stressors which include warming, sea-level rise, extreme weather events and water-quality changes. These shared pressures highlight the relevance of long-term observations across coastal habitats and underline the transferability of monitoring methods between systems *(Fig. 8)* (Guild et al., 2025).

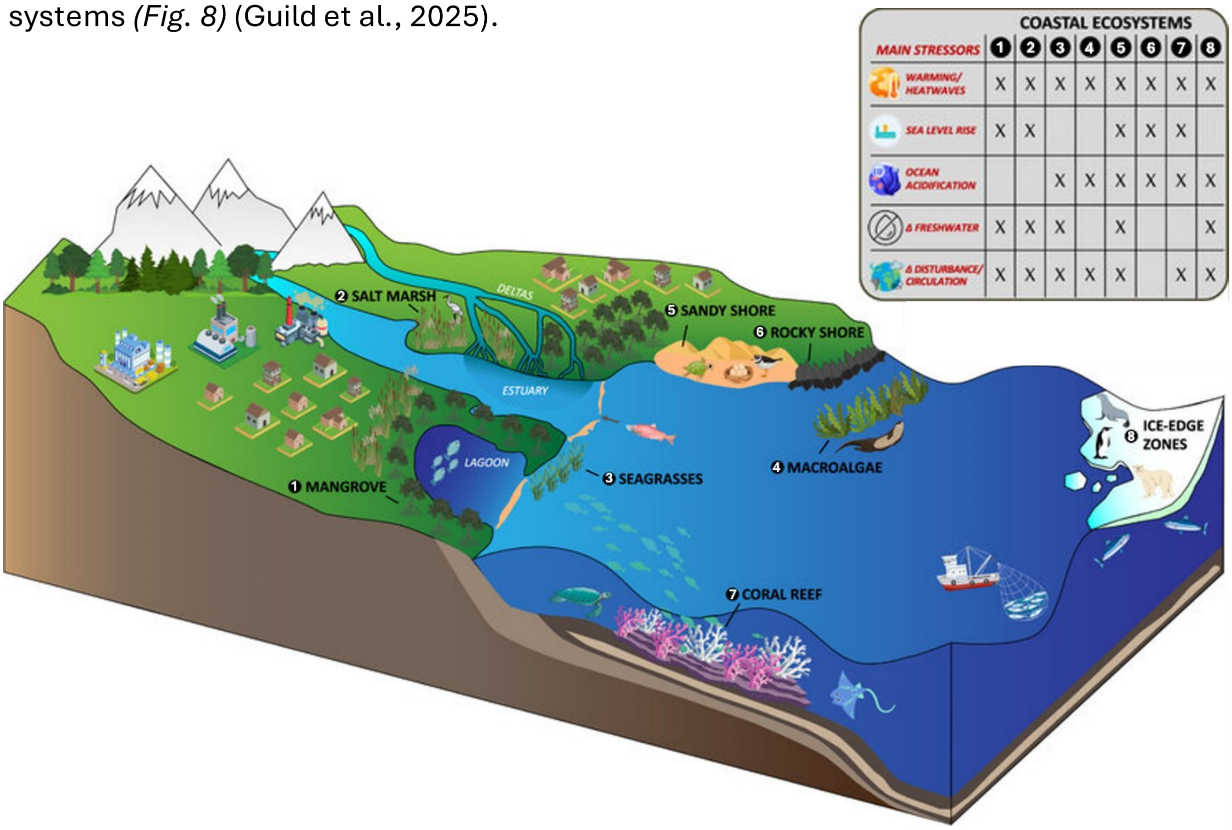

Figure 8 - Conceptual diagram of major coastal ecosystems and their exposure to climate-change stressors. The diagram shows the spatial organization of several coastal habitats including salt marshes, mangroves, seagrasses, macroalgae and coral reefs and summarizes the main stressors affecting all of them (warming, sea-level rise, acidification, freshwater inputs and changes in ocean circulation). Adapted from (Guild et al., 2025)

Historically, one of the systems that has been tracked the most is coral reefs. Multi-decadal field observations and satellite archives have revealed general decreases in coral cover and an increase in bleaching frequency linked to marine heatwaves (Hughes et al., 2018). These long-term datasets show how chronic pressures, including warming and water-quality degradation, interact with episodic disturbances to influence reef resilience. The example of the coral reef shows how an accurate base for identifying structural and functional change can be obtained by combining repeated ecological observations with continual imaging.

Mangrove forests also benefit from long-term monitoring because of their distinct signal in optical imagery. Global estimates of biomass loss, recovery and changes have been produced using multi-decadal Landsat analyses (Friess et al., 2019). With recent measurements quantifying national carbon stocks and their variability, long-term studies are becoming more and more important for blue-carbon accounting in SIDS like the Seychelles (Wartman et al., 2025). These examples show how continuous time series support both ecological bases and national climate commitments.

Another analogy for seagrass monitoring is kelp forests. Medium-resolution satellites can detect their canopies, which allows time series to record large-scale variations and declines linked to ecological instability and marine heatwaves. According to Cavanaugh et al. (2025), kelp and seagrass ecosystems are sensitive to changes in turbidity, warming and nutrients. They also point out that multi-sensor time series, machine-learning classifiers and automated detection pipelines must all be integrated into modern monitoring. Seagrass research can benefit from the authors' claim that "decadal-scale remote sensing datasets are now needed for analyzing coastal ecosystem trends".

Salt-marsh monitoring is also another example of how multi-sensor integration improves long-term ecosystem assessment. For instance, (Agate et al., 2024) used Landsat time series and machine learning to quantify changes in salt-marsh width and coastal protection services. Although applied to salt marshes, such methodologies are conceptually transferable and could be adapted to seagrass ecosystems.

These methods show parallels for seagrasses, which can show both gradual and abrupt reactions to environmental pressures such as changes in temperature, turbidity, eutrophication and hydrodynamic conditions. Recent long-term studies show that satellite archives can be used to reconstruct multi-decadal trends. For instance, Cingano et al. (2024) mapped 20 years of species-level change in an Italian lagoon and Sebastian et al. (2023) used Google Earth Engine to analyze 17 years of decline in Lakshadweep. Together, they show that long-term optical satellite data, combined with modern analytical tools, provide a strong basis to evaluate long-term seagrass change.

1.7 Remote sensing of seagrasses

Because seagrass meadows are found in shallow, dynamic coastal environments, satellite imagery offers an affordable way to map their extent, observe spatial shifts and evaluate long-term ecological trends (Klemas, 2011). Over the past decade, technological advancements in sensor capabilities, atmospheric correction and analytical methods have increased the potential of optical imagery for monitoring seagrass habitats (Liang et al., 2023; McKenzie et al., 2022).

Among the available platforms, Sentinel-2 has become a key sensor for seagrass remote sensing due to its 10-20 m spatial resolution, multispectral resolution and frequent revisit time. These characteristics makes S2 suitable for the detection of subtropical and tropical meadows in clear or slightly turbid waters. Many studies have demonstrated that S2 can differentiate seagrass from sandy substrates, macroalgae or unvegetated lagoon floors (Y. Li et al., 2023; Widya et al., 2023; Zoffoli et al., 2020).

In Seychelles, C. B. Lee et al. (2023) produced one of the best regional mapping efforts to date, by combining S2 and NICFI data to identify meadows across the inner Seychelles islands. Their classification based on medium-resolution imagery can capture both continuous and fragmented beds across island settings, improving national initial data for coastal ecosystem management. (*Fig. 9*)

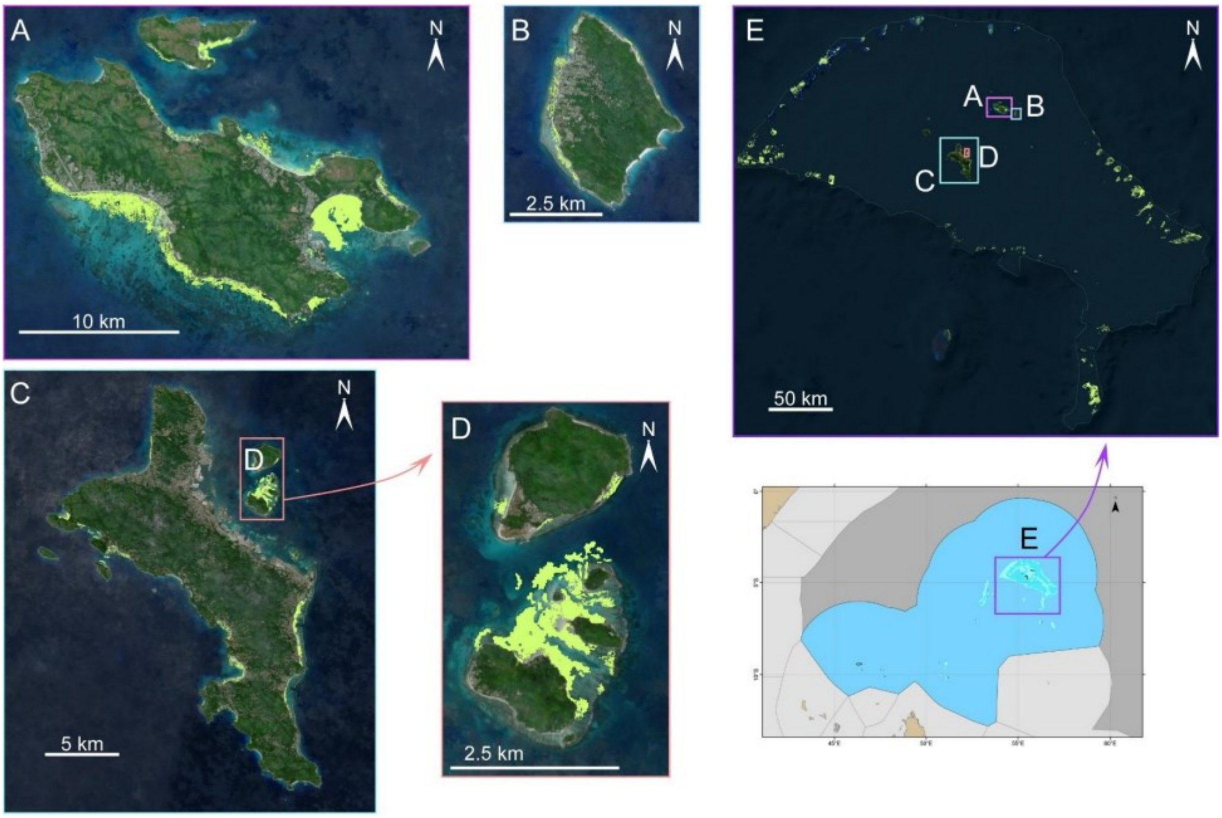

Figure 9 - Regional seagrass classification for the Mahé Plateau. Panels A-D show detailed classifications for Praslin, La Digue, Mahé and Ste. Anne/Cerf/Long, while panel E situates these sites within the broader plateau. The maps illustrate the ability of multi-temporal satellite datasets to detect continuous and fragmented shallow-water vegetation across island and lagoon systems. Adapted from (Rowlands et al., 2024).

In addition to determining the current extent, remote sensing simplifies the analysis of long-term seagrass dynamics. Using multi-year satellite archives, researchers are able to identify gradual ecological change, including meadow contraction, fragmentation, recolonization and species change. Time-series techniques improve consistency by taking advantage of the temporal redundancy of Landsat and Sentinel missions because individual scenes are frequently impacted by cloud cover, turbidity, or tidal variability (Cingano et al., 2024; Hill et al., 2024; Sebastian et al., 2023). In European lagoons, Cingano et al. (2024) reconstructed multi-decadal trends of species-level distribution and found declines in *Cymodocea nodosa* and *Zostera noltei* linked to environmental degradation. (*Fig.10*)

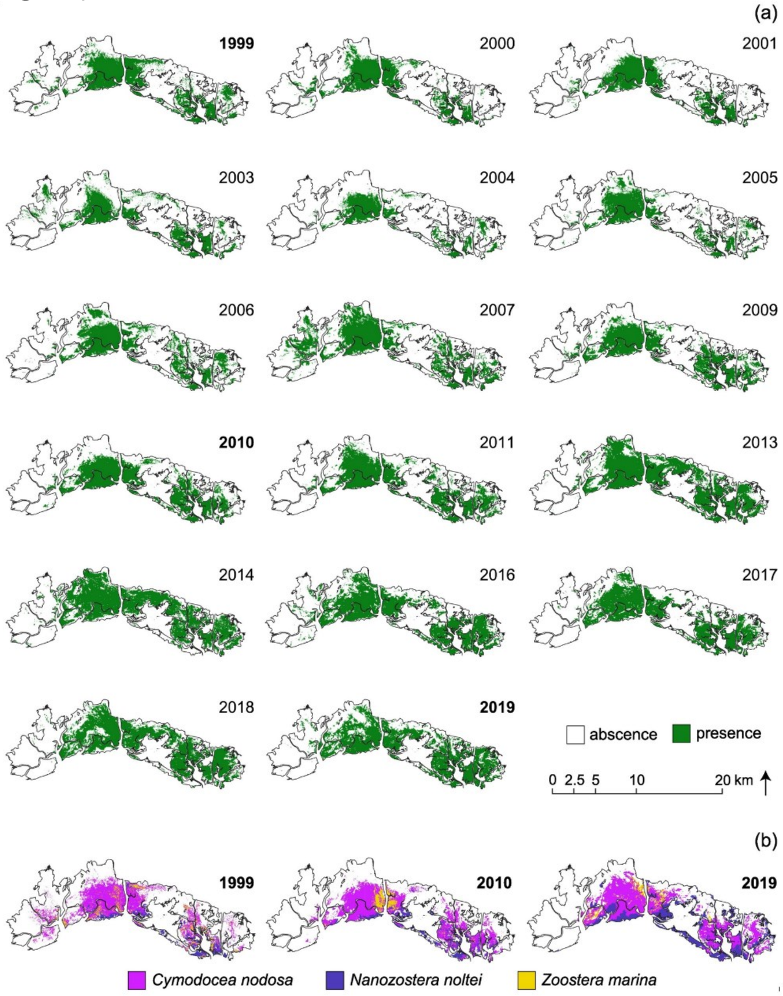

Figure 10 - Multi-decadal evolution of seagrass distribution and species composition. (a) Annual presence-absence maps from 1999 to 2019 obtained from Landsat imagery, showing spatial decrease and fragmentation of lagoonal meadows. (b) Long-term changes in dominant species (Cymodocea nodosa, Nanozostera noltei, Zostera marina) showing shifts in community composition over two decades. These time-series products demonstrate the ability of satellite archives to reveal gradual ecological change at scales difficult to traditional monitoring. Adapted from(Cingano et al., 2024).

The accuracy of seagrass mapping has also increased thanks to developments in machine-learning techniques. Random Forests, Support Vector Machines and gradient-boosting classifiers have proven to perform well in complex coastal environments where traditional thresholding methods fail to differentiate seagrass from spectrally similar environments (Amone-Mabuto et al., 2024; Mastrantonis et al., 2024; Widya et al., 2023).

Integrated workflows that combine medium and high-resolution sensors can further improve detection of small patches and heterogeneous meadows (Hill et al., 2024; McKenzie et al., 2022). These advancements are part of a larger trend in aquatic remote sensing toward data-driven methods and multi-sensor fusion.

1.8 Revealing the knowledge gap

Despite recent advances in seagrass remote sensing, important gaps remain in the temporal monitoring of tropical seagrass ecosystems, especially in tropical SIDS. Global studies apply more and more multi-sensor datasets, machine-learning classifiers and archives to map and monitor coastal vegetation over time (Klemas, 2011; Liang et al., 2023; McKenzie et al., 2022). However, the WIO remains less documented than many other regions, even though seagrass meadows have high ecological, carbon and management significance there (Palacios et al., 2021; UNEP, 2020).

In Seychelles, a recent national mapping improved knowledge of seagrass distribution and confirmed the large extent of these ecosystems within the EEZ (C. B. Lee et al., 2023; Rowlands, 2024). But this product is a reference map. It does not explain the variation in seagrass extent through time, whether shallow lagoon meadows have seasonal cycles, or whether change affect persistent cores, variable margins, recovery zones or potential loss areas. This temporal dimension is important as seagrass meadows are dynamic ecosystems and single maps don’t capture seasonality, interannual variability or spatial reorganization. A major gap is therefore the absence of a consistent workflow capable of reconstructing seagrass extent through time, under similar processing conditions. For this purpose, Sentinel-2 is well suited because it provides frequent, open-access imagery adapted to repeated monitoring of shallow coastal environments (Drusch et al., 2012; Zoffoli et al., 2020). However, mapping of tropical lagoons remains challenging, as seagrass detection is affected by water depth, turbidity, sunglint, bright sand, reef substrates, mixed pixels and seasonal optical variability (A. G. Dekker et al., 2011; Hedley et al., 2018; Zoffoli et al., 2020). Within this gap, Anse-aux-Pins is an appropriate site for development given the reference information available and it being a shallow reef-lagoon environment relevant to Seychelles coastal monitoring (C. B. Lee et al., 2023; Rowlands, 2024). It can therefore be used as a development site to train and evaluate a Sentinel-2 classification workflow and to reconstruct multi-year patterns of mapped seagrass extent. The knowledge gap that still exists is not just the lack of seagrass maps in Seychelles, but the lack of an operational link between mapping, time-series analysis and future scaling. Bridging this gap will aid in determining whether Sentinel-2 can provide accurate signals of seagrass extent over time and support broader monitoring perspectives for Seychelles seagrass meadows (Cingano et al., 2024; C. B. Lee et al., 2023; Rowlands, 2024).

2. Objectives and research question

Following the knowledge gaps mentioned in *Section 1.8*, this thesis seeks to fill the absence of Sentinel-2 based time-series workflow for monitoring and mapping seagrass in Seychelles shallow lagoons. While recent national mapping improved knowledge of seagrass distribution, no study has yet developed a reproducible approach able to reconstruct temporal patterns under comparable processing conditions for Seychelles.

The aim of this thesis is thus to develop a Sentinel-2 workflow for mapping seagrass, construct and analyze multi-year time series at a reference lagoon site and assess the scalability for broader application across Seychelles.

To achieve this goal, this thesis pursues three complementary objectives:

- Develop and evaluate a Sentinel-2 classification pipeline for mapping the extent of seagrass in shallow Seychelles lagoons.
- Derive Sentinel-2 time series for 2016-2026 and assess seasonal and interannual patterns of seagrass extent.
- Assess the potential scalability of the workflow to other secondary Seychelles lagoon sites and highlight the main requirements for wider applications.

Together, these objectives structure the analytical framework of this thesis and give the basis needed to answer the main research question:

“Can a Sentinel-2 pipeline be developed to map, monitor and analyze seagrass extent through time for Anse-aux-Pins and what are the main requirements toward broader application across the Seychelles EEZ?”

The analysis will then be guided by a set of secondary questions:

- What are the long-term (decadal) and short-term (seasonal) components of mapped seagrass extent variability?
- What are the spatial dynamics of mapped seagrass extent including persistent areas, seasonal margins and potential recovery or loss zones?
- How could the workflow developed for Anse-aux-Pins be applied to secondary lagoon sites in Seychelles and what does it say about broader scaling perspective?

These questions structure the methodological developments in the next section.

3. Materials & methods

This chapter presents the methodological pipeline (*Fig. 11*) that was developed and implemented in Python to map and analyze the extent of seagrass meadows in the Anse-aux-Pins lagoon. The workflow follows a specific order, from data download to multi-temporal analysis. The main Python libraries used in the processing, classification and analysis workflow are listed in *Appendix A*.

Each step is built on the previous one. The preprocessing make sure that remote sensing reflectance values are physically relevant. Then, the feature extraction transforms reflectance data into variables suitable to discriminate benthic classes. Finally, the classification produces seagrass maps, which are then aggregated to analyze inter-annual changes. In this section, each stage of the algorithm will be detailed.

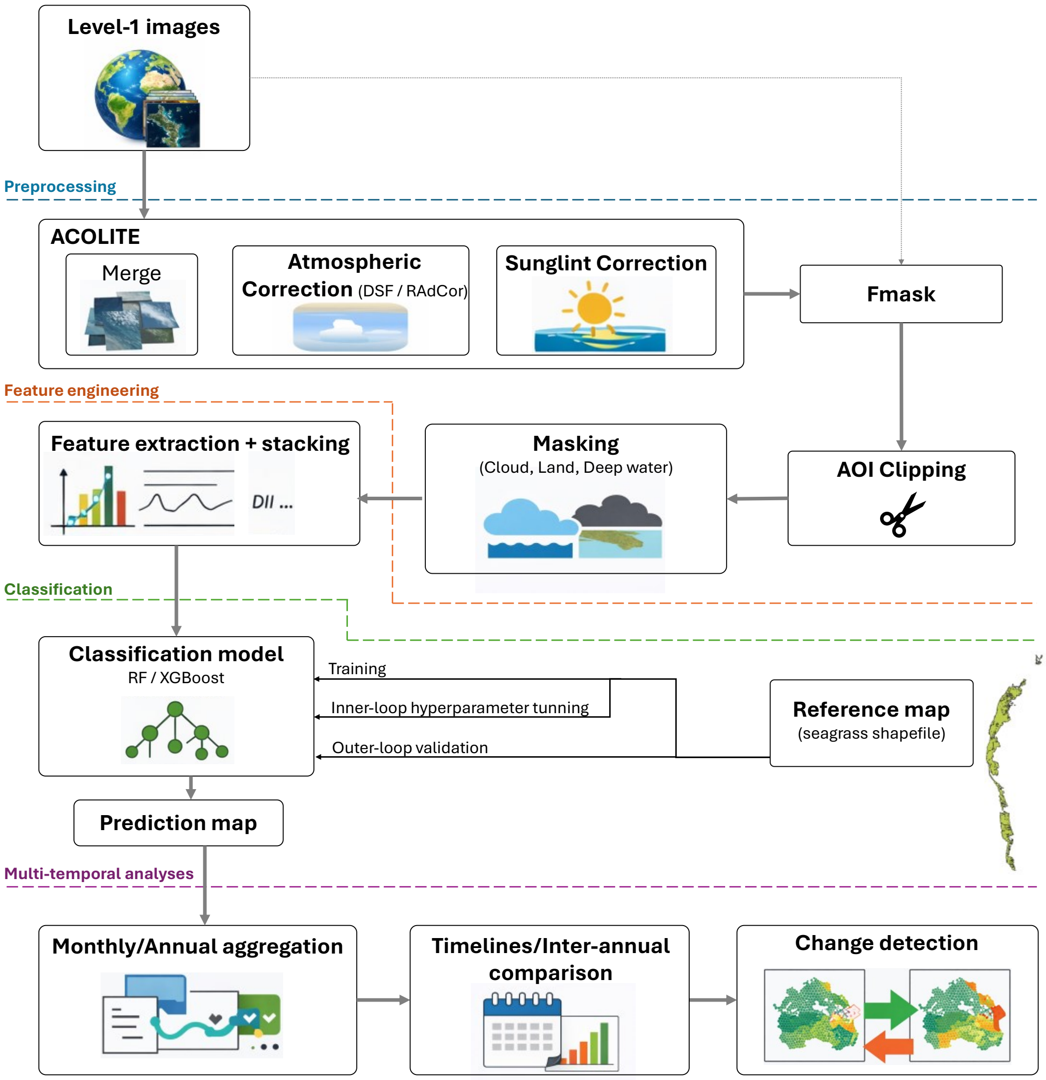

Figure 11 - Schematic representation of the methodological pipeline used for seagrass mapping. Sentinel-2 images are corrected for atmosphere and sunglint with ACOLITE, masked (cloud, land, deep water) and transformed into features. A classifier is trained with the reference map and then seagrass maps are generated, which are monthly/annually aggregated for timelines, inter-annual comparison and change detection.

3.1 Study sites

This study focuses on five shallow seagrass systems (*Tab. 1*) located around the inner granitic islands of Seychelles. The sites were selected because they host seagrass meadows that differ in lagoon morphology, exposure, bottom type and dominant seagrass assemblages. Anse-aux-Pins, on Mahé, was used as the primary site for model training, validation and temporal analysis. Four additional sites, Côte d'Or, Grande Anse, Sainte Anne and Baie Sainte Anne, were used as secondary application sites to assess the transferability of the model.

All the study areas were defined by areas of interest (AOIs) in geographic coordinate system (GCS). These AOIs are the spatial extent forced from the Sentinel-2 scenes before masking and classification. Fixed AOIs guaranteed consistency in space between acquisition dates and allowed the same processing workflow to be applied to all the sites.

3.1.1 Primary site: Anse-aux-Pins, Mahé

The Anse-aux-Pins lagoon (*Fig. 12*) is located on the east coast of Mahé Island. It forms a shallow lagoon partly enclosed by reef structures, which shield the area from direct oceanic exposure and provide suitable conditions for seagrass development. The lagoon is a mixture of seagrass, sand, reef substrat and also contains deeper water and thus is representative of the optical complexity of shallow tropical coastal systems.

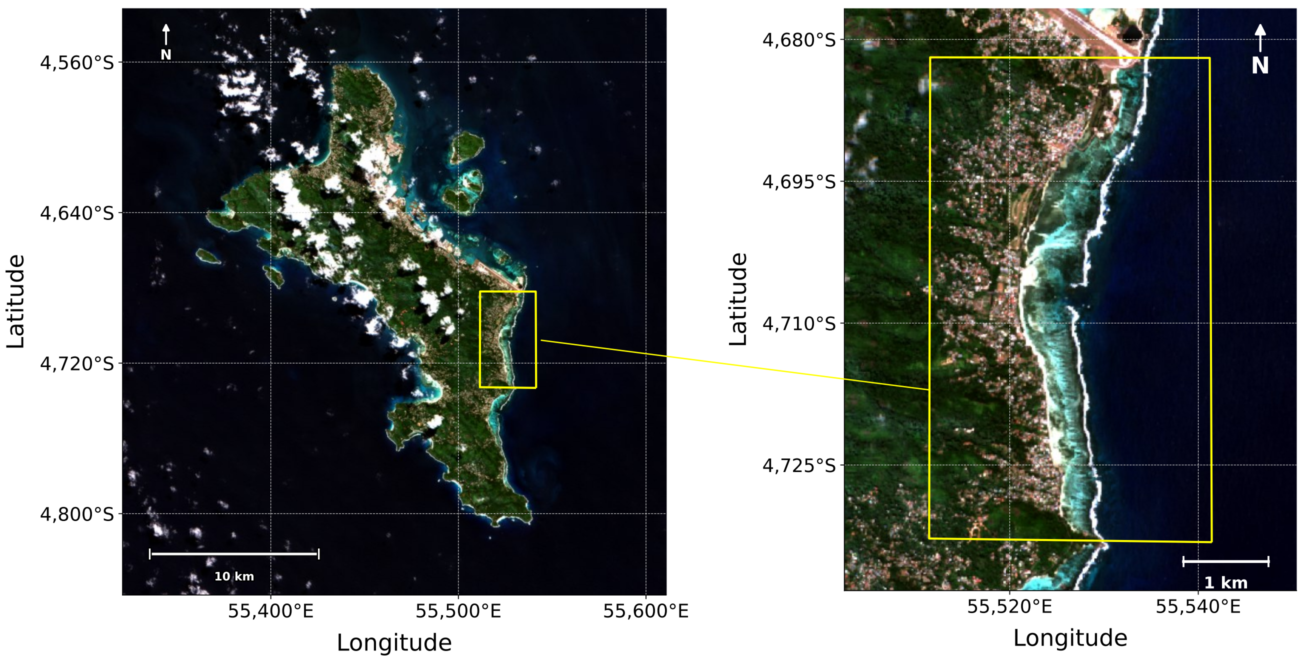

Figure 12 - Sentinel-2 true-color images 2025-06-27 of Mahé and zoom on the Anse-aux-Pins lagoon on Mahé Island. The primary area of interest used for training/validation is indicated by the polygon (yellow).

This site was selected as the primary study area because a seagrass reference map was available for Anse-aux-Pins. The reported seagrass assemblage includes *Thalassia*, *Oceana*, *Cymodocea*, *Halodule* and *Syringodium* (Rowlands, 2024). In this thesis, Anse-aux-Pins was used to develop the classification pipeline, evaluate model performance against the reference map and analyze temporal changes in mapped seagrass extent.

The AOI is defined by a bounding box in the World Geodetic System 1984 (WGS84) GCS, with longitude going from 55.5115 ° E to 55.5414 ° E and latitude going from −4.7332 ° to −4.6819 °. This box is the maximum spatial area of the AOI considered for seagrass mapping, within which the lagoon and all the seagrass meadows are located.

3.1.2 Secondary application sites

Four secondary sites (*Fig. 13*) were selected to test whether the model trained at Anse-aux-Pins could be applied to other seagrass systems in the same regional context. AOIs' bounding boxes in the WGS84 GCS (*Appendix B*). Two sites are located on Praslin: Côte d'Or and Grande Anse. Côte d'Or is a shallow lagoon with mixed seagrass assemblages, including *Thalassia*, *Oceana*, *Cymodocea*, *Halodule* and *Syringodium*. Grande Anse differs from the other sites because it is reported to be dominated by *Thalassodendron*, making it useful for testing the model on a meadow with a different canopy structure and potential spectral response.

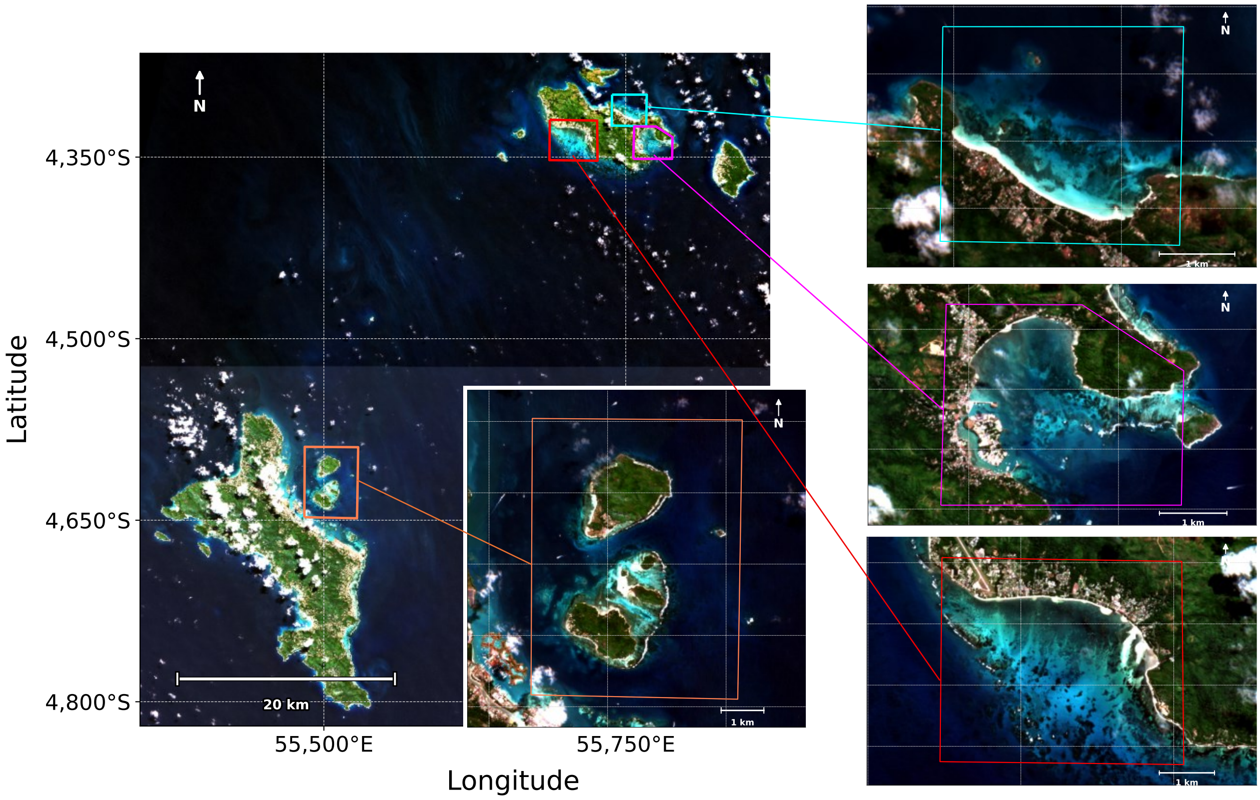

Figure 13 - Sentinel-2 true-color images 2025-06-27 showing Mahé and Praslin Islands, with the location of the selected secondary application sites. The colored outlines indicate the lagoon polygons used for secondary model application: Sainte-Anne (orange), Côte d'Or (cyan), Baie Sainte Anne (magenta) and Grande Anse (red).

The two other secondary sites are Sainte Anne and Baie Sainte Anne. Sainte Anne is located north-east of Mahé, within a reef-lagoon system surrounding small islands and contains mixed seagrass assemblages similar to those reported at Anse-aux-Pins and Côte d'Or. Baie Sainte Anne is located on Praslin and is reported to be dominated by *Enhalus*, providing another test case for transferability across different meadow types.

These secondary sites were not used for model training and validation. They were used only for model application and transferability assessment. The comparison between sites was based on the spatial coherence of predicted seagrass areas, the consistency of model outputs across the Sentinel-2 time series and the influence of site-specific conditions such as depth, substrate brightness, lagoon morphology and species composition.

Table 1 - Summary of the study sites. Mixed meadows include Thalassia, Oceana, Cymodocea, Halodule and Syringodium.

Site	Island	Role	Meadow type
Anse-aux-Pins	Mahé	Training / validation	Mixed meadow
Côte d'Or	Praslin	Application	Mixed meadow
Grande Anse	Praslin	Application	*Thalassodendron*-dominated
Sainte Anne	Mahé	Application	Mixed meadow
Baie Sainte Anne	Praslin	Application	*Enhalus*-dominated

3.2 Data sources

3.2.1 Sentinel-2 MSI imagery

This study used satellite imagery from the Sentinel-2 Multi Spectral Instrument (S2-MSI) mission between April 2016 and May 2026. Developed by the European Space Agency (ESA), the S2-MSI constellation actually consists of multiple satellites, Sentinel-2A (2015-2025), Sentinel-2B (2017-present) and Sentinel-2C (2025-present), which have identical spectral band definitions and radiometric characteristics and together provide a revisit time of approximately five days at the equator. This temporal resolution is particularly useful in tropical coastal regions where frequent cloud cover can limit data availability (Drusch et al., 2012; ESA, 2023).

Level-1 Collection (L1C) products were automatically downloaded from the Copernicus Open Access Hub using a Python script. These products provide top-of-atmosphere (TOA) reflectance values that are orthorectified and projected in the Universal Transverse Mercator (UTM) coordinate system. We used L1C products to have control over the atmospheric correction and other corrections methods. This is important in shallow-water environments, where standard land-oriented corrections may be less accurate (Vanhellemont, 2019). The AOI is covered by orbit 034 and only scenes corresponding to this orbit were selected.

S2-MSI records data in 13 spectral bands (*Tab. 2*) ranging from the visible to shortwave infrared (SWIR). Four bands: blue, green, red and near-infrared (NIR) are provided at 10 m spatial resolution, which is well suited for mapping shallow coastal environments. Additional red-edge and SWIR bands at 20 m resolution provide complementary spectral information that can improve vegetation detection and water correction steps (Delegido et al., 2011; Pahlevan et al., 2017). The spectral composition of S2 makes it ideal for mapping shallow-water. While the Red-edge and NIR bands are used for identifying vegetation and for separating land from water, the blue and green bands are sensitive to water-column properties and bottom reflectance (Hedley et al., 2018; Roca-Mora et al., 2026). Additionally, the SWIR bands helps for the sunglint and atmospheric corrections.

Table 2 - Spectral characteristics of Sentinel-2 MSI bands

Band	Name	Central wavelength (nm)	Resolution (m)
B1	Coastal aerosol	443	60
B2	Blue	492	10
B3	Green	559	10
B4	Red	665	10
B5	Red-edge 1	704	20
B6	Red-edge 2	740	20
B7	Red-edge 3	783	20
B8	NIR	833	10
B8A	Narrow NIR	865	20
B9	Water vapor	945	60
B10	Cirrus	1375	60
B11	SWIR 1	1610	20
B12	SWIR 2	2190	20

3.2.2 Ancillary data

Ancillary atmospheric data were used indirectly during image preprocessing through the ACOLITE atmospheric correction workflow (see *Section 3.3.2* for details). ACOLITE retrieves auxiliary meteorological information from NASA EarthData services when required for atmospheric parameter estimation. These supplementary datasets contain meteorological parameters and atmospheric variables like aerosol attributes that are obtained from global reanalysis products. ACOLITE uses the data internally to enhance the atmospheric correction algorithms (Vanhellemont, 2019; Vanhellemont & Ruddick, 2018). Ancillary data are also involved in the sunglint correction procedure implemented in ACOLITE. In particular, wind-related parameters may influence the estimation of air-water interface effects, depending on the selected correction options.

3.2.3 Reference seagrass map

The shapefile (Fig. 14), which comes from the national seagrass cartography project (Rowlands, 2024) done under the SeyCCAT MACCE program, was supplied by partners from the University of Seychelles. The mapping was created as part of a project to record and evaluate seagrass meadows all over the Seychelles. As a result is a map product.

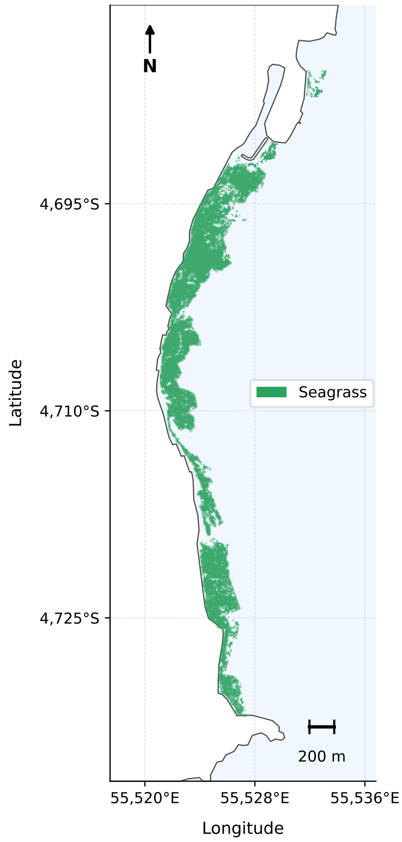

Figure 14 - Seagrass meadow polygons (green) in the Anse-aux-Pins lagoon shapefile from the SeyCCAT MACCE cartography project (Rowlands, 2024). The polygons are seagrass map product created from a previous model based on field observations from October and November 2021. Shapefile provided by Jérôme Harlay (University of Seychelles).

Field-based observations were collected between October and November 2021 during the national seagrass mapping campaign. However, the shapefile used in this thesis does not correspond to direct field observations or manually mapped groundtruth polygons. The seagrass boundaries are produced by a previous model trained with field observations. Thus the polygons are a model derived cartographic product with spatial resolution of about 3-4 m.

The quality of this product is spatially variable. In the original mapping work, the validation results for the North region, which includes Mahé, were lower than for the Central and South regions, with an overall accuracy of 69.7% and a seagrass F1-score of 63.3%. Therefore, the Anse-aux-Pins shapefile was considered as the best available reference seagrass map, but not as an error-free groundtruth dataset. This limitation is important because uncertainties from the original product may affect the interpretation of results derived from it (See *Section 4*) (C. B. Lee et al., 2023; Rowlands, 2024).

3.3 Image preprocessing

3.3.1 Image selection and filtering

All L1C Sentinel-2 scenes coming from orbit 34, covering the AOI between April 2016 and May 2026 were automatically downloaded. The download process was intentionally not filtered based on cloud cover, in order to retain the full archive and ensure consistent preprocessing prior to quality filtering. Due to temporal overlap between sensors missions, multiple acquisitions may be available for a same date. Thus priority was given to the most complete data then to the latest sensor.

The AOI is located close to the boundary of multiple S2 tiles. In order to provide enough spatial context for atmospheric correction, neighboring tiles were systematically included during preprocessing. These tiles were merged into a single continuous scene using the *"merge_tiles=True"* option in ACOLITE. This approach avoids gaps at tile borders and improves the estimation of atmospheric parameters, which is known to benefit from larger spatial domains in coastal environments (Vanhellemont, 2019; Vanhellemont & Ruddick, 2018).

Selected acquisitions (*Tab. 3*) were processed using the same pipeline. The S2 bands were also resampled to a common spatial resolution of 10 m. This resampling step ensures the spatial consistency between bands and avoids the misalignment for the next steps.

Table 3 - Number of Sentinel-2 acquisitions for each year and each sensor

Sensor	2016	2017	2018	2019	2020	2021	2022	2023	2024	2025	2026	Total
S2A	27	37	36	37	33	36	35	37	37	2	0	317
S2B	0	19	38	35	39	36	37	35	37	35	15	326
S2C	0	0	0	0	0	0	0	0	1	38	15	54
Total	27	56	74	72	72	72	72	72	75	75	30	697

3.3.2 Atmospheric and sunglint correction

Atmospheric correction was performed using ACOLITE v20251013.0, a processing software specifically designed for aquatic applications of optical satellite imagery (Vanhellemont, 2025; Vanhellemont & Ruddick, 2018). Two atmospheric correction methods were evaluated and compared based on their impact on the classification performance as no in situ reflectance measurements were available. ACOLITE was used because it returns a better corrected reflectance, particularly in the blue and green spectral bands, where it often performs better than many other atmospheric correction methods (Pahlevan et al., 2017; Vanhellemont, 2019; Vanhellemont & Ruddick, 2018).

Blue and green bands are very sensitive to water-depth and composition, making them great for seagrass detection. ACOLITE can be applied to S2 images and has had good results in tropical and equatorial regions (Pahlevan et al., 2022; Vanhellemont, 2019), making it suited for this study.

ACOLITE's default method, the Dark Spectrum Fitting (DSF) method aerosol optical thickness was estimated directly from the image by identifying dark pixels and fitting atmospheric parameters accordingly (Vanhellemont, 2019). In this study, the fixed aerosol estimation (*"dsf_aot_estimate=fixed")* was used because the final processed AOI was small enough to apply one single atmospheric correction over the lagoon and surroundings. This approach assumes spatially homogeneous atmospheric conditions over the scene and is commonly applied in small coastal regions like this thesis' AOI (Castagna & Vanhellemont, 2025; Vanhellemont, 2025).

For the Remote sensing Adjacency Correction (RAdCor) method, atmospheric correction includes adjacency effects, which occur when the reflectance from neighboring pixels (e.g. land, clouds or bright shallow areas) influences the observed signal of a given pixel. Aerosol optical thickness and aerosol models are estimated using TOA-Surface Dark Spectrum Fitting (TSDSF), a generalisation of the DSF method for surface heterogeneity and provides inputs for adjacency correction (Castagna & Vanhellemont, 2025). RAdCor relies on a spatial kernel to model relation between pixels. Thus, a buffer was included around the AOI. Following ACOLITE recommendations, a 5 km padding was applied for adjacency effects to be computed.

In both case, the sunglint correction was applied using the glint correction option implemented in ACOLITE. Sunglint is caused by the reflection of sunlight at the air-water interface and can artificially increase reflectance values in visible and near-infrared bands. Correction of sunglint is required in shallow coastal environments to avoid the overestimation of remote sensing reflectance and to improve detection of submerged features (Hedley et al., 2005; Vanhellemont, 2019).

Level-2 water products (L2W) were generated by ACOLITE's processing. The analysis used remote sensing reflectances (Rrs, Rrs_*), which is the radiance normalized by downwelling irradiance and corresponds to the signal leaving the water column after atmospheric and surface corrections. This quantity isolates the aquatic optical signal, including contributions from the water column and benthic substrate, with minimal effects of the atmosphere and surface reflection. The Rrs data is the main input for feature extraction and following classification.

3.3.3 Masks

Only after atmospheric and sunglint correction, cloud, land and deep-water masks were applied to remove pixels that were not appropriate for seagrass detection.

Cloud masking was performed using the Function of Mask (Fmask) algorithm rather than the internal ACOLITE cloud mask, in order to maintain independence between processing steps and avoid the excessive coastal and land pixels masking of ACOLITE. Fmask was implemented via the python-fmask library (version 0.5.10) (GERSL/FMask, 2026). Fmask is an object-based approach that detects clouds and cloud shadows using spectral and thermal information (Zhu et al., 2015; Zhu & Woodcock, 2012).The method is also used within the Harmonized Landsat-Sentinel (HLS) processing framework to ensure consistent cloud masking across sensors, supporting its use in this study (Claverie et al., 2018; Ju et al., n.d.).

Cloud masks were produced from the original Level-1 imagery rather than from atmospherically corrected products. This was done, accordingly with Fmask recommendations, to preserves the original radiometric and geometric structure of the data, which is required for optimal performance of Fmask. Using corrected reflectance products can alter and degrade cloud detection accuracy (Qiu et al., 2019). Fmask parameter settings were used to account for S2 specific characteristics and to limit over-masking (*Appendix C*). Permissive parameters were applied, with reduced cloud probability thresholds and small buffer distances, in order to avoid masking bright shallow-water pixels which are common in lagoons images. Cloud masking was applied, while cloud shadows, snow and water classes were not removed (Zhu et al., 2015).

In addition to cloud masking, a land mask was applied based on the coastline to exclude land pixels from the analysis. This mask also excludes the inner lagoon enclosed by the reclaimed structure , which appears in *Fig. 15a* as a skyblue masked area to the north inside the lagoon, despite visually corresponding to water. This area is excluded because it is subject to stronger eutrophication and has a different water residence time and flushing compared to the main lagoon. As a result, its optical and ecological properties are significantly different, which could bias the classification and temporal comparison.

Finally, a deep-water mask based on visual interpretation of the imagery and the local bathymetry, was also applied to exclude offshore pixels where bottom reflectance is negligible and where seagrass detection is not relevant. These masking and clipping steps guaranteed that feature extraction and classification were all limited to valid shallow-water pixels within the lagoon (*Fig. 15*).

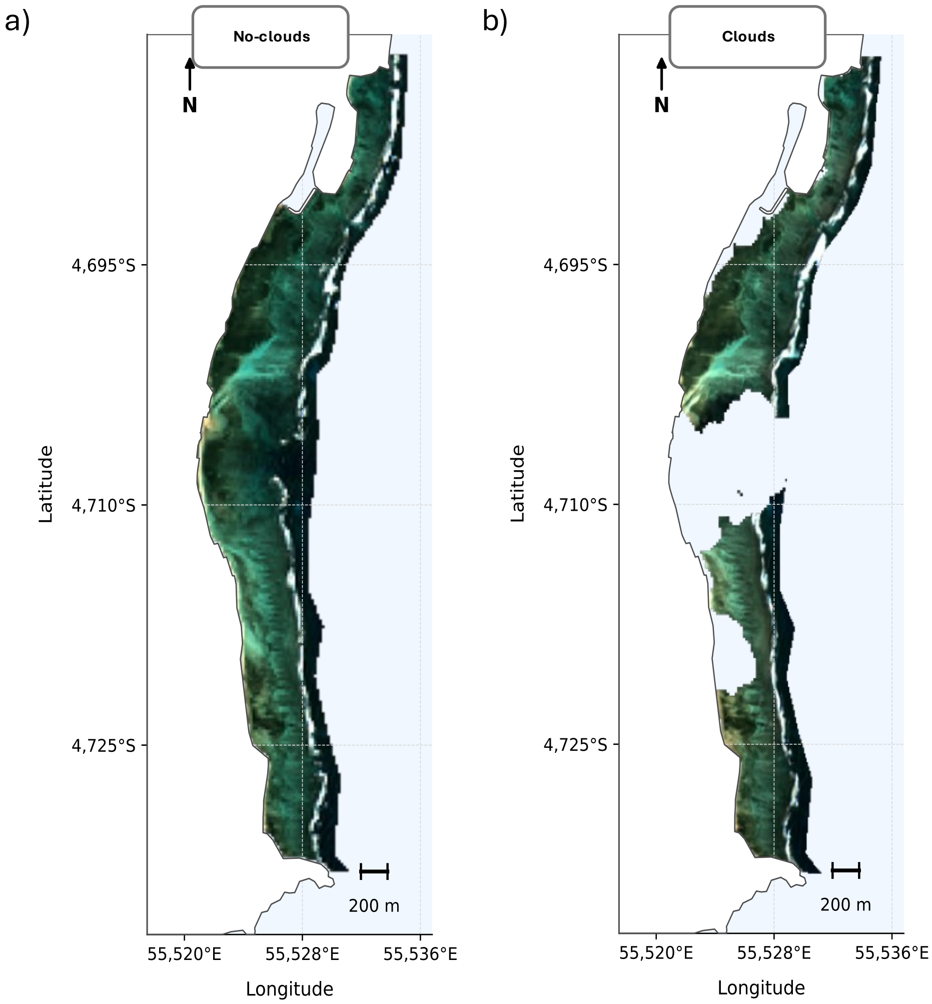

Figure 15 - Example of a final lagoon areas, used for further steps, after AOI clipping and application of cloud, land and deep-water masks. a) without clouds b) with clouds

3.4 Basis for seagrass detection

3.4.1 Optical properties of underwater vegetation

Seagrass detection using optical satellite imagery works by using the spectral behavior of submerged vegetation. Like terrestrial plants, seagrass contains chlorophyll pigments that absorb strongly in the blue (≈440-490 nm) and red (≈660-670 nm) wavelengths, while reflecting more light in the green region (≈550-560 nm). This creates a characteristic spectral pattern that can be used to distinguish vegetated from non-vegetated substrates (*Fig. 16*) (Thorhaug et al., 2007).

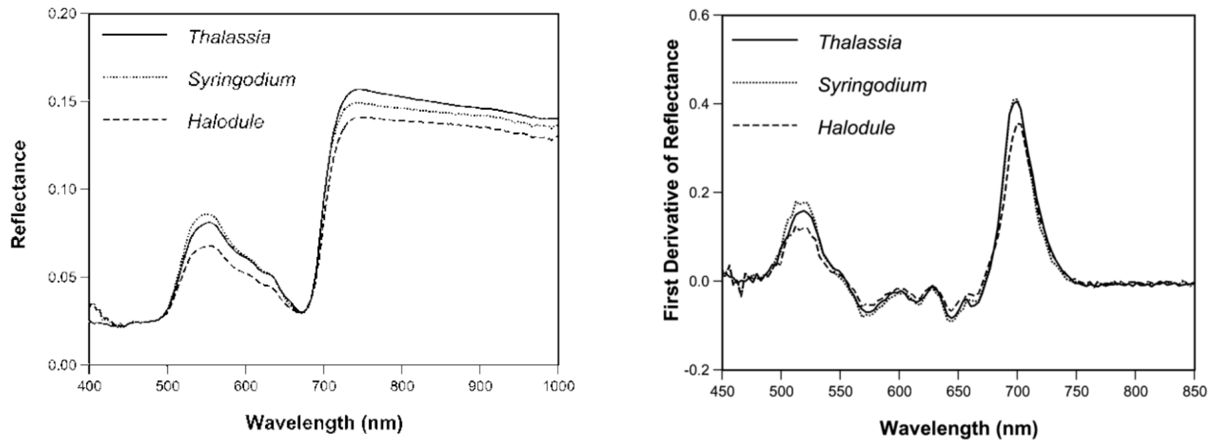

Figure 16 - Reflectance curves of seagrass species in shallow water. Differences in blue and green wavelengths provide the main spectral basis for discrimination. Source : (Thorhaug et al., 2007)

As seagrass is located below the water surface, the signal measured by a satellite sensor is influenced not only by the plant itself but also by the water column above it. Light attenuation in water reduces the intensity of reflected signals, especially in red and near-infrared wavelengths. As a result, shallow-water mapping relies mainly on the blue and green spectral bands, where light penetration is higher (Z. Lee et al., 1998).

In clear shallow waters, the bottom reflectance contributes significantly to the Rrs signal. Seagrass meadows typically show lower reflectance in the blue band compared to sandy substrates, while differences in the green band can help improve class separation. These spectral contrasts are the basis for seagrass mapping using multispectral imagery such as S2-MSI (Amone-Mabuto et al., 2024; Cingano et al., 2024). Recent studies have demonstrated that Visible bands, particularly in the blue and green region, provide most of the spectral information required for mapping seagrass in shallow coastal waters. Additional spectral bands, such as red-edge wavelengths available in Sentinel-2, can further improve vegetation detection when available. When they are combined with appropriate preprocessing, these bands allow reliable discrimination between vegetated and non-vegetated seabeds in optically-shallow waters (Caballero et al., 2020; C. B. Lee et al., 2023; Z. Lee et al., 1998).

3.4.2 Constraints affecting detection

Several factors limit the detectability of seagrass from satellite imagery. Among these, water depth is the most important constraint. As depth increases, light gets progressively absorbed and scattered, which reduces the contribution of bottom reflectance to the signal detected by the sensor. After a certain depth, the seabed becomes optically invisible and classification accuracy decreases (Z. Lee et al., 1998). Seagrass detection is thus limited to optically shallow areas typically above 30 m. Water turbidity also affects detection. The suspended sediments and other particles increase the scattering effect in the water column, which reduces clarity and modifies spectral signatures. Temporal changes in turbidity can thus lead to differences in reflectance values between different acquisition dates, even if benthic cover remains unchanged (Cingano et al., 2024). Another limitation is the spectral similarity between substrates. Some sandy bottoms, macroalgae, or mixed substrates can have reflectance values closely similar to seagrass under certain light or depth conditions. This thus reduces separability and increases classification uncertainty (Amone-Mabuto et al., 2024). Surface effects such as sunglint and residual atmospheric correction errors can also affect reflectance values. Although preprocessing aims to minimize these effects, some variability stays and must thus be considered when spectral features are selected and classification models trained. Finally, the targeted spatial resolution of satellite imagery (10 m for S2) means that individual pixels can include mixed substrates in heterogeneous lagoon environments. Mixed pixels can reduce spectral contrast between classes and thus affect the classification results.

These constraints are the reason why a robust preprocessing with feature engineering and machine-learning classification is necessary in complex environments.

3.5 Feature extraction

3.5.1 Spectral features and transformations

The selection of input features (*Tab. 4*) is a key step for seagrass classification, as it defines the ability of the model to distinguish seagrass from non-seagrass substrates in varying environments. In this study, features were derived from ρs products to capture spectral, depth-related and spatial properties of the lagoon environment. A full set of 30 features is computed from Sentinel-2 images. The feature set combines (i) raw spectral reflectance, (ii) depth-invariant indices to reduce water-column effects, (iii) spectral ratios highlighting vegetation signatures and (iv) spatial context metrics computed over a 3×3 neighborhood to capture the spatial structure of seagrass. This combination allows the model to better distinguish seagrass from sand under variable depth and turbidity conditions (Amone-Mabuto et al., 2024; Z. Lee et al., 1998). The same feature were used to interpret separability, feature redundancy and temporal stability of the spectral signal.

Table 4 - Feature set used for classification with Sentinel-2

Family	Feature	Definition	Expected role
Spectral reflectance	B01	Rrs at 443 nm (coastal blue)	Water clarity and shallow bottom signal
	B02	Rrs at 492 nm (blue)	Strong water penetration
	B03	Rrs at 559 nm (green)	Key band for benthic habitat
	B04	Rrs at 665 nm (red)	Chlorophyll absorption
	B05	Rrs at 704 nm (red-edge)	Vegetation reflectance signal
	B08	Rrs at 833 nm (NIR)	Detects shallow water or mixed pixels
	B11	Rrs at 1610 nm (SWIR1)	Water-land discrimination
Depth-invariant	DII(B02,B03)	Depth-invariant index from B02 and B03	Reduce depth effect
	DII(B01,B03)	Depth-invariant index from B01 and B03	Reduce depth effect
	DII(B03,B04)	Depth-invariant index from B03 and B04	Reduce depth effect
Spectral Index	IDX_B03_B02	(B03 − B02) / (B03 + B02)	Blue-green spectral contrast
	IDX_B04_B03	(B04 − B03) / (B04 + B03)	Vegetation absorption contrast
	IDX_B05_B04	(B05 − B04) / (B05 + B04)	Red-edge vegetation signal
	IDX_B05_B03	(B05 − B03) / (B05 + B03)	Vegetation spectral response
Band ratios	RATIO_B03_B02	B03 / B02	Relative blue-green reflectance
	RATIO_B04_B03	B04 / B03	Red-green reflectance ratio
	RATIO_B05_B03	B05 / B03	Red-edge to green ratio
Spectral difference	DIFF_B03_B02	B03 − B02	Blue-green slope
	DIFF_B04_B03	B04 − B03	Green-red slope
	DIFF_B05_B03	B05 − B03	Red-edge slope
Spatial metrics	MEAN3x3_DII _B02_B03	Mean DII_B02_B03 in a 3×3 window	Stabilizes depth correction
	STD3x3_DII_B02_B03	Standard deviation of DII_B02_B03 in a 3×3 window	Spatial variability of bottom signal
	MEAN3x3_B03	Mean B03 value in a 3×3 window	Local reflectance consistency
	STD3x3_B03	Standard deviation of B03 in a 3×3 window	Detects structure
	MEAN3x3_B05	Mean B05 value in a 3×3 window	Local vegetation signal
	STD3x3_B05	Standard deviation of B05 in a 3×3 window	Spatial variability of vegetation
	MEAN3x3_ RATIO_B03_B02	Mean RATIO_B03_B02 in a 3×3 window	Spatial stability of ratio
	STD3x3_ RATIO_B03_B02	Standard deviation of RATIO_B03_B02 in a 3×3 window	Ratio heterogeneity
	MEAN3x3_NDWI	Mean NDWI in a 3×3 window	Local water conditions
	STD3x3_NDWI	Standard deviation of NDWI in a 3×3 window	Water variability

The visible bands in the blue (≈440-490 nm), green (≈550-560 nm) and red (≈660-670 nm) regions contain most of the information related to bottom reflectance in shallow waters because light penetration is at the highest in the blue-green part of the spectrum. These wavelengths therefore carry most of the signal related to benthic substrates and submerged seagrass (Amone-Mabuto et al., 2024; Traganos & Reinartz, 2018). The green band (559 nm) is particularly informative for detecting submerged vegetation due to the reflectance peak of aquatic plants in this region (Mumby et al., 2004).

Additional bands were included to capture extra data past the visible spectrum range. The red-edge band (≈704 nm), is sensitive to vegetation reflectance transitions and can retain vegetation signals even under shallow water (Fyfe, 2003; Hedley et al., 2018). The NIR band (≈833 nm) is strongly absorbed by water but still capture data in very shallow areas or mixed pixels, helping to identify areas where vegetation reaches the surface or where bottom reflectance is strong (A. G. Dekker et al., 2011). Finally, the SWIR band (≈1610 nm) shows strong water absorption and is therefore useful for distinguishing water from land or mixed pixels on coastal areas (Xu, 2006).

Depth-invariant indices (DII) are used in shallow-water remote sensing to reduce the influence of variable bathymetry and water-column attenuation (A. G. Dekker et al., 2011; Green et al., 2000; LYZENGA, 1981). The general formulation is:

$$DII_{ij} = \ln(R_i) - k_{ij}\ln(R_j)$$

where R_i and R_j are Rrs values at wavelengths i and j and k_{ij} is derived from attenuation relationships directly estimated from valid pixels from scenes. This transformation reduces variability related to depth while still keeping differences between bottom types (Z. Lee et al., 1998). The band combinations (492,559), (442,559) and (559,665) balance water penetration and vegetation contrast.

We used normalized spectral indices and band ratios to increase spectral contrasts between benthic types while reducing sensitivity to variable illumination. Normalized difference indices are commonly used in aquatic remote sensing because they emphasize relative differences between bands rather than absolute reflectance values (Mumby et al., 2004; Roelfsema et al., 2014). Here, we considered the following indices:

$$\frac{R_{559} - R_{492}}{R_{559} + R_{492}} \quad ; \quad \frac{R_{665} - R_{559}}{R_{665} + R_{559}} \quad ; \quad \frac{R_{704} - R_{665}}{R_{704} + R_{665}} \quad ; \quad \frac{R_{704} - R_{559}}{R_{704} + R_{559}} \quad ,$$

as well as:

$$\frac{R_{559}}{R_{492}} \;;\; \frac{R_{665}}{R_{559}} \;;\frac{R_{704}}{R_{559}}$$

to capture and improve the relative spectral contrasts related to vegetation while reducing the sensitivity to differences in illumination. These combinations are commonly used in shallow-water seagrass mappings (A. Dekker et al., 2007; Mumby et al., 2004; Roelfsema et al., 2014). Simple spectral differences such as:

$$R_{559} - R_{492} \;,\; R_{665} - R_{559} \; and \; R_{704} - R_{559}$$

were also computed to approximate the spectral slopes. These slopes provide complementary information to normalized indices and can capture subtle transitions in spectral reflectance associated with seagrass.

Finally, local statistics were computed using a 3×3 moving window due to the patchy spatial structure of seagrass meadows and the heterogeneous distribution of seagrass, sand and mixed substrates. These statistics include the mean and standard deviation of the selected features, including bands, indices and the Normalized Difference Water Index (NDWI), which was used to capture water presence change and surface conditions. The mean values describe the local consistency in reflectance and the standard deviation shows the spatial heterogeneity. These texture-like metrics allow the model to capture the patchiness and edges of seagrass, which also improves the discrimination between seagrass and non-seagrass areas.

3.5.2 Feature set for model input

Each feature family captures different characteristics of the lagoon environment and contributes to the discrimination between seagrass and non-seagrass areas (*Tab. 5*).

Table 5 - Summary of feature families used in the classification

Feature family	# features	Purpose
Spectral reflectance	7	Capture raw spectrum of substrates
Depth-invariant	3	Reduce water depth influence
Spectral Index	4	Improve seagrass spectrum contrast
Band ratios	3	Show relative spectrum differences
Spectral difference	3	Represent spectral slopes
Spatial metrics	10	Acquire spatial structure of seagrass
Total	30	

3.6 Classification

3.6.1 Dataset

The classification dataset used was created by merging the seagrass reference shapefile (*Section 3.2.3*), with feature stacks obtained from satellite imagery acquired in October-November 2021, which corresponds to the field survey period. Pixels located within the seagrass polygons were labelled as seagrass, while pixels located outside these polygons but within valid shallow-water areas were labelled as non-seagrass. Valid pixels are pixels remaining after masking was applied (*Section 3.3.3*).

The Sentinel-2 dataset was built (*Tab. 6*) using 10 acquisition dates. Dates were selected to provide the best conditions for model development, with a maximum of 70% cloud coverage over the AOI, in order to maximize quality while preserving temporal variability.

Table 6 - Distribution of reference pixels in the datasets,per sensor, used for model training and evaluation.

Sensor	Date	Valid pixels	Seagrass pixels	Non-seagrass pixels
Sentinel-2	2021-09-26 *	30,126	6,325	23,801
	2021-10-06	26,240	4,960	21,280
	2021-10-11	15,783	3,304	12,479
	2021-10-16	35,144	7,397	27,747
	2021-10-26	17,088	1,777	15,311
	2021-10-31	34,756	7,272	27,484
	2021-11-05	16,177	3,105	13,072
	2021-11-25	32,851	6,976	25,875
	2021-11-30	31,342	6,756	24,586
	2021-12-05 *	27,918	5,413	22,505
	Total	267,425	53,285	214,140

* Included despite outside the reference period, due to close temporal proximity.

3.6.2 Machine-learning model

Seagrass classification was performed using two supervised machine-learning algorithms: Random Forest (RF) and Extreme Gradient Boosting (XGBoost). RF is an ensemble method that constructs multiple decision trees and combines their predictions through majority voting (Breiman, 2001), while XGBoost is a gradient boosting algorithm that sequentially builds trees to correct the errors of previous ones (Chen & Guestrin, 2016). Both methods are widely used in remote sensing because they can handle high-dimensional data, are robust to noise and correlated features and do not require specific assumptions about data distributions (Amone-Mabuto et al., 2024; Belgiu & Drăguţ, 2016; Maxwell et al., 2018). Their complementary learning strategies make them well suited for comparison in coastal habitat mapping.

The models were implemented in Python using the scikit-learn and XGBoost libraries. The input features correspond to the spectral bands, depth-invariant indices, water indices, band ratios and texture metrics. A dedicated model was trained using the 30-feature Sentinel-2 dataset, corresponding to the spectral bands and derived features (*Section 3.5*). The model output is a probability for each pixel, which were then converted in a binary prediction using a probability threshold. Feature importance from the trained models was used as an interpretative output, not as an additional feature-selection step.

3.6.3 Training, validation and testing strategy

A nested cross-validation (CV) strategy (*Fig. 17*) based on the datasets acquisition dates was used to evaluate the classifier's ability to generalize over time (Roberts et al., 2017). Such strategy is recommended as it provides a more realistic estimate of the predictive performance compared to a random CV (Meyer et al., 2019; Roberts et al., 2017)

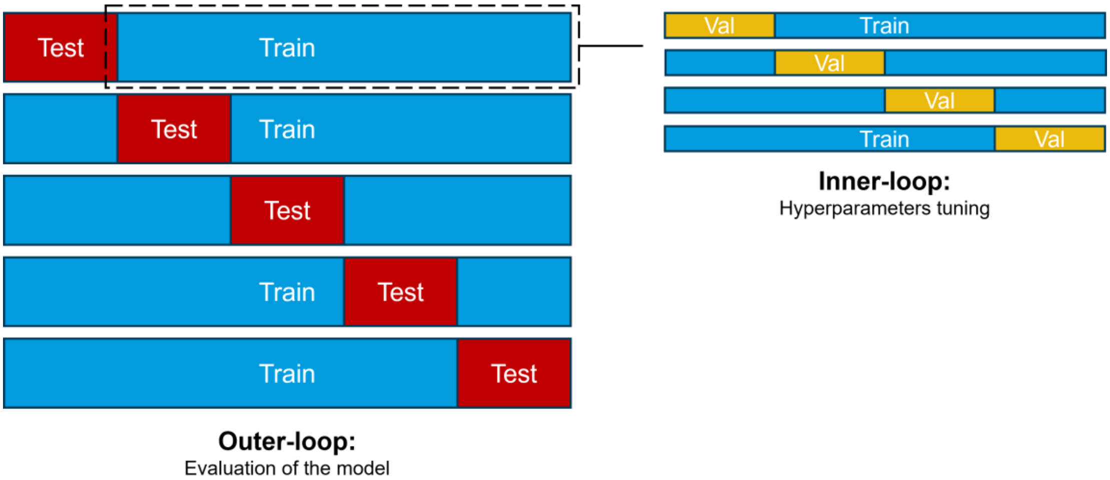

Figure 17 - Nested LODO-CV strategy used for model training and evaluation. In the outer loop, one date is put to the side as the test set while the remaining dates are used for model development. With the development data, an inner leave-one-date-out cross-validation is done to tune hyperparameters

In order to evaluate the model performance on unseen temporal conditions, an outer CV loop using a Leave-One-Date-Out (LODO) methodology was used. At each iteration, all labelled pixels from one acquisition date were put to the side for testing, while pixels from the remaining dates were used for model development. With the development data, an inner CV loop was used for hyperparameter tuning. For each outer iteration, the dates were put to the side were then split with the same LODO strategy: one date used for validation while the others were used for training. A 1:1 ratio between seagrass and non-seagrass pixels was imposed during training by randomly downsampling the majority class to prevent class imbalances. Hyperparameters were tuned in the inner loop using grids specific to each classifier: 96 combinations for the RF model and 384 combinations for the XGBoost model. The full list of tested hyperparameters is provided in *Appendix D*. In order to prevent information leakage, this nested structure made sure that the hyperparameter tuning was done only on the training data.

The model was then trained on the full development dataset of the respective outer fold using the best hyperparameter set from the inner loop. After that, predictions were produced for the testing date put to the side. The process was then repeated for each date. And the final model performance, using the best hyperparameters, was computed as the average over all outer folds, which gave an estimate of the model's ability to generalize to new acquisition dates.

3.6.4 Performance metrics

Model performance was evaluated using standard classification metrics derived from the confusion matrix (*Tab. 7*), which compares predicted classes with reference classes. In addition to these metrics, the macro-averaged F1-score (macro-F1) was used as the primary evaluation criterion (Pedregosa et al., 2011). Unlike other metrics, which can be biased toward the majority class, macro-F1 gives equal weight to each class by averaging the F1-scores of the seagrass and non-seagrass classes. This is particularly relevant in this study, where class imbalance may occur due to the spatial distribution of seagrass within the lagoon (Maxwell et al., 2018).

Table 7 - Confusion matrix structure

	Predicted Non-Seagrass	**Predicted seagrass**
Actual Non-seagrass	True negative (TN)	False Positive (FP)
Actual Seagrass	False Negative (FN)	True Positive (TP)

From this matrix, the following metrics were calculated for each class:

- *Precision*

$$Precision = \frac{TP}{TP + FP}$$

- *Recall*

$$Recall = \frac{TP}{TP + FN}$$

- *F1-score (F1)*

$$F1 = 2 \times \frac{Precision \times Recall}{Precision + Recall}$$

- Macro-F1

$$macro\ f1 = \frac{F1_{seagrass} + F1_{non-seagrass}}{2}$$

Performance metrics were computed for each fold of the LODO cross-validation and then averaged across all folds to provide a robust estimate of model performance. Variability between folds was also considered in order to assess the stability of the models under different conditions. This evaluation framework allows a consistent comparison between algorithms (RF and XGBoost) making sure that differences in performance are attributable to model and data characteristics rather than to specific training conditions.

Since outputs are class probabilities, a probability threshold is needed to convert to a binary class prediction. In this study, three thresholding strategies were considered: a standard threshold of 0.5, a threshold maximizing the macro-F1 score and a threshold maximizing the F1-score of the seagrass class. Threshold optimization was performed within each training fold using validation data and the selected threshold was then applied to the corresponding test fold. Thus, threshold selection does not bias performance evaluation and allows to evaluate the effect of threshold selection on the classification results.

The selection of the best model configuration for multi-temporal seagrass mapping is then made based on the model accuracy, class-specific performance and robustness that these metrics and evaluation techniques give. However, the reference classes used in the confusion matrix are from a model-derived seagrass reference map, not from independent field observations (*Section 3.2.3*). Consequently, the reported metrics should be interpreted as an evaluation of agreement with the available reference map, rather than as direct estimates of field-based ecological accuracy.

3.7 Temporal analysis of seagrass predictions

The temporal analysis aimed to reconstruct seasonal and interannual variability in mapped seagrass extent across the study sites. It was based on the probability outputs of the final Sentinel-2 classification pipeline selected (*Section 4.2*). For each acquisition date, the model produced a raster of seagrass presence probability. Binary prediction rasters were used only as secondary diagnostic products when necessary, while probability rasters were used as the main input for temporal analysis because they retain more information than a fixed binary classification.

The analysis included only shallow-water pixels that were valid. Land, clouds, invalid pixels, nodata values and masked deep-water areas were excluded following the preprocessing steps (*Section 3.3*). The probability values were restricted between zero and one. Pixel area was then used to convert probability sums and pixel counts into square kilometres. The metrics that result from this procedure are referred to as mapped seagrass extent and not seagrass cover because the model predicts presence probability, not percentage seagrass cover, biomass, or density.

3.7.1 Monthly aggregation and temporal trajectories

Single-date predictions can be affected by water clarity, tide level, sunglint, atmospheric correction residuals, or occasional classification errors. To reduce this short-term variability, monthly centred probability composites were produced. For each target month, we then averaged all valid predictions from a three-month centred window. For example, the January composite used observations from December, January and February.

For each monthly composite, we first calculated the mapped seagrass extent as probability-weighted surface area:

$$A_{pw} = a_{pix} \sum_{i=1}^{n} p_i$$

where a_{pix} is the pixel area in km^2 and p_i is the predicted seagrass probability of pixel i. This gives a continuous estimate of the mapped seagrass extent. Probability-thresholded mapped seagrass extent were also calculated using selected probability thresholds:

$$A_\tau = a_{pix} \sum_{i=1}^{n} \mathbf{1}(\, p_i \geq \tau)$$

where A_τ is the mapped extent at threshold τ and $\mathbf{1}(p_i \geq \tau)$ equals 1 when the pixel probability is greater than or equal to the threshold and 0 otherwise. Thresholds such as $p \geq 0.25$, $p \geq 0.50$ and $p \geq 0.75$ were used to assess threshold sensitivity and confidence in the mapped signal.

Then, we generated two temporal summaries. First, a seasonal curve was obtained by folding monthly composites from all years onto day-of-year. This is the average seasonal pattern for the whole time series Second, the same monthly composites were arranged along the full calendar time axis, from 2016 to 2026, to produce a chronological trajectory of mapped seagrass extent and highlight interannual variation. (Davies et al., 2024a, 2024b). Because the annual cycle repeats itself, the seasonal curve was smoothed with a circular Gaussian smoother with a bandwidth of 45 days. A non-circular Gaussian smoother with a bandwidth of 90 days was used to smooth the chronological curve. We used a descriptive bootstrap procedure to place estimates of uncertainty around the smoothed curves. The shaded interval is an 89% bootstrap interval, not to be confused with a Bayesian credible interval. The rate of change was obtained by taking the derivative of the smoothed trajectory (expressed in km^2 per week).

3.7.2 Annual composites and persistent extent

Annual probability composites were produced by averaging all valid probability rasters for each year. When needed, the annual composite was restricted to a fixed seasonal window to improve comparability between years. Pixels with too few valid observations were excluded from annual binary products. The annual mapped extent was determined using the same probability-weighted and thresholded area equations as previously described.

A threshold of $p \geq 0.50$ was used to represent, with moderate-confidence, mapped seagrass extent and a more conservative threshold of $p \geq 0.75$ was used to represent persistent seagrass extent. The thresholds represent the confidence level of the model's prediction and must not be taken as straightforward ecological categories. Annual maps were used to visualize the spatial structure of mapped seagrass probability through time and to compare patterns between years.

3.7.3 Spatial persistence and gain/loss analysis

Spatial persistence was calculated as the proportion of valid observations or composites in which a pixel exceeded a selected seagrass probability threshold:

$$P_i = \frac{N_{i,p\geq\tau}}{N_{i,valid}} \quad ,$$

where P_i is the persistence of pixel i, $N_{i,p\geq\tau}$ is the number of valid observations where the pixel exceeded threshold τ and $N_{i,valid}$ is the total number of valid observations for that pixel. High persistence indicates areas consistently mapped as seagrass, while intermediate persistence often corresponds to meadow margins where seagrass is more sparse, fragmented, or seasonally variable. However, intermediate persistence may also reflect uncertainty in the classification, especially near meadow boundaries.

Annual binary maps were compared between selected periods to create gain/loss maps. Each pixel was classified as either stable non-seagrass, loss, stable seagrass or gain. Loss was calculated as pixels classified as seagrass in first period and non seagrass in second period. Gain was for the opposite transition. Statistics for areas were then calculated for gain, loss, stable seagrass, stable non-seagrass, comparable area and net change. These maps were interpreted as changes in mapped high-confidence or persistent seagrass extent, rather than as a direct proof of ecological recovery or degradation.

3.8 Transferability to secondary sites

The final Sentinel-2 mapping pipeline was also applied to the four secondary study sites: Côte d'Or, Grande Anse, Sainte Anne and Baie Sainte Anne (*Section 3.1.2*). The objective was to assess whether a model trained and evaluated at Anse-aux-Pins could produce coherent seagrass predictions in nearby lagoons with different geomorphological, optical and ecological conditions.

No additional site-specific training was done with the secondary sites. The same preprocessing, feature extraction, classifier and probability thresholds used for Anse-aux-Pins were used without any modification. This allowed us to test the transferability of the workflow, rather than the performance of a locally updated model. The transferred model was used to generate maps of high-confidence seagrass extent for each secondary site. These outputs were then analyzed following the same general logic as for Anse-aux-Pins (*Section 3.7*). First, we analyzed the spatial distribution of valid Sentinel-2 observations to identify where temporal aggregation and mapped predictions were more or less reliable. Second, the transferred predictions were compared to the available MACCE reference map and recent Sentinel-2 imagery to evaluate the spatial coherence and site-specific generalization. Third, we extracted monthly trajectories and seasonal cycles when there were enough valid observations to test whether the transferred classifier produced temporally consistent patterns outside its training site.

This step was not an independent accuracy validation. The transferability was instead assessed by a descriptive comparison of model behavior across sites. Particular attention was given to: the location of high probability areas, the consistency of predictions over time and the possible occurrence of false detections in reef flats, bright sand, turbid water or optically complex shallow areas. The secondary-site analysis was therefore used to identify the conditions under which the Anse-aux-Pins-trained model appeared transferable and the conditions where site-specific calibration would likely be required. Results from this section should be interpreted as an exploratory assessment of model behavior across sites, rather than as definitive evidence of seagrass change at each location.

4. Results & discussions

The results presented in this chapter should be read in relation to the methodological framework (*Section 3*). The classifier was trained using reference labels extracted from the reference seagrass map product and the temporal analyses are therefore expressed as mapped seagrass extent rather than direct field-measured cover. This framing is especially important for the interpretation of model performance, meadow margins and transferability to secondary sites. However, the following sections focus primarily on the spatial and temporal patterns obtained from the Sentinel-2 workflow.

4.1 Spectral characteristics and feature separability of the classes

Before evaluating the classification models, the spectral and feature space of the labelled pixels was examined. This step aimed to verify whether the reference seagrass and non-seagrass classes showed coherent optical differences in the Sentinel-2 data and to identify which parts of the spectrum were most informative for classification. The analysis also tested whether these patterns were consistent between the two atmospheric correction approaches, DSF and RAdCor. This section therefore provides a first interpretation of the information available to the classifier, before the model performance comparison (*Section 4.2*).

4.1.1 Spectral behavior of seagrass and non-seagrass pixels

The median spectral profiles, with 95% interquartile range (IQ95), were first analyzed to evaluate whether seagrass and non-seagrass pixels from the reference map showed consistent spectral differences before classification. This was done with the dataset of both atmospheric correction : DSF and RAdCor. In both cases, the profiles showed the expected behavior for optically shallow tropical waters: reflectance is highest in the visible domain, peaks around the green band and decreases strongly towards the NIR and SWIR regions. This is consistent with shallow-water remote sensing, where blue and green wavelengths penetrate the water more efficiently, while red, NIR and SWIR wavelengths are highly absorbed by water (Lee et al., 1998; Hedley et al., 2018; Amone-Mabuto et al., 2024).

For the DSF version dataset (*Fig. 18*), non-seagrass pixels are slightly brighter that seagrass pixels in the coastal and blue bands, which may be related to sandy or unvegetated substrates. From the green band onward, seagrass pixels show higher reflectance than non-seagrass pixels. The contrast remains limited around 560 nm, where both classes reach their maximum reflectance, but becomes clearer in the red and red-edge regions.

In particular, the separation at 665 nm and 705 nm suggests that these wavelengths contain useful information for distinguishing vegetated benthic areas from non-vegetated or mixed substrates. This is consistent with the spectral behavior of photosynthetic vegetation, for which pigment absorption and canopy structure affect the red and red-edge domains (Thorhaug et al., 2007; Caballero et al., 2020; C. B. Lee et al., 2023).

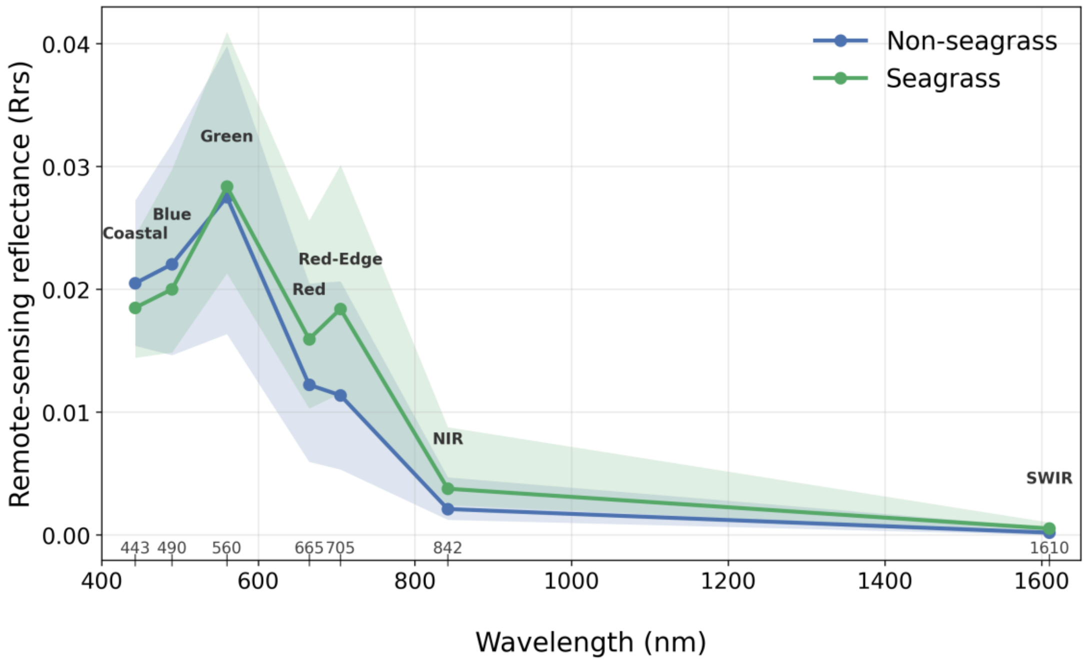

Figure 18 - Aggregated Sentinel-2 spectral profiles of seagrass and non-seagrass pixels for the DSF version dataset. Lines are median Rrs values across all selected acquisition dates, while shaded bands show the IQ95 of pixel reflectance.

The green band has a strong shallow-bottom signal but it is not obviously discriminant on its own, as both classes peak at that wavelength and their IQ95 overlap significantly. The same is true for coastal and blue bands which are a little bit more informative but still have some overlapping between classes. Both classes have low reflectance in the NIR, but the seagrass is still slightly higher than the non-seagrass, probably due to very shallow water, dense vegetation patches or mixed pixels. On the other hand, the SWIR band is close to zero for both classes and shows almost no direct class separation, as expected due to strong water absorption.

The RAdCor version dataset (*Fig. 19*) shows a very similar spectral pattern. The same green maximum, decrease towards NIR/SWIR and near-zero SWIR reflectance are observed. Seagrass is again generally brighter than non-seagrass from the green to the NIR bands, with the clearest visual separation in the red and red-edge regions. The comparison between DSF and RAdCor therefore indicates that the main spectral differences between the two classes were not created by a specific atmospheric correction approach, but were present in both corrected datasets. Apart from a slight difference around the green band, there is no major spectral change DSF and RAdCor.

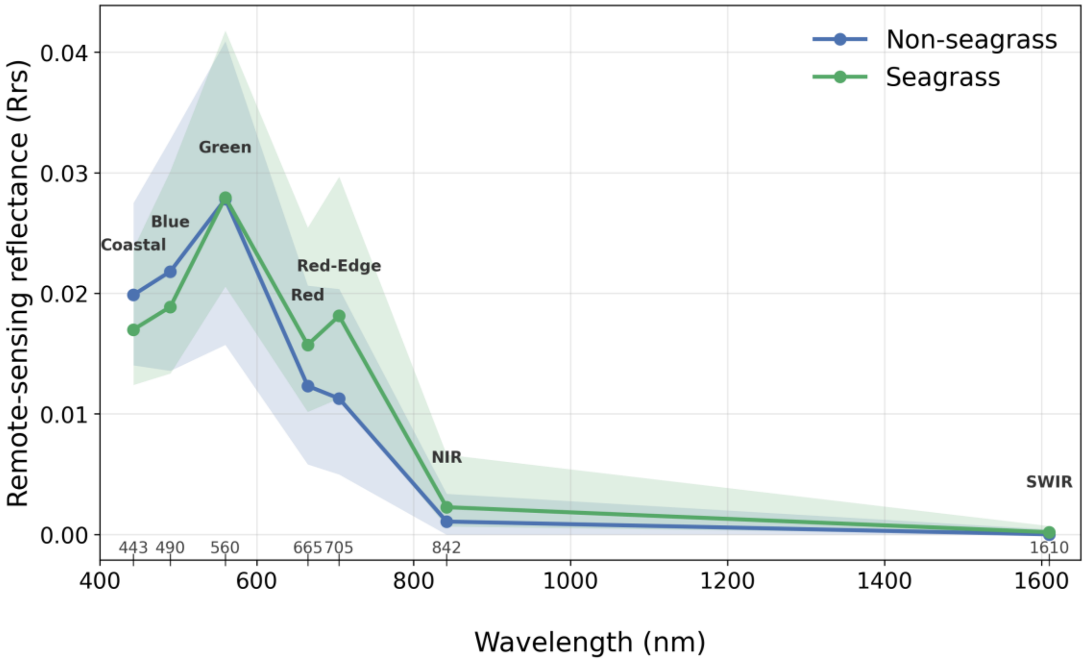

Figure 19 - Same as Figure 18, but for the RAdCor-corrected dataset.

Overall, these profiles show that seagrass and non-seagrass pixels differ spectrally, but with IQ95 overlap. Part of this overlap is expected in shallow tropical lagoons because of mixed pixels, water-depth variability, substrate heterogeneity and changes in water clarity (*Section 3.4.2*). However, it may also be reinforced by uncertainties in the reference map, because some pixels labelled as seagrass or non-seagrass may not correspond perfectly to their real field class. Despite this limitation, the main spectral pattern remains coherent across both atmospheric correction approaches. The red and red-edge bands appear to provide the clearest class contrast, while the blue and green bands remain important for capturing the shallow-water bottom signal but are more strongly overlapping. At first glance, the choice between DSF and RAdCor does not strongly modify the general spectral behaviour of the two classes. This supports the use of multiple spectral bands and derived features rather than relying on a single reflectance band for seagrass classification.

4.1.2 Effect of atmospheric correction on feature distributions

After the spectral behavior of seagrass and non-seagrass pixels (*Section 4.1.1*), we analyzed the effect of atmospheric correction on the feature space. This step is important because the classifier uses the corrected spectral bands and derived features as input. Therefore, changes caused by atmospheric correction can influence the separability and stability of the classes before any model comparison (*Section 4.2*). This effect is relevant in Anse-aux-Pins, because the lagoon is shallow, narrow and spatially heterogeneous. As explained in *Sections 3.3.2 and 3.4.2*, the signal measured by Sentinel-2 can be affected by water depth, bright sand, reef flats, land proximity, sun glint and residual atmospheric effects. RAdCor was developed to account for adjacency effects and surface heterogeneity, while DSF is the default ACOLITE atmospheric correction approach for aquatic applications (Vanhellemont, 2019; Castagna and Vanhellemont, 2025).

For the native Sentinel-2 bands, the differences between RAdCor and DSF are generally limited in the visible domain (*Fig. 20*). B01, B02, B03, B04 and B05 are mostly centered close to zero, although small class-dependent differences were visible. RAdCor tended to slightly reduce reflectance in the coastal, blue and red-edge bands, especially for seagrass pixels. In contrast, the green and red bands showed very small median differences, suggesting that both correction methods produced similar values in the main visible wavelengths used for shallow-bottom detection.

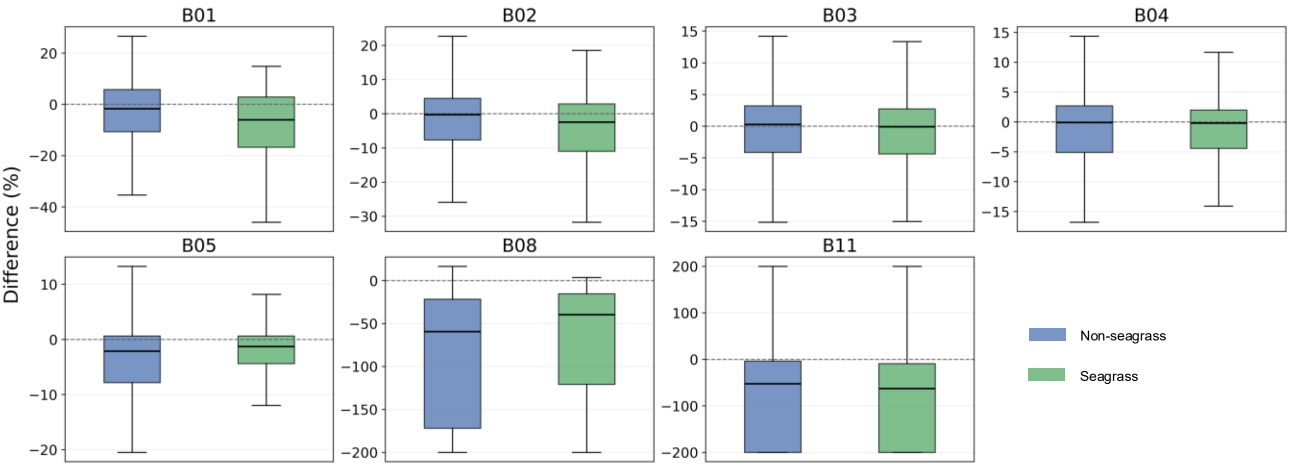

Figure 20 - Relative difference between DSF and RAdCor for native bands of Sentinel-2. Boxplots show the distribution of RAdCor minus DSF for paired labelled pixels, separately for seagrass and non-seagrass classes. Values are aggregated over all selected Sentinel-2 acquisition dates.

The largest changes among native bands are observed with B08 and B11. Both bands show negative differences, indicating lower values after RAdCor correction. This is coherent with RAdCor as it is intended to correct residual atmospheric, adjacency, surface or mixed-pixel effects especially in these wavelengths (Castagna & Vanhellemont, 2025). However, this result should only be interpreted as a modification of the feature space, not as evidence that one correction is better.

The 6 most affected features (*Fig. 21*) from the feature set (*Section 3.5*) are shown separately, while the complete table of differences is provided in *Appendix E*. These features showed stronger relative differences than the native bands. DII_B02_B03 and MEAN3x3_DII_B02_B03 all increased under RAdCor, with a stronger shift for non-seagrass than for seagrass. This shows that small changes in corrected visible bands can propagate into larger changes in depth-invariant indices. This is important because they are included to reduce water-column effects and improve discrimination (*Section 3.5.1*).

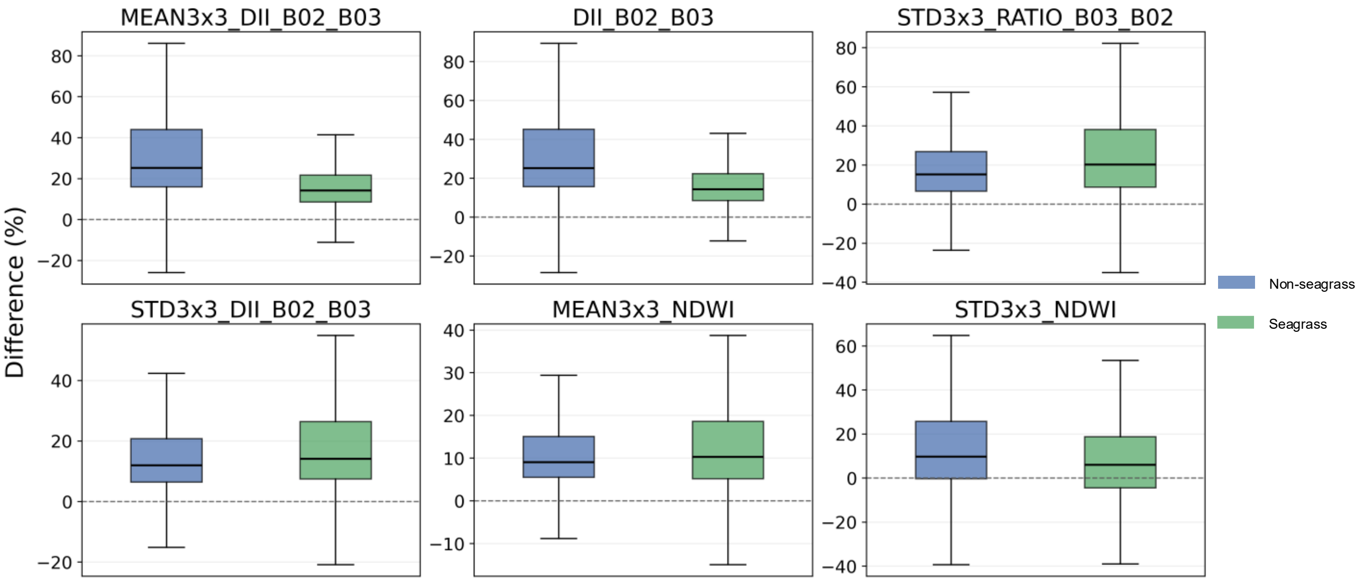

Figure 21 - Top 6 most affected derived features between DSF and RAdCor. Boxplots show the distribution of RAdCor minus DSF for the derived features with the biggest difference between atmospheric correction methods. Values are aggregated across all selected Sentinel-2 acquisition dates.

Other features also show marked changes after RAdCor correction. MEAN3x3_NDWI increased for both classes, which is consistent with the decrease observed in B08. The standard deviation features, especially STD3x3_RATIO_B03_B02, STD3x3_DII_B02_B03 and STD3x3_NDWI, also showed positive differences. This suggests that RAdCor did not only change average feature values, but also modified local spatial variability in the feature space. This may be linked to its correction of adjacency and surface heterogeneity effects, which are expected to be important in narrow and heterogeneous lagoons (Castagna & Vanhellemont, 2025). It also indicates that RAdCor modified the blue-green balance. Which is a very important spectral region because blue and green contain much of the information (*Section 3.4.1*).

Overall, atmospheric correction modified the feature space in a feature-dependent and class-dependent way. Native visible bands are only moderately affected, while B08, B11 and several derived features showed bigger differences. These results do not indicate whether DSF or RAdCor improves classification performance. They show that both corrections produce different input distributions, which may influence class separability, feature importance and model stability.

4.1.3 Feature separability and temporal stability

The selected features are analyzed according to two complementary criteria: their ability to separate seagrass from non-seagrass pixels and their stability across acquisition dates. This distinction is important because a feature can be very discriminative on one image but less useful for multi-temporal mapping if its distribution changes a lot between dates. For readability, only the most informative features are shown, the complete boxplot panels for all extracted features are in *Appendix F*.

For the DSF version dataset, some of the clearest class separations are observed with blue-green derived features, especially RATIO_B03_B02, DII_B02_B03, IDX_B03_B02 and MEAN3x3_RATIO_B03_B02 (*Fig. 22*). These variables show a relatively consistent difference between seagrass and non-seagrass pixels across most dates. Seagrass pixels generally had higher B03/B02 ratios and higher IDX_B03_B02 values, while DII_B02_B03 values were lower. This confirms that the blue-green contrast provides an important spectral signal for detecting submerged vegetation, as expected from the optical basis (*Section 3.4.1 and 4.1.1) that* blue wavelengths are strongly influenced by water-column attenuation and substrate brightness, while the green band retains more bottom information in shallow water. In this lagoon, non-seagrass pixels, which include sand and mixed substrates, tend to remain relatively brighter in the blue band, whereas seagrass pixels show a stronger green relative signal. This explains why ratios and normalized contrasts between B02 and B03 are more discriminative than either band alone (Thorhaug et al., 2007; Cingano et al., 2024).

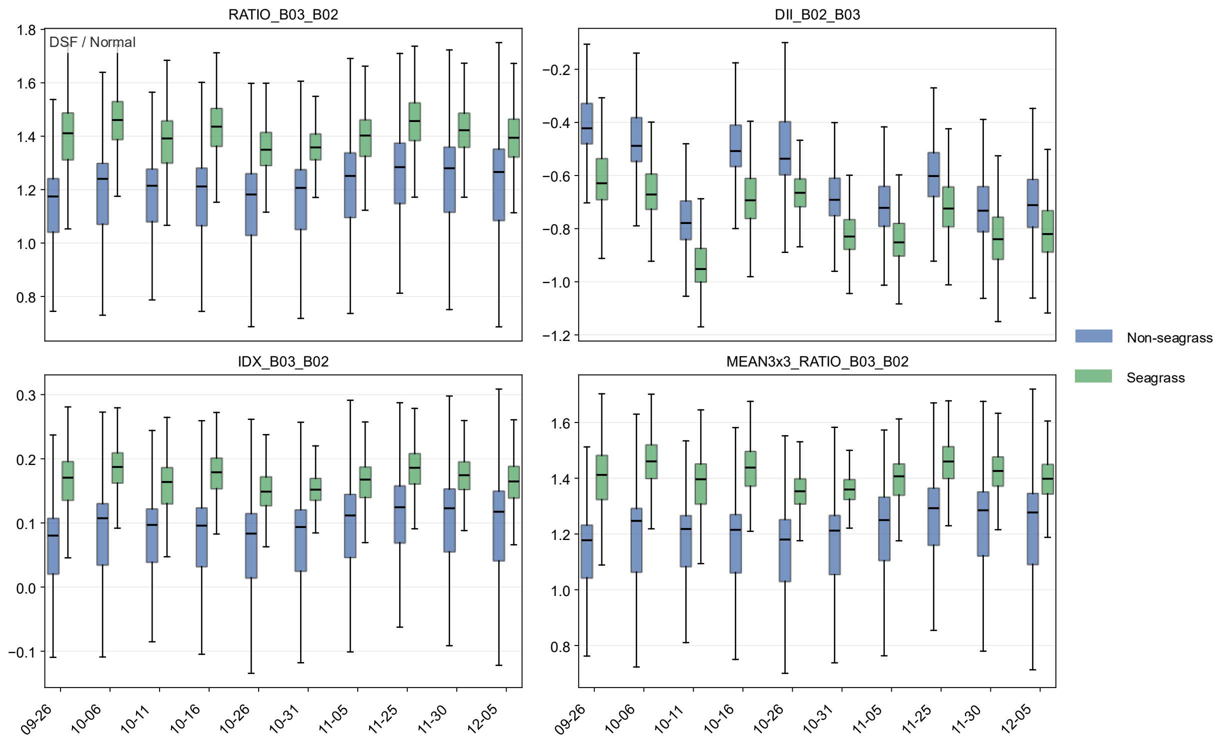

Figure 22 - Boxplots of the features with the best class separability for DSF. Features were selected using the mean absolute normalized median difference between seagrass and non-seagrass pixels across dates. Dates are shown as MM-DD.

The behavior of MEAN3x3_RATIO_B03_B02 also suggests that spatial context helps stabilize the spectral signal. Compared with the raw ratio, the 3 × 3 mean keeps the same class contrast but reduces part of the pixel-scale variability. This is relevant for Sentinel-2 because 10 m pixels can include mixed bottom types, small bare-sediment patches, or transitions between seagrass and non-seagrass areas. The 3 × 3 mean therefore probably captures the local coherence of meadow patches rather than only the spectral value of a single pixel. This explains why spatially averaged features can be useful in patchy lagoon environments, where seagrass boundaries are not perfectly aligned with the satellite pixel grid.

The most temporally unstable DSF features show a different pattern (*Fig. 23*). B08, MEAN3x3_NDWI, B05 and RATIO_B05_B03 vary strongly between acquisition dates. B08 remain close to zero for most dates, but increase strongly for seagrass pixels on some acquisitions, especially 10-06, 11-05 and 12-05. This is important because NIR reflectance should normally be strongly attenuated by water. High B08 values over pixels labelled as seagrass are therefore unlikely to represent a stable seagrass signal. They more probably indicate scene-specific effects such as very shallow water, residual sunglint, high bottom visibility, adjacency effects, mixed pixels, or remaining correction artefacts (Hedley et al., 2005; Vanhellemont, 2019).

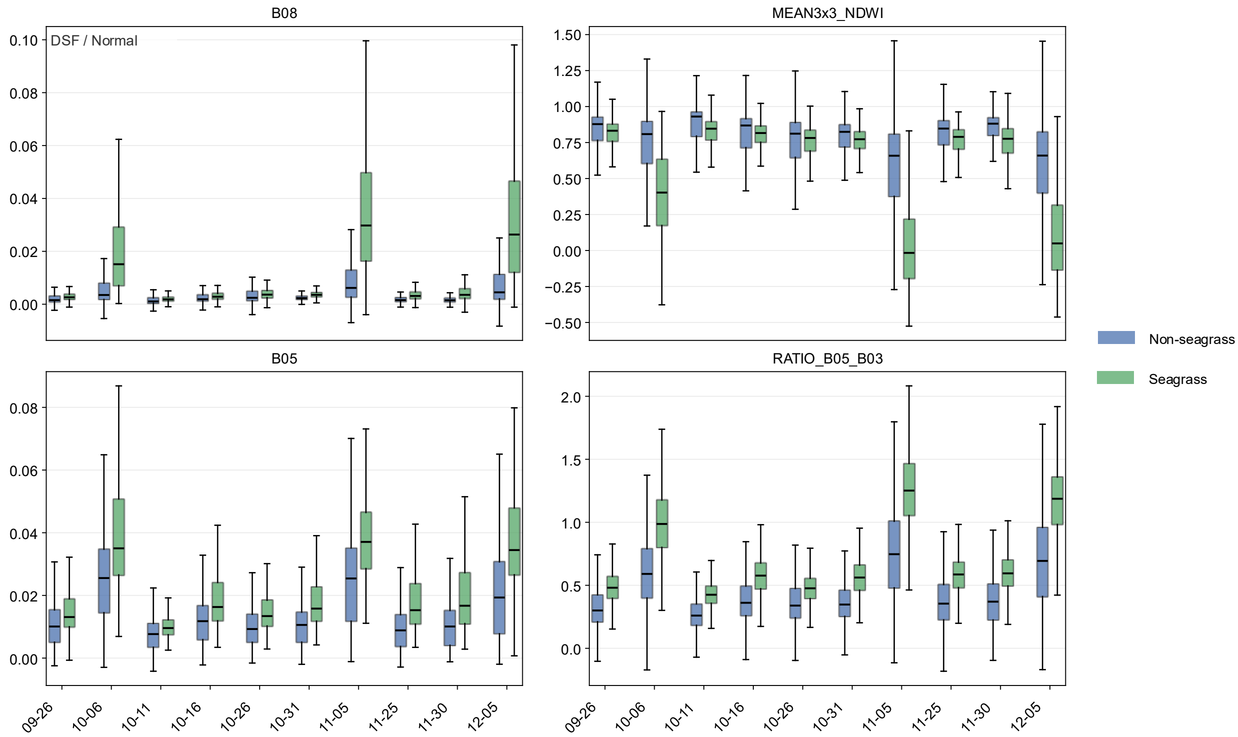

Figure 23 - Boxplots of the features with the highest temporal instability for DSF. Features were selected using the interquartile range across dates of the normalized class difference. Dates are shown as MM-DD.

The same applies to B05 and RATIO_B05_B03. The red-edge band can contain useful vegetation information and *Section 4.1.1* showed that red and red-edge wavelengths contribute to class contrast. However, in submerged environments these wavelengths are also more attenuated by water than blue and green wavelengths. Their usefulness therefore depends on water depth, water clarity and acquisition conditions. This explains why RATIO_B05_B03 can show good separation on some dates but weaker separation on others. These features are therefore discriminative under favorable optical conditions, but less robust across the full multi-date dataset.

MEAN3x3_NDWI also show temporal variability. Because NDWI uses the contrast between green and NIR reflectance and thus has the same sensitivity to scene-specific effects. Here, NDWI features appear more useful as indicators of scene conditions than as stable predictors of seagrass presence. Large changes in MEAN3x3_NDWI between dates may reflect differences in turbidity, sunglint residuals, depth-related bottom visibility or masking behavior rather than changes in benthic class. This supports the need to evaluate model performance with LODO-CV, because a model that relies too strongly on unstable features may perform well on some dates but generalize poorly on others.

For the RAdCor version dataset, the same blue-green features also show high class separation (*Fig. 24*). RATIO_B03_B02, IDX_B03_B02 and MEAN3x3_RATIO_B03_B02 remained higher for seagrass pixels, while DII_B02_B03 remained lower. This indicates that the main discriminative information was preserved after adjacency correction. The separation between classes is therefore not only an artefact of the DSF correction.

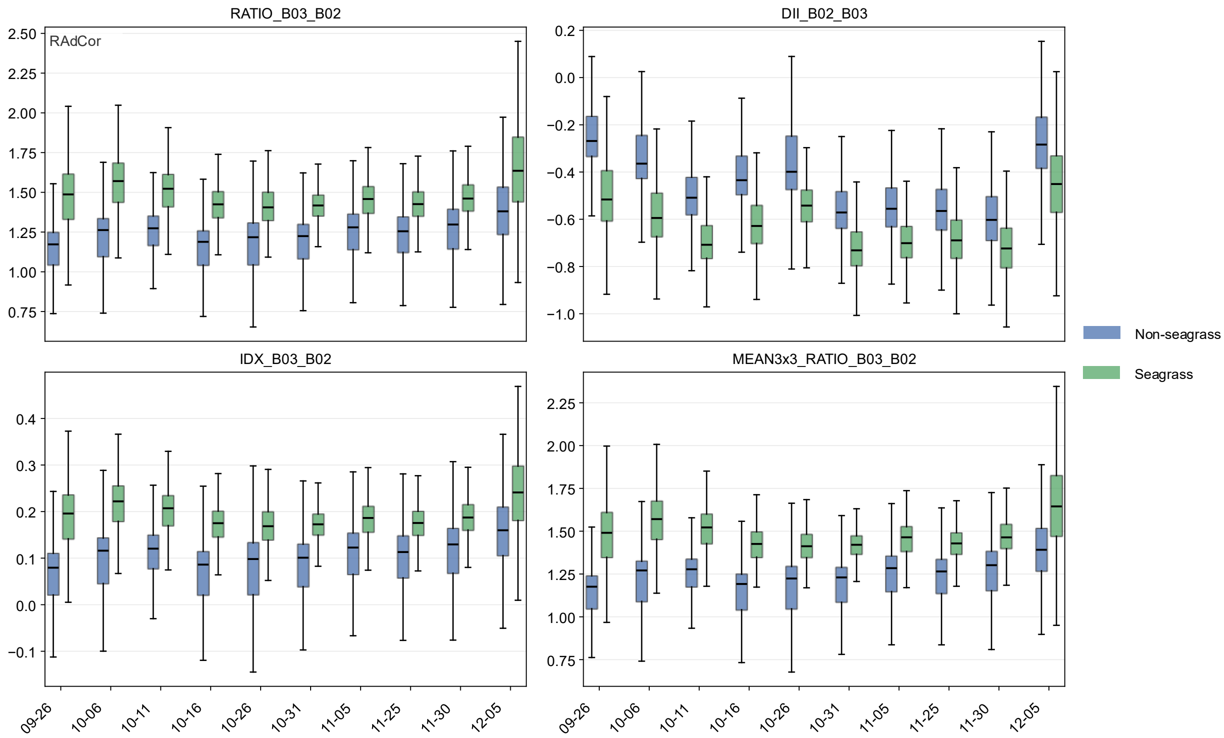

Figure 24 - Same as Figure 22, but for the RAdCor-corrected dataset.

Both atmospheric correction strategies retain the same general spectral basis for seagrass discrimination: the relative difference between blue and green reflectance. However, the RAdCor distributions were often wider than the DSF distributions. This is visible for RATIO_B03_B02 and MEAN3x3_RATIO_B03_B02, especially on 12-05, where both classes show larger dispersion. This suggests that RAdCor may increase some class contrasts, but also increase the spread of values under some acquisition conditions. One possible explanation is that adjacency correction modifies the blue and green bands differently depending on the surrounding land, reef flat, shallow sand or bright-water context. Since ratio features amplify relative differences between bands, small correction differences can produce larger changes in derived features. This is consistent with *Section 4.1.2*, where RAdCor had limited effects on most native visible bands but stronger effects on derived features.

The RAdCor unstable features confirm that adjacency correction does not remove all temporal variability (*Fig. 25*). B08, B05, RATIO_B05_B03 and MEAN3x3_NDWI remained dependent to the date. This means that part of the instability is not only caused by adjacency effects, but also by other factors that are difficult to correct fully, including water-column variability, bottom visibility, residual sunglint, acquisition geometry, turbidity and mixed pixels. Thus, RAdCor should not be interpreted as automatically producing a more stable feature space. It may improve some aspects of the correction, but the resulting feature distributions still depend on the conditions of each Sentinel-2 acquisition (Castagna and Vanhellemont, 2025).

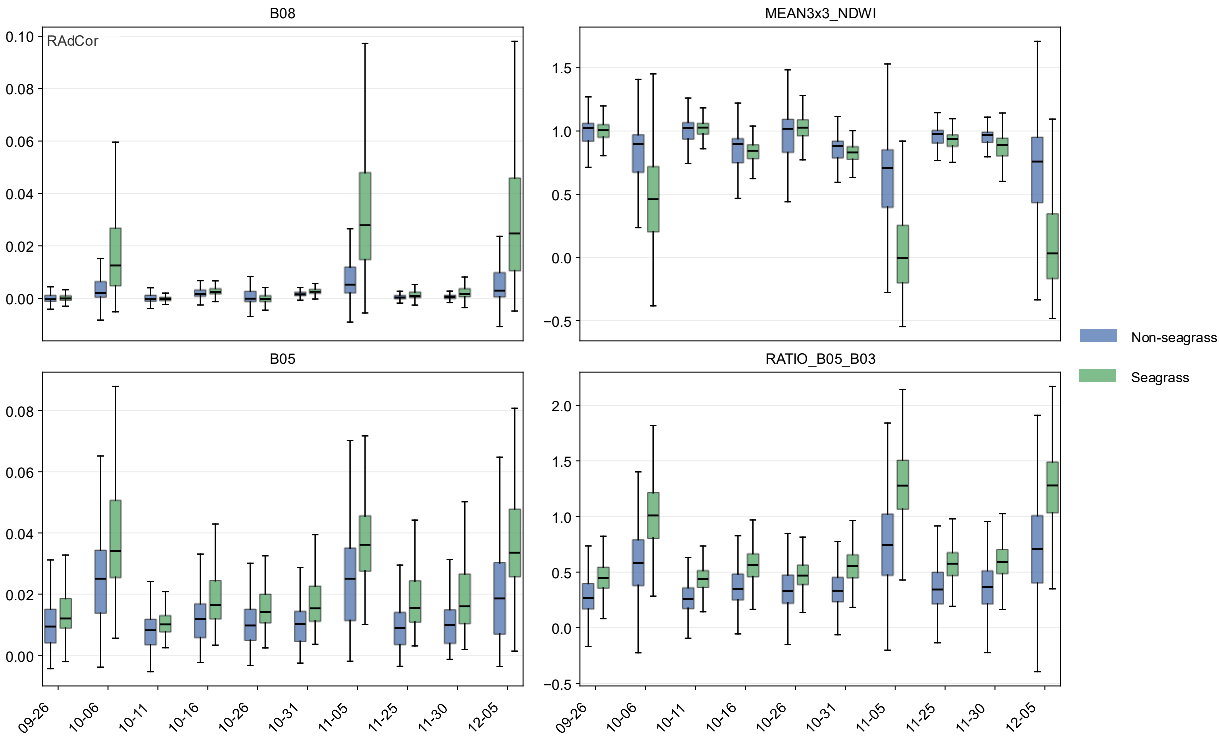

Figure 25 - Same as Figure 23, but for the RAdCor-corrected dataset.

Overall, both datasets identify the same main discriminative information, especially the blue-green contrast. This result shows that the separation between seagrass and non-seagrass is not specific to one correction method. However, this separability should still be interpreted relative to the available reference classes, because the labels were extracted from a model-derived seagrass map rather than from independent field observations. Some overlap between classes, especially near meadow margins or mixed pixels, may therefore reflect both real spectral ambiguity and uncertainty in the reference map.

Thus, the main difference between the two datasets is not the discriminative features but their temporal behavior. DSF tends to produce more compact and regular feature distributions. RAdCor sometimes improves the class contrast but also increases the dispersion. This means that the B02/B03 derived features provide the best trade-off between separability and temporal robustness in the classification analysis that follows. On the other hand, B08, B05 and NDWI features may still contain useful information for the classifier but should be interpreted with more caution as they seem to be more sensitive to specific acquisition conditions rather than to persistent presence of seagrass. This distinction is important for multi-temporal mapping, where the final model should detect seagrass consistently across dates rather than only maximize class separation under favorable conditions.

4.1.4 Implications for classification

The feature analysis shows that seagrass and non-seagrass pixels are spectrally different, but that their distributions is still overlapping. This confirms that seagrass mapping in optically shallow lagoons cannot rely on a single band, index, or threshold. Instead, it needs the combination of complementary features, including visible-band contrasts, spectral ratios, depth-related transformations and local spatial metrics (*Section 3.5*). This supports the use of machine-learning classifiers, which are better suited to non-linear and overlapping feature spaces in complex environments (Maxwell et al., 2018; Amone-Mabuto et al., 2024).

The results also show that feature separability and temporal robustness are not equivalent. B02/B03 features appear to provide the most stable discriminative information, while B05, B08 and NDWI features are more sensitive to acquisition-specific conditions. In addition, DSF and RAdCor preserve the same main spectral signal but modify the feature space differently. The next step is therefore to test whether these differences affect classification performance, robustness across dates and threshold sensitivity (*Section 4.2*).

4.2 Sentinel-2 classification performance and pipeline selection

4.2.1 Overall comparison of classification pipelines

First, the classification results are evaluated at the complete level. Each pipeline is defined by the combination of one atmospheric correction method, one machine-learning classifier and one probability thresholding strategy. This first comparison is necessary because the final binary seagrass maps depend on the interaction of these three components. Atmospheric correction modifies the input reflectance and features, the classifier determines how these features are separated and the threshold controls how probability outputs are converted into seagrass and non-seagrass classes.

In total, we evaluated 12 configurations. The comparison is based primarily on Macro-F1, with F1_1 also reported to describe the performance for the seagrass class specifically. Additional performance metrics and the selected hyperparameters of the final trained configurations, are provided in *Appendix G*. The four model combinations are DSF + RF, DSF + XGBoost, RAdCor + RF and RAdCor + XGBoost. For each combination, three probability thresholds are tested: a fixed threshold of 0.5, a threshold optimized to maximize macro-F1 and a threshold optimized to maximize the F1-score of the seagrass class (*Section 3.3.2, 3.6.2 and 3.6.4*). All configurations are evaluated using the same nested LODO-CV strategy (*Section 3.6.3*), so that performance are estimated on acquisition dates not used during model training or hyperparameter tuning.

Table 8 -Overall performance of the 12 Sentinel-2 classification configurations.

Atmospheric correction	Classifier	Threshold strategy	Selected Threshold	F1 seagrass	Macro-F1
DSF	RF	Fixed 0.5	0.500	0.700 ± 0.077	0.801 ± 0.065
		Macro-F1	0.582	0.699 ± 0.066	0.808 ± 0.054
		F1_1	0.563	0.700 ± 0.067	0.807 ± 0.055
	XGBoost	Fixed 0.5	0.500	0.701 ± 0.073	0.801 ± 0.062
		Macro-F1	0.586	0.703 ± 0.063	0.808 ± 0.048
		F1_1	0.565	0.702 ± 0.064	0.806 ± 0.051
RAdCor	RF	Fixed 0.5	0.500	0.662 ± 0.134	0.761 ± 0.123
		Macro-F1	0.677	0.663 ± 0.124	0.773 ± 0.106
		F1_1	0.643	0.661 ± 0.123	0.768 ± 0.110
	XGBoost	Fixed 0.5	0.500	0.673 ± 0.131	0.770 ± 0.122
		Macro-F1	0.655	0.669 ± 0.119	0.777 ± 0.102
		F1_1	0.635	0.673 ± 0.121	0.778 ± 0.105

This overview gives the basis for the following sections, where the effects of atmospheric correction, classifier choice and threshold optimization are analyzed separately.

4.2.2 Effect of atmospheric correction

Atmospheric correction is the first pipeline component evaluated separately because it acts before classification and modifies the feature distributions used by the models. As shown (*Section 4.1.2*), DSF and RAdCor produce the same general spectral behavior, but they affect some derived features differently. The objective here is therefore to test whether these differences translate into better classification performance.

DSF produce higher mean Macro-F1 values than RAdCor for all classifier and threshold combinations (*Fig. 26*). With RF, DSF reaching Macro-F1 values between 0.801 and 0.808, while RAdCor ranges between 0.761 and 0.773. The differences is around 0.035-0.040 depending on the threshold strategy. With XGBoost, the same pattern is observed: DSF ranges between 0.801 and 0.808, while RAdCor ranges between 0.770 and 0.778. The difference is slightly smaller than for RF, around 0.028-0.031, but remains consistent across the three threshold strategies.

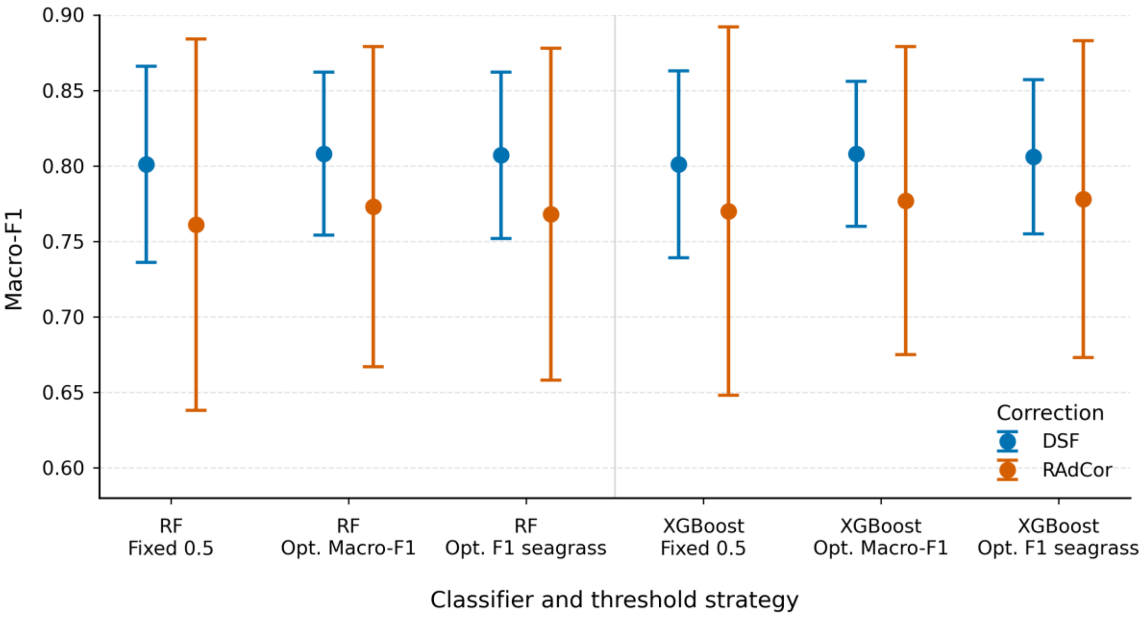

Figure 26 - Effect of atmospheric correction on mean Macro-F1 ± standard deviation for DSF and RAdCor for each model.

The error bars also show a clear difference in temporal stability. DSF has smaller standard deviations across the folds, while RAdCor shows wider variability for both RF and XGBoost. This indicates that RAdCor performance is more dependent on the acquisition date. This pattern is consistent with *Section 4.1.2* and *Section 4.1.3*, where RAdCor modified some derived features more and sometimes increased the distribution of features. Thus, under the conditions of this study, DSF produced a feature space that agrees better and more consistently with the reference seagrass map. RAdCor remains theoretically relevant for heterogeneous coastal environments (Castagna and Vanhellemont, 2025), but in this dataset its additional correction does not improve classification performance and increase date-to-date variability in some features.

4.2.3 Effect of the classification algorithm

The effect of the classifier is then evaluated to determine whether the performance is improved by the learning algorithm after the upstream correction.

Under DSF, RF and XGBoost produce almost identical Macro-F1 values (*Fig. 27*). With the fixed threshold, both classifiers reach 0.801. With the optimized Macro-F1 threshold, both reach 0.808 and with the optimized F1 seagrass threshold, RF reaches 0.807 while XGBoost reaches 0.806. The main difference is therefore not the mean performance, but the variability. XGBoost shows slightly smaller standard deviations than RF under DSF but the differences remains small and the error bars overlap.

For all threshold strategies under RAdCor, XGBoost performs slightly better than RF. Macro-F1 increases from 0.761 to 0.770 with the fixed 0.5 threshold, from 0.773 to 0.777 with the optimized Macro-F1 threshold and from 0.768 to 0.778 with the optimized F1 seagrass threshold. XGBoost also has a slightly lower variability than RF. Both classifiers are more variable in RAdCor than in DSF.

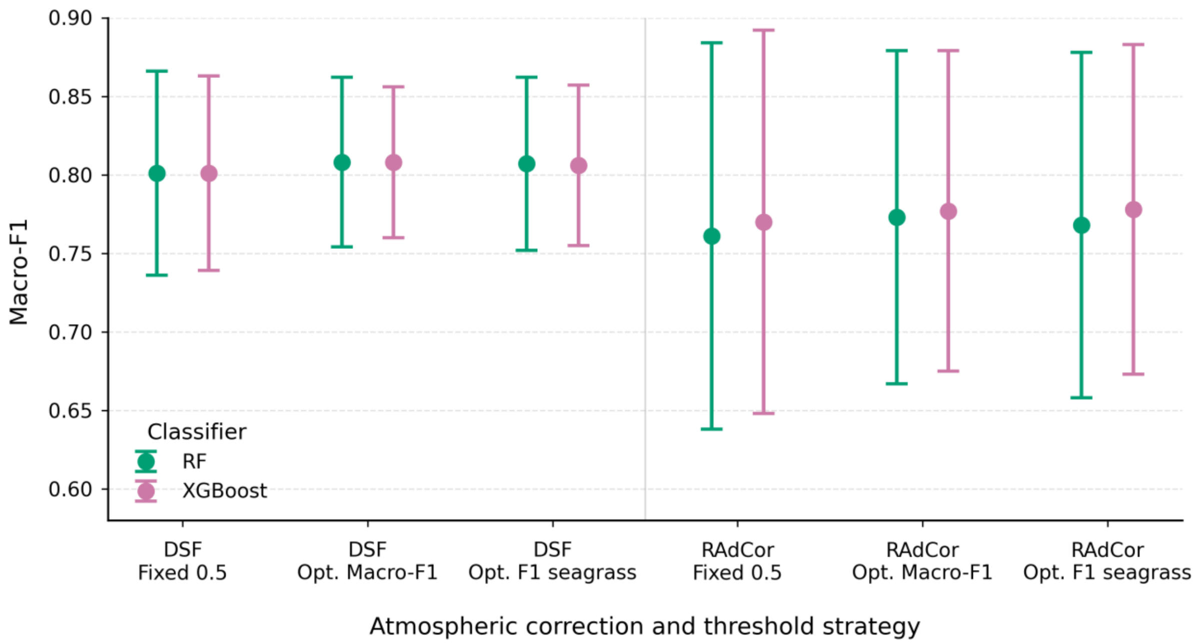

Figure 27 - Effect of classifier on mean Macro-F1 ± standard deviation for DSF and RAdCor for each model.

Classifier choice has a smaller effect than atmospheric correction. RF and XGBoost give similar results under DSF, suggesting that the DSF feature space is already stable for both algorithms. Under RAdCor, XGBoost slightly improves performance and variability, possibly because it capture more complex decision boundaries. However, this improvement remains small compared with variability. In this thesis, XGBoost therefore appears a bit more adapted, especially because it also reduces computation time by about a factor of ten in this implementation. This makes it a practical candidate for the final workflow, even if the performance difference with RF is small.

4.2.4 Effect of threshold optimization

After comparing atmospheric correction and classifier choice, the effect of threshold strategy is evaluated to determine whether the conversion from probabilities to binary seagrass maps affects model performance (*Fig. 28*).

For the DSF pipelines, threshold optimization only slightly improves Macro-F1 compared to the fixed 0.5 threshold. With RF, Macro-F1 improves from 0.801 to 0.808 with the Macro-F1 optimized threshold and to 0.807 with the F1 seagrass threshold. With XGBoost, Macro-F1 also improves from 0.801 to 0.808 with Macro-F1 optimization, while the F1 seagrass threshold gives a similar value of 0.806 The optimized DSF thresholds are just above 0.5, ranging from 0.56 to 0.59. For the RAdCor pipelines, threshold optimization also improves Macro-F1, but variability remains higher. With RF, Macro-F1 is increased from 0.761 to 0.773 with Macro-F1 optimization and the F1 seagrass threshold is 0.768. With XGBoost, Macro-F1 goes up to 0.777-0.778 from 0.770.

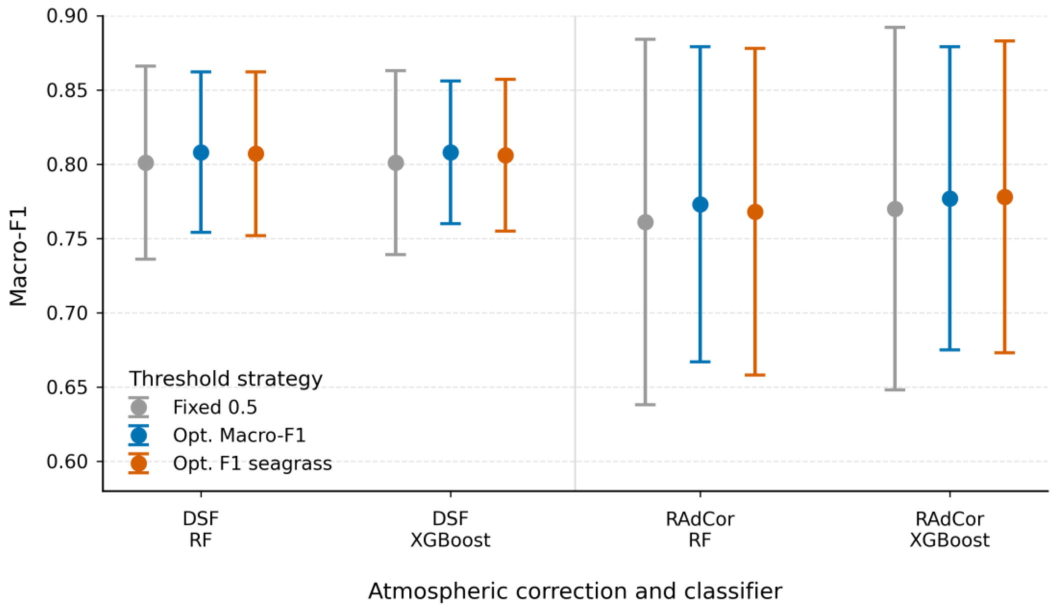

Figure 28 - Effect of threshold strategy on mean Macro-F1 ± standard deviation for DSF and RAdCor for each model.

Threshold optimization slightly improves Macro-F1, but it did not change the main structure. The Macro-F1 optimized threshold seems to be the most appropriate for this thesis as the goal is not only to detect seagrass pixels but also to keep a comparable discrimination between seagrass and non-seagrass. F1 seagrass optimization is also useful when the objective is to maximize the performance with respect to seagrass-class, but it may be less appropriate for balanced mapping if it induces more confusion with non-seagrass pixels. Hence, the threshold choice should be related to the mapping objective and should not be interpreted as globally optimal. Macro-F1 optimization provides the best trade-off for the final pipeline between seagrass detection, non-seagrass discrimination and temporal robustness.

4.2.5 Selection of the final Sentinel-2 classification pipeline

Among the tested configurations, DSF models consistently shows higher and more stable performance than RAdCor models (*Section 4.2.2*), while XGBoost shows similar or slightly better performance than RF and is faster to run in this implementation (*Section 4.2.3*). The Macro-F1 optimized threshold also provides the most balanced compromise between seagrass detection and non-seagrass discrimination (*Section 4.2.4*). Based on these comparisons, the final pipeline selected for the time-series analysis and transferability assessment is **DSF + XGBoost with the Macro-F1 optimized threshold**.

The selected pipeline has a mean Macro-F1 of 0.808 ± 0.048 and a mean F1 seagrass of 0.703 ± 0.063 over the outer LODO-CV folds. These values are among the highest of the tested configurations, but the choice is not based only on the maximum score. It is also based on the lower variability compared with RF, the slightly better seagrass F1 and the practical advantage of faster computation. The selected threshold is 0.586, which is a little above the standard 0.5 threshold. This confirms that a slightly more conservative threshold balances the detection of seagrass with avoiding too many false seagrass detections.

The confusion matrix of the selected pipeline shows the same trade-off (*Tab. 9*). Most non-seagrass pixels are correctly classified, with 188,883 TN and 25,434 FP. For the seagrass class, 42,775 pixels were correctly detected, while 10,510 pixels were classified as non-seagrass. This corresponds to a seagrass precision of about 0.63 and a seagrass recall of about 0.80. The model therefore detects most reference seagrass pixels, but still includes some pixels labelled as non-seagrass in the reference map. Here, this behavior is acceptable because the objective is to reconstruct mapped seagrass extent through time without using a too restrictive model that would miss marginal or sparse seagrass.

Table 9 - Confusion matrix of the selected classification pipeline (DSF + XGBoost + Macro-F1 optimized)

	Predicted Non-Seagrass	**Predicted seagrass**
Actual Non-seagrass	188,883	25,434
Actual Seagrass	10,510	42,775

However, the confusion matrix is an agreement with the available reference map, not a direct field accuracy assessment. Some apparent FP or FN may actually correspond to uncertainties in the reference map itself. Therefore, the real field performance could be higher or lower than the reported values, depending on the spatial accuracy of the reference labels. This point is important for the interpretation of the temporal analysis and transferability results, where model outputs are considered as mapped seagrass extent rather than direct field observations.

The feature contribution of the selected model is consistent with the feature analysis in *Section 4.1* (*Fig. 29*). The two most important predictors are MEAN3x3_RATIO_B03_B02 and IDX_B03_B02, contributing about 27.1% and 20.7% of total feature importance. Both features describe the blue-green contrast, confirming that this spectral region provides the main discriminative information. The high contribution of the 3 × 3 mean ratio also shows the importance of local spatial context in a patchy lagoon environment, where individual Sentinel-2 pixels can contain mixed substrates.

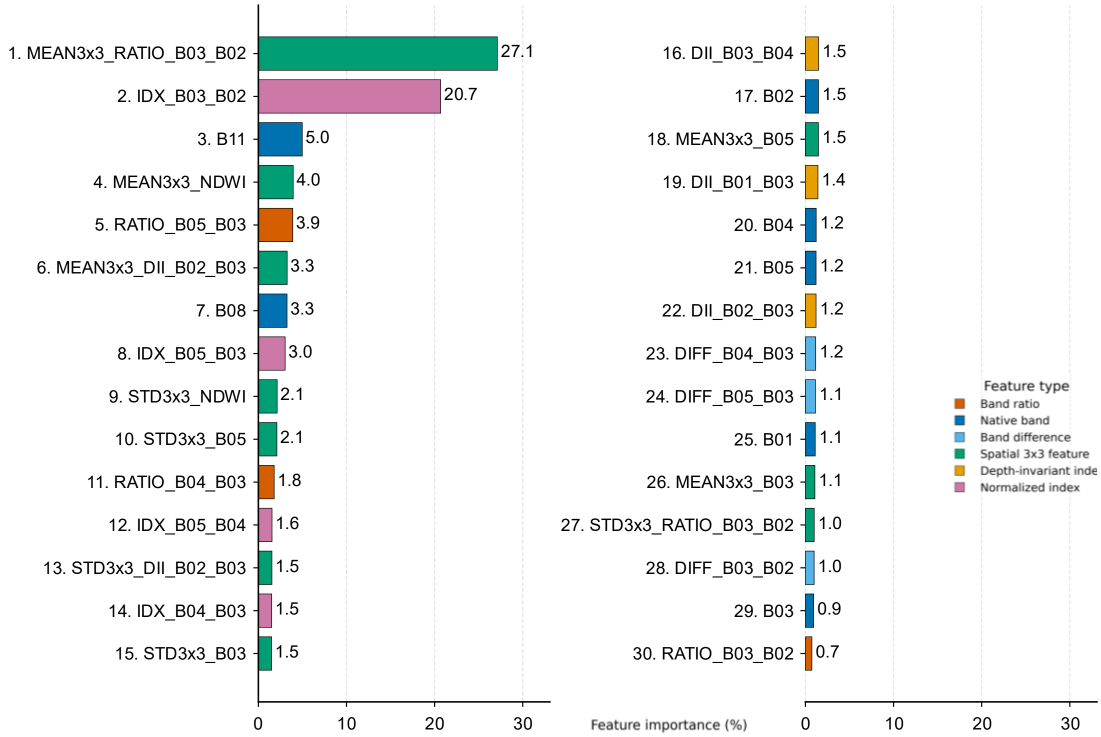

Figure 29 - Feature contribution of the selected classification pipeline. Relative feature importance of the final DSF + XGBoost model with the Macro-F1 optimized threshold.

Other contributing features are B11, MEAN3x3_NDWI, RATIO_B05_B03, MEAN3x3_DII_B02_B03 and B08. These features probably provide complementary information on shallow-water conditions, spectral contrast related to vegetation and local spatial variability. However, some features that appear discriminative in *Section 4.1* have low contribution in the final model. This means that some of the feature set has redundant information. Correlated predictors in tree-based models can share or mask importance (Chen & Guestrin, 2016; Maxwell et al., 2018). Thus, future work could test feature selection, correlation filtering, or feature ablation to determine whether a smaller and less redundant feature set could improve model stability and also transferability.

Overall, the selected DSF + XGBoost + Macro-F1 threshold pipeline provides the best compromise between performance, temporal robustness, computation time and interpretability for this thesis. It is therefore used for the Anse-aux-Pins time-series analysis in *Section 4.3* and for the exploratory transferability assessment in *Section 4.4*. Future work on the feature set could improve model stability and also transferability.

4.3 Sentinel-2 time-series analysis at Anse-aux-Pins

In this section, we use the selected DSF + XGBoost pipeline to map seagrass extent at Anse-aux-Pins, following the probability-based framework described in *Section 3.7*.

4.3.1 Temporal coverage and valid observations

Before interpreting seagrass area trends or gain/loss maps, the temporal and spatial reliability of the Sentinel-2 archive must be assessed. Optical monitoring of shallow coastal habitats depends not only on model performance, but also on the number of valid observations kept after preprocessing, cloud masking, sunglint correction and land/deep-water masking (*Section 3.3*).

The temporal distribution of valid observations is uneven through the archive (*Fig. 30*). Valid Sentinel-2 observations start in 2016, while 2026 is only available until May. These two years are therefore incomplete and should not be directly compared with full years such as 2018-2025. At the monthly scale, most months contain between one and six valid observations, with a one month reaching seven observations. However, some months contain no valid image, showing that the time series is not perfectly regular.

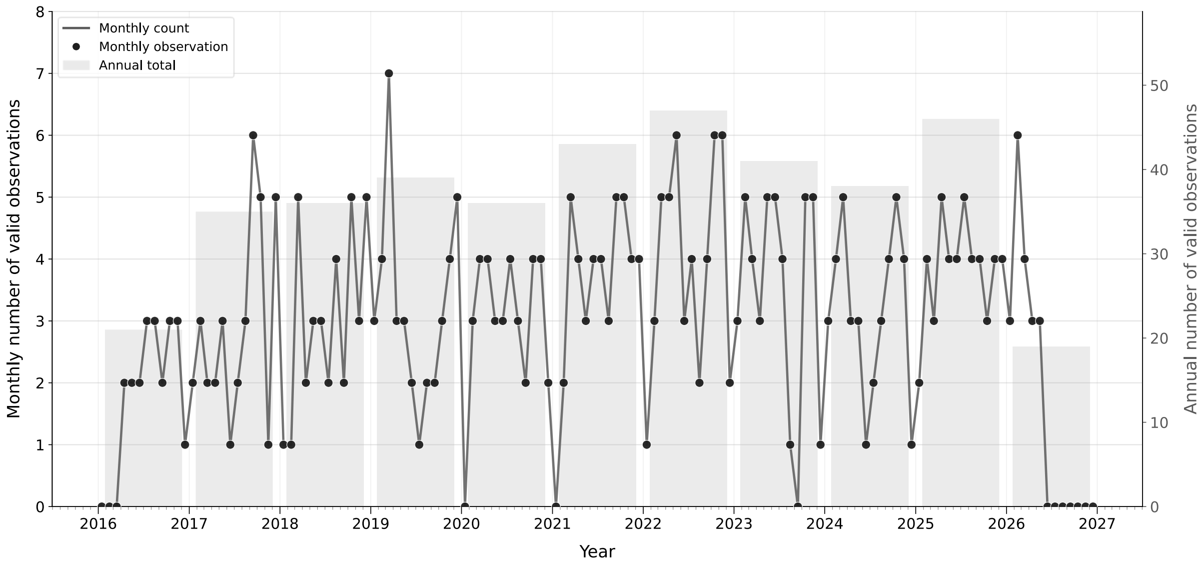

Figure 30 - Temporal distribution of valid Sentinel-2 observations used for the Anse-aux-Pins time series. Points and lines represent the number of valid observations per month after preprocessing and masking, while grey bars show annual totals.

At the annual scale, the number of valid observations increases after 2016 with the arrival of Sentinel-2B in addition to Sentinel-2A (*Section 3.2.1*) and is quite good for most complete years. This confirms that the Sentinel-2 archive provides a useful basis for long-term monitoring, but also shows that he density of sampling varies between years. The years with many valid observations are more robust because here are more acquisition conditions in the annual composites. In contrast, years with fewer acquisitions are more sensitive to individual scenes and may be biased if the available images were acquired during a specific season, after rainfall, under higher turbidity, or with residual sunglint.

The spatial distribution of valid observations is also uneven (*Fig. 31*). Most of the central lagoon reaches high observation counts, generally around 250-320 valid observations over the full time series. This indicates that the main shallow-water area used for seagrass monitoring is well represented. Persistent seagrass patterns detected in this central zone can therefore be interpreted with relatively high confidence.

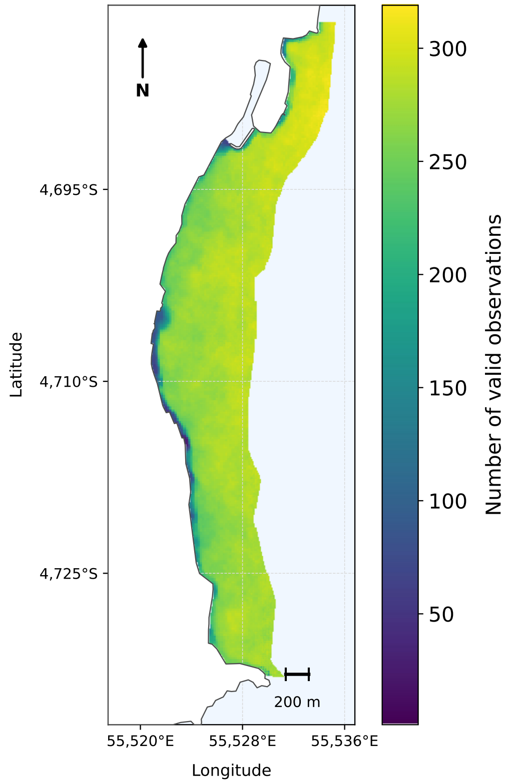

Figure 31 - Spatial distribution of valid counts of Sentinel-2 acquisitions over the Anse aux Pins lagoon. Pixel values indicate the number of valid observations after preprocessing and masking. Higher values indicate area where seagrass predictions and change maps are expected to be more reliable.

Lower counts are observed close to the coastline, likely due to shallow sandbeds being falsely detected by the cloud mask and removed during preprocessing. These areas should therefore be interpreted with caution, as fewer valid observations are available near the coast and along some meadow margins. These zones may reflect masking errors over bright sandy bottoms rather than true ecological dynamics during analyses . As a perspective, future processing can mitigate this issue by tuning cloud-mask parameters.

The Sentinel-2 archive is enough for the analysis of long-term seagrass dynamics at Anse-aux-Pins, especially between 2018 and 2025 and in the central lagoon. However, we should take its temporal and spatial heterogeneity into account when interpreting the following results. This supports the use of monthly and annual aggregation (*Section 3.7.1 and 3.7.2*), as these composites reduce the influence of individual images affected by residual clouds, sunglint, turbidity or masking artefacts. Thus long-term and spatially persistent patterns are more robust than isolated changes observed in incomplete years or low-observation areas.

4.3.2 Chronological evolution

The chronological evolution of satellite detected high-confidence ($p \geq 0.75$) seagrass area at Anse-aux-Pins shows strong variability between 2016 and 2026 (*Fig. 32*). As discussed (*Section 4.3.1*), the first and last years of the archive are incomplete and should therefore be interpreted cautiously. The seagrass area does not follow a simple trajectory. Instead, it shows repeated phases of expansion and contraction, with most monthly estimates ranging between approximately 0.5 and 1.0 km^2. Several isolated peaks exceed 1.2 km^2, especially around 2017, 2020-2021 and 2023-2024.

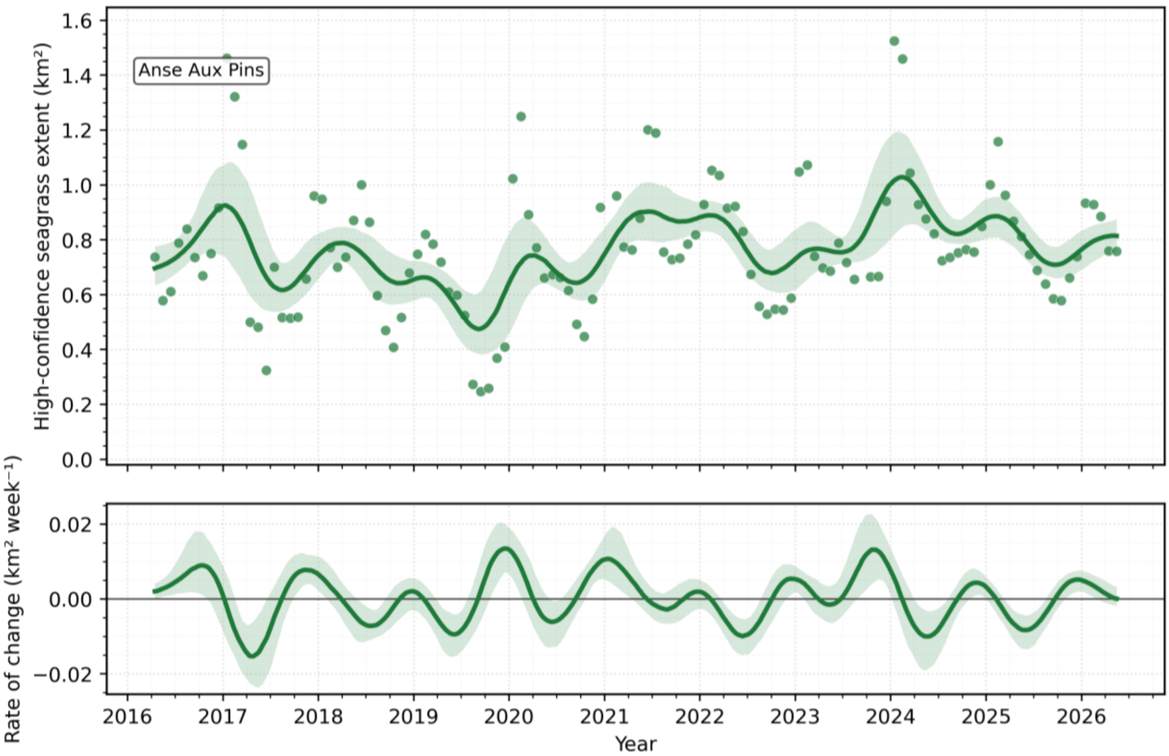

Figure 32 - Chronological evolution of high-confidence ($p \geq 0.75$) mapped seagrass area at Anse-aux-Pins from 2016 to 2026. The points are monthly estimates from Sentinel-2. The solid line is the smoothed temporal trajectory and the shaded envelope the 89% bootstrap confidence interval. The bottom panel shows the estimated rate of change, positive values mean apparent expansion, negative values mean apparent contraction.

The smoothed curve suggests a slight overall increase over the full period, from about 0.7 km^2 in 2016 to approximately 0.8-0.9 km^2 in 2026. But this tendency is small compared to the size of seasonal and interannual fluctuations. There are some apparent declines along the trajectory, especially between 2017 and 2019, in 2022 and after the 2023-2024 maximum. We can see the same pattern in the rate-of-change panel, with positive phases around early 2020, early 2021 and late 2023-early 2024 and negative phases around 2017, late 2019, 2022 and 2024-2025.

Some anomalies are close to major climate events in the Indian Ocean. The 2019-2020 and 2023-2024 periods coincide with positive Indian Ocean Dipole (IOD) phases, which are associated with warmer conditions and higher sea level in the WIO, while the eastern Indian Ocean (EIO) becomes cooler and has lower sea level (NASA/JPL, 2026).

This regional context is important because seagrass meadows are sensitive to temperature, water depth and light availability. Warmer water can increase physiological stress and higher water levels, changed currents or sediment resuspension can reduce light reaching the canopy (Short & Neckles, 1999; Zabarte-Maeztu et al., 2021a). However this does not demonstrate that the IOD was responsible for the changes mapped at Anse-aux-Pins, because the time series alone cannot distinguish between climatic effects and local or methodological variability.

The 2020-2023 period followed several La Niña phases, which are part of the El Niño-Southern Oscillation (ENSO) (NOAA CPC, 2026b). La Niña is usually associated with the cool phase of ENSO in the tropical Pacific, but it can also affect the global atmospheric circulation and rain and temperature patterns. In the present time series this period corresponds to relatively high mapped seagrass extent and several positive phases in the rate-of-change curve . This doesn't mean direct benefits of La Niña to seagrass condition at Anse-aux-Pins but it provides useful climatic context before the change towards El Niño conditions in 2023-2024.

The 2023-2024 period also occurred during El Niño conditions, which are part of ENSO (NOAA CPC, 2026b), which can influence temperature and rainfall patterns globally, although local effects vary between regions. This does not demonstrate causality, but it provides a climatic context for interpreting the 2023-2024 peak and the following apparent decline. The decline after 2023-2024 should also be interpreted in relation to exceptional regional ocean conditions. The WIO experienced severe coral bleaching in 2024, associated with El Niño, positive IOD conditions and record global temperatures as combined drivers of record-high sea surface temperatures (SST) and thermal stress (ICRI/CORDIO, 2024). These stressors can affect seagrass directly through thermal stress and reduced productivity, or indirectly through reef degradation, where present, wave attenuation changes, sediment mobility and water-quality degradation (Hughes et al., 2017; Short & Neckles, 1999; Zabarte-Maeztu et al., 2021b). (Because reef condition was not assessed at Anse-aux-Pins, this indirect reef-related pathway cannot be confirmed locally.)

In addition to possible ecological stress, these climatic anomalies may also affect the detectability by modifying water clarity, turbidity, water depth or bottom visibility (*Section 3.4.2*). The decline after 2023-2024 should therefore be interpreted with caution, as a potential combination of ecological stress, changing observation conditions and classification uncertainty, rather than as confirmed seagrass loss.

Other changes are less clearly linked to large-scale climate events. For example, the decrease between 2017 and 2019 occurs before the strong 2019 positive IOD episode. This suggests that local or methodological factors were also involved, such as sediment redistribution, rainfall-driven turbidity, seasonal wind exposure, coastal works, cloud-mask errors, classification uncertainty, or differences in valid image availability. These factors are relevant in Seychelles because erosion, flooding and coastal vulnerability are identified as major management concerns for the country's low-lying coastal zones (Government of Seychelles, 2019)

At the time of writing, climate forecasts also indicated a high probability of a new El Niño event developing into late 2026 and early 2027. NOAA CPC reported a 82% probability of El Niño emergence during May-July 2026 and a 96% probability of persistence during December 2026-February 2027, while WMO also indicated that El Niño conditions were expected to develop from mid-2026 forward (NOAA CPC, 2026a; WMO, 2026). Continued observations after 2026 could help assess whether a new ENSO event, potentially combined with positive IOD conditions or regional marine heat stress, affects the mapped seagrass extent at Anse-aux-Pins. Future monitoring should evaluate if the persistent mapped core remains stable, if marginal areas contract or expand and if the seasonal envelope identified in *Section 4.3.3* shifts under new climatic conditions.

Thus, this figure suggests Anse-aux-Pins is a dynamic lagoon system with strong seasonal-to-interannual variability and a weak increasing trend in high confidence seagrass area. Major peaks and apparent declines may coincide with IOD, ENSO or regional marine heat-stress periods, but they should also be interpreted in relation to local processes, observation conditions and classification uncertainty. However, these results should be interpreted as a satellite estimate of seagrass area and not a direct estimate of seagrass cover, density or biomass.

4.3.3 Seasonal cycle

After the chronological analysis of mapped seagrass extent (*Section 4.3.2*), the seasonal analysis was used to identify the average intra-annual signal at Anse aux Pins. This analysis combines two outputs: the aggregated monthly seasonal curve and the February-October seasonal envelope map. Together, they describe when the mapped meadow expands or contracts during the year and where this seasonal variability occurs.

The aggregated seasonal curve shows an annual cycle in high-confidence ($p \geq 0.75$) seagrass extent (*Fig. 33*). Over the 2016-2026 period, the highest mean extent happens at the beginning of the year, with a maximum around February of approximately 0.9-0.95 km^2. From March onwards, the extent gradually decreases and reaches a minimum around September-October, at approximately 0.6-0.65 km^2. It then increases again from October to December-January. The rate-of-change panel confirms this pattern, with negative values from March to September and positive values from October to February.

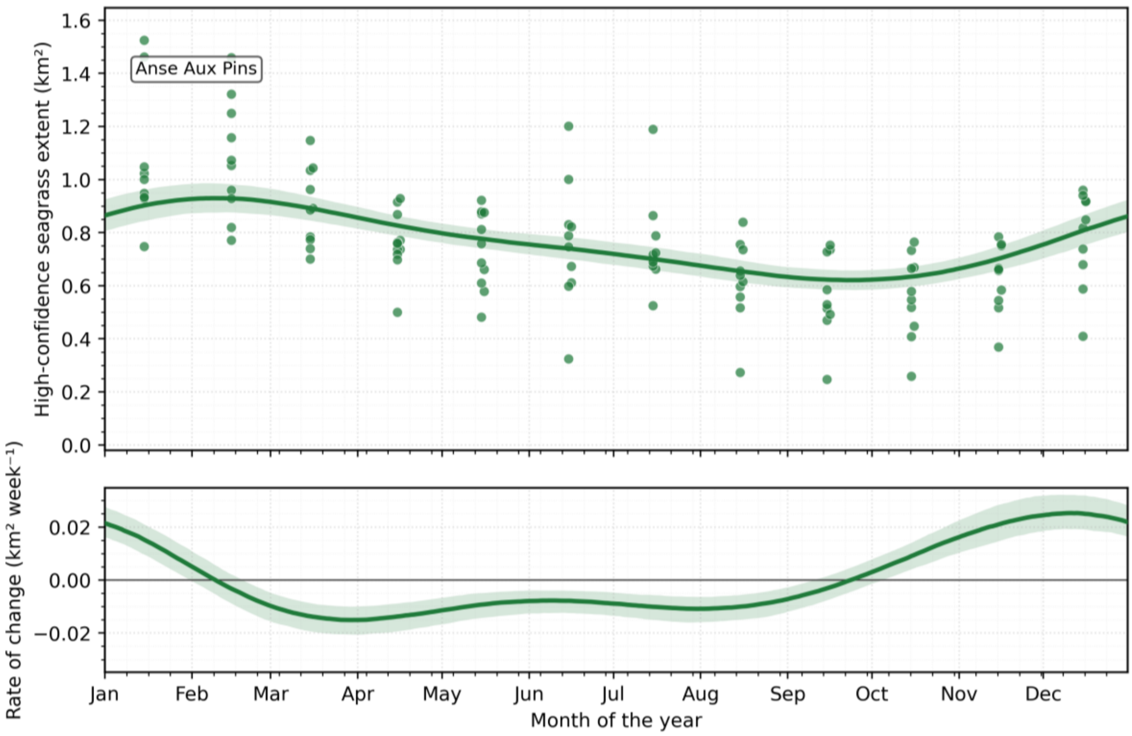

Figure 33 - Monthly seasonal cycle of high-confidence ($p \geq 0.75$) mapped seagrass extent at Anse aux Pins from 2016 to 2026. Upper panel is the mean monthly high-confidence seagrass extent, with an 89% bootstrap confidence interval from interannual variability and threshold sensitivity. The lower panel is the mean rate of change, showing the average periods of seasonal contraction and expansion. The curve is seasonal signal in extent and should not be interpreted as a direct seagrass biomass.

The timing of maximum is important because the mapped seagrass extent peaks around February, while the annual SST maximum generally occurs later, around April. Therefore, the seasonal cycle is not directly in phase with the SST maximum. This means that temperature alone is not the cause for the observed pattern. Instead, the February maximum is a combination of seasonal meadow development and better detectability (i.e., lower turbidity, better light penetration, reduced sediment resuspension, more favorable water-column conditions and increased continuity of marginal seagrass). On the other hand, the decline towards September-October could be due to a decrease in detectability or continuity of marginal areas, for example because of turbidity related to rainfall, sediment dynamics, hydrodynamic disturbance or lower optical penetration.

The February-October envelope map shows that this seasonal signal is mainly located around the margins of the persistent meadow (*Fig. 34*). A large part of the central and southern coastal meadow remains classified as stable seagrass, meaning that it is detected during both seasonal peaks. In contrast, February expansion areas are mainly located along the offshore edge and in parts of the central and northern study area. In the central part between 4,710° and 4,725°, this zone overlaps with areas later identified as long-term recovery up to 2026 (*Section 4.3.5*). However, because the seasonal map is based over the full 2016-2026 period, it does not show this recovery process directly. Instead, it indicates that these areas belong to the seasonal envelope of the meadow, where seagrass expression is more variable through the year. The seasonal maximum should therefore be interpreted as a potential high-season envelope, corresponding to areas where seagrass may expand, become denser, or become more detectable during the favorable season, rather than as an average expansion area. Areas classified as contraction from October are very limited and almost invisible at the scale of the map, suggesting that this class should not be over-interpreted.

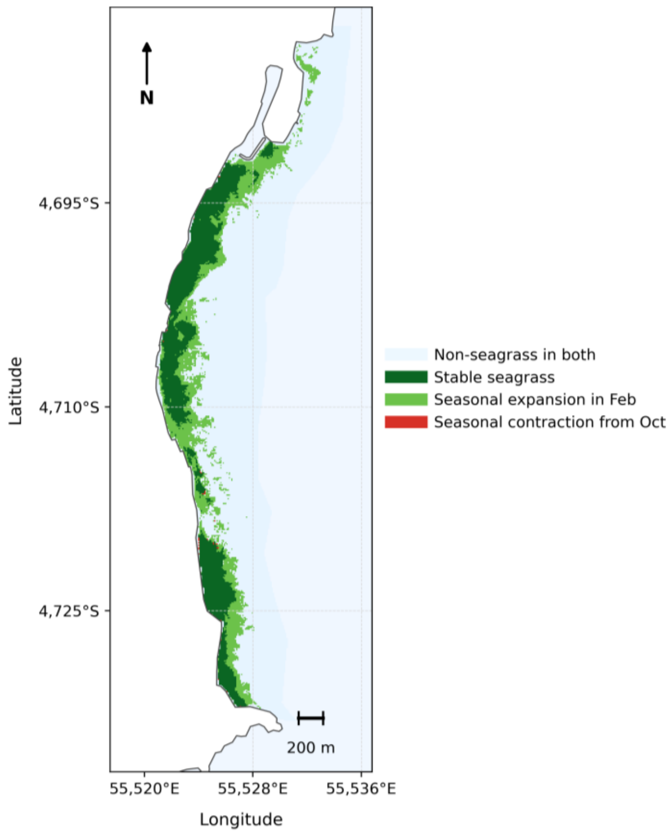

Figure 34 - Seasonal envelope of high-confidence ($p \geq 0.75$) mapped seagrass extent at Anse-aux-Pins, showing the potential zone where seagrass may expand during the seasonal maximum relative to the seasonal minimum.

This spatial structure is ecologically relevant. The stable seagrass core likely represents the most persistent part of the meadow, because it remains detectable across different seasonal conditions. These areas may therefore be considered candidate priority zones for conservation, monitoring and protection. They probably provide the most continuous habitat function through the year and supports long-term ecosystem services such as habitat provision, sediment stabilization and carbon storage.

February expansion zone means something else. It represents the seasonal envelope of the meadow, where the presence of seagrass seems to be more variable, fragmented or sensitive to environmental conditions. These are marginal areas and may be sparse or edge seagrass which is more continuous or detectable during favorable periods. Since the reference data were collected during the October-November period, close to the seasonal minimum, these February expansion areas should be interpreted with more caution than the stable core, since they may partly reflect seasonal changes in detectability related to turbidity, water depth, sediment resuspension or acquisition conditions. But from a management point of view it should not be forgotten. Even if they are more uncertain than the persistent core, meadow margins could be zones of potential expansion, seasonal habitat availability and ecological connectivity. They could also serve as early warning areas, because changes in these margins could show stress or recovery before changes are seen in the persistent core. The most useful approach therefore would be to take the persistent core as the main conservation baseline, but to use the seasonal envelope as a target area for monitoring and future validation.

Overall the seasonal analysis shows a stable seagrass core surrounded by a more dynamic marginal envelope. Results should be interpreted as a seasonal signal in mapped extent rather than a direct measurement of seagrass biomass. But this does not reduce the ecological importance of the pattern. Rather it shows that the February maximum and September-October minimum probably represent a combination of true meadow dynamics, seasonal detectability and timing of reference data. Thus, this seasonal baseline is critical to separate long-term change from typical intra-annual variability and identifying where should be prioritized for protection, monitoring or targeted field surveys.

4.3.4 Annual distribution

The annual maps provide a spatial complement to the chronological and seasonal analyses (*Sections 4.3.2 and 4.3.3*). While the previous subsections showed temporal changes in mapped seagrass area, the annual maps show where the persistent seagrass structures ($p \geq 0.75$) are in the lagoon. Three representative years were selected: 2017 for the early Sentinel-2 period, 2021 for the reference map period and 2025 for the recent period. The full annual map series from 2016 to 2026 is provided in *Appendix H*.

The three maps show that a seagrass core was repeatedly detected along the coastline of the lagoon, making a narrow meadow band (*Fig. 35*). In 2017, this core was already visible, with continuous patches in the northern and central sectors and a second important patch in the southern part of the bay. However, the central-southern section was more discontinuous, with several gaps and fragmented patches. In 2021, the meadow appeared more spatially coherent, especially in the northern and central sectors, where the seagrass belt was broader and more connected. This year is useful as a spatial consistency check with the reference map period, but it should not be considered a fully independent validation because the same period contributed to model development or evaluation. In 2025, the persistent core remained present along most of the same coastal zone, although the meadow appeared more irregular, with more internal gaps and a less regular offshore boundary.

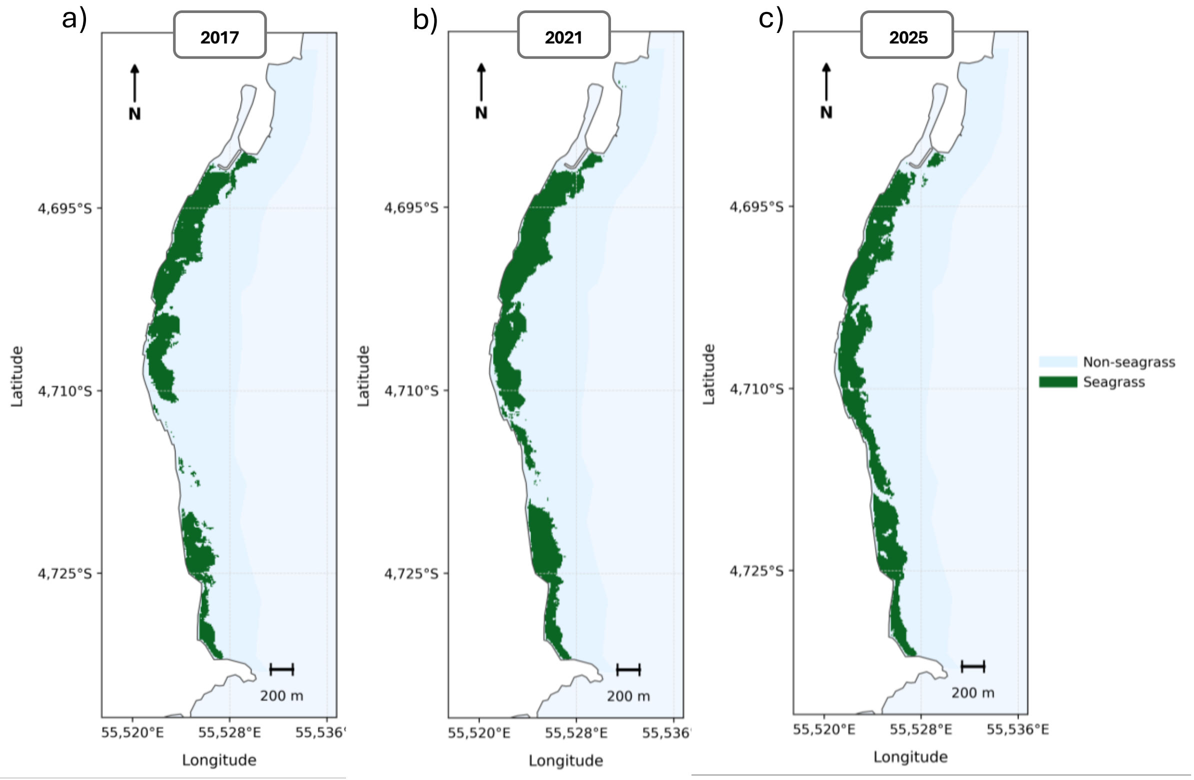

Figure 35 - Annual core seagrass ($p \geq 0.75$) maps for a) 2017, b) 2021 and c) 2025 at Anse-aux-Pins. Green pixels are annual core seagrass, light blue pixels are mapped non-seagrass. The selected years are the early Sentinel-2 period, the reference-map period and the recent period.

The maps show that Anse-aux-Pins has a persistent seagrass core that is detected repeatedly over time. This supports the interpretation that the mapped meadow is not composed of temporary or seasonal detections only but a stable coastal habitat . These shallow Seychelles lagoons are known to support extensive seagrass meadows (C. B. Lee et al., 2023; Rowlands, 2024). The main inter-annual differences are at the margins of the meadow, in particular along the offshore edge and in the central/northern sector .

Margins are more sensitive to changes in water depth, turbidity, substrate reflectance, canopy density, mixed pixels and classification threshold effects (Cingano et al., 2024; Lizcano-Sandoval et al., 2025; Unsworth et al., 2019). Therefore, small single-year differences should not be over-interpreted as direct ecological gain or loss.

Overall, the comparison between 2017, 2021 and 2025 suggests a strengthening or reorganization of the meadow structure in the central to southern part of the AOI. This area was less to not at all present in 2017, became more present in 2021 and developed more in 2025. However, because these maps represent annual high-confidence core seagrass, they mainly describe persistent meadow structure and do not fully capture short-term seasonal expansion zones. This spatial overview is therefore used in the next subsection to examine long-term recovery and loss patterns.

4.3.5 Recovery and spatial change between 2016-2018 and 2024-2026

The recovery/loss analysis complements the annual maps (*Section 4.3.4*) by focusing directly on pixels that changed status between the start and the end of the time series. Instead of annual map of seagrass, it shows where high-confidence seagrass ($p \geq 0.75$) remained stable, increased, or decreased between 2016-2018 and 2024-2026 (*Fig. 36*)

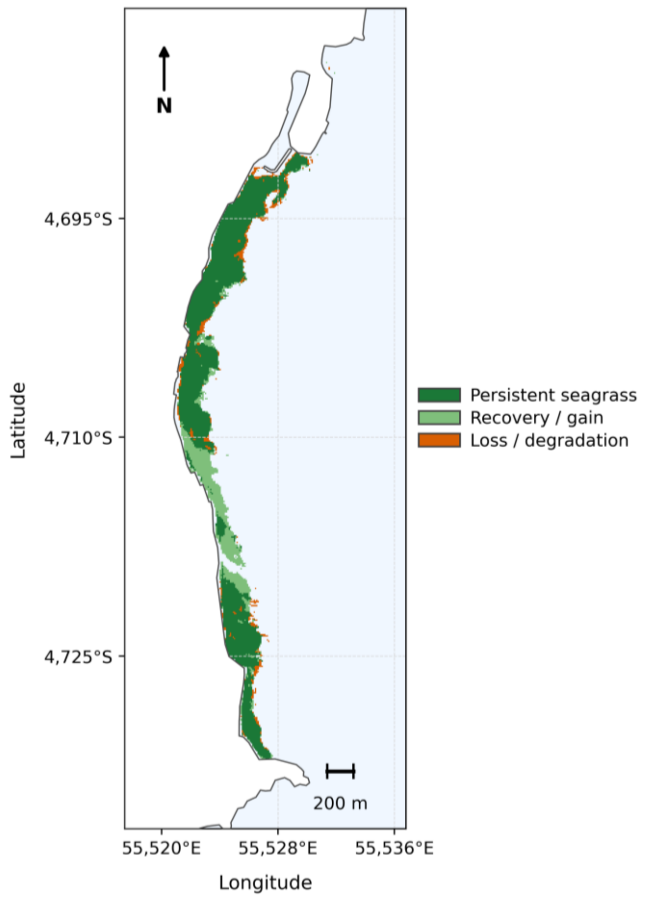

Figure 36 - Long-term seagrass recovery/loss between 2016-2018 and 2024-2026. The map shows persistent seagrass ($p \geq 0.75$), recovery/gain and loss/degradation, with the main recovery zone located in the central to southern AOI.

The clearest satellite detected change is the apparent recovery observed in the central to southern part of the AOI. In this sector, recovery forms a coherent extension connected to the persistent meadow. This pattern is more informative than the smaller isolated gain pixels because it is spatially structured and directly adjacent to the stable seagrass area. Apparent loss is also visible, especially in the northern part of the meadow, where it happens along the margin of the persistent seagrass. Although smaller than the central/southern recovery zone, this pattern remains relevant because it may indicate a less stable meadow edge. These loss margins could therefore be considered as a priority area for future monitoring or field verification. The central/southern recovery pattern could also be linked to local coastal modifications. *Dr Jérôme Harlay* (*Pers. Comm.*) suggested in discussions that coastal works in this sector may have modified local hydrodynamics, potentially disturbing the meadow first and then allowing progressive recolonization or more consistent satellite detection as conditions stabilized. However, this interpretation remains hypothetical, because no independent hydrodynamic dataset, historical engineering record, or recent field validation was available to test it directly. These spatial changes agree with the smoothed curve (*Section 4.3.2*) that suggested a weak increase in mapped seagrass extent from about 0.7 km^2 in 2016 to about 0.8-0.9 km^2 in 2026. The central/southern recovery zone may explain part of this increase, while the northern marginal loss shows that the change is not spatially uniform.

This suggests a spatial reorganization of mapped seagrass, with recovery in the central/southern margin and localized apparent loss in the northern margin. This should still be interpreted as satellite detected change, not as direct proof of ecological recovery or degradation.

4.3.6 Synthesis: temporal patterns and implications for transferability

The Anse-aux-Pins analysis is the reference framework for the transferability analysis. This primary site produced a number of coherent spatial and temporal patterns with the model that was selected: a persistent mapped seagrass core, a mapped extent chronological trajectory, a seasonal cycle, a seasonal marginal envelope and a spatially organized recovery/loss pattern. Together, these results illustrate what coherent model behavior looks like at the site where reference data is available.

For *Section 4.4*, the objective is therefore not specifically to verify whether the model predicts seagrass at the secondary sites. But also to assess if similar types of spatial and temporal structures can be observed, including persistent cores, seasonal cycles, seasonal envelopes, chronological trajectories and coherent changes through time. The transferability analysis will therefore evaluate not only whether seagrass is predicted, but also whether the predictions form ecologically plausible, spatially coherent and temporally interpretable patterns when the model is applied to other Seychelles lagoons.

4.4 Transferability to secondary Seychelles seagrass sites

The optimized pipeline was applied to the four secondary sites (*Section 3.1.2*), with site locations shown in Fig. 13. in order to evaluate if the Sentinel-2 workflow developed at Anse-aux-Pins can be extended to other Seychelles reef-lagoon systems . No field observation data were available for these sites and so this analysis should not be taken as a validation of seagrass maps for Côte d'Or, Grande Anse, Sainte Anne and Baie Sainte Anne. Instead, the goal is to evaluate the transferability of the existing classifier trained on Anse-aux-Pins. The methodology is transferable itself, as the same pre-processing, feature extraction, classification and temporal aggregation steps can be applied to all the sites. So the main question is "how well does the classifier generalize outside the training site?" and "what additional training data would be needed to scale the method more robustly over the Seychelles EEZ?".

4.4.1 Observation availability and spatial reliability

Before analyzing the transferred seagrass predictions, the spatial distribution of valid Sentinel-2 observations is checked for the four secondary sites (*Fig. 37*). This figure follows the same logic as *Section 4.3.1*, where lower valid counts are mainly observed close to the coastline and are interpreted as a possible effect of cloud-mask over removal of bright shallow sand pixels.

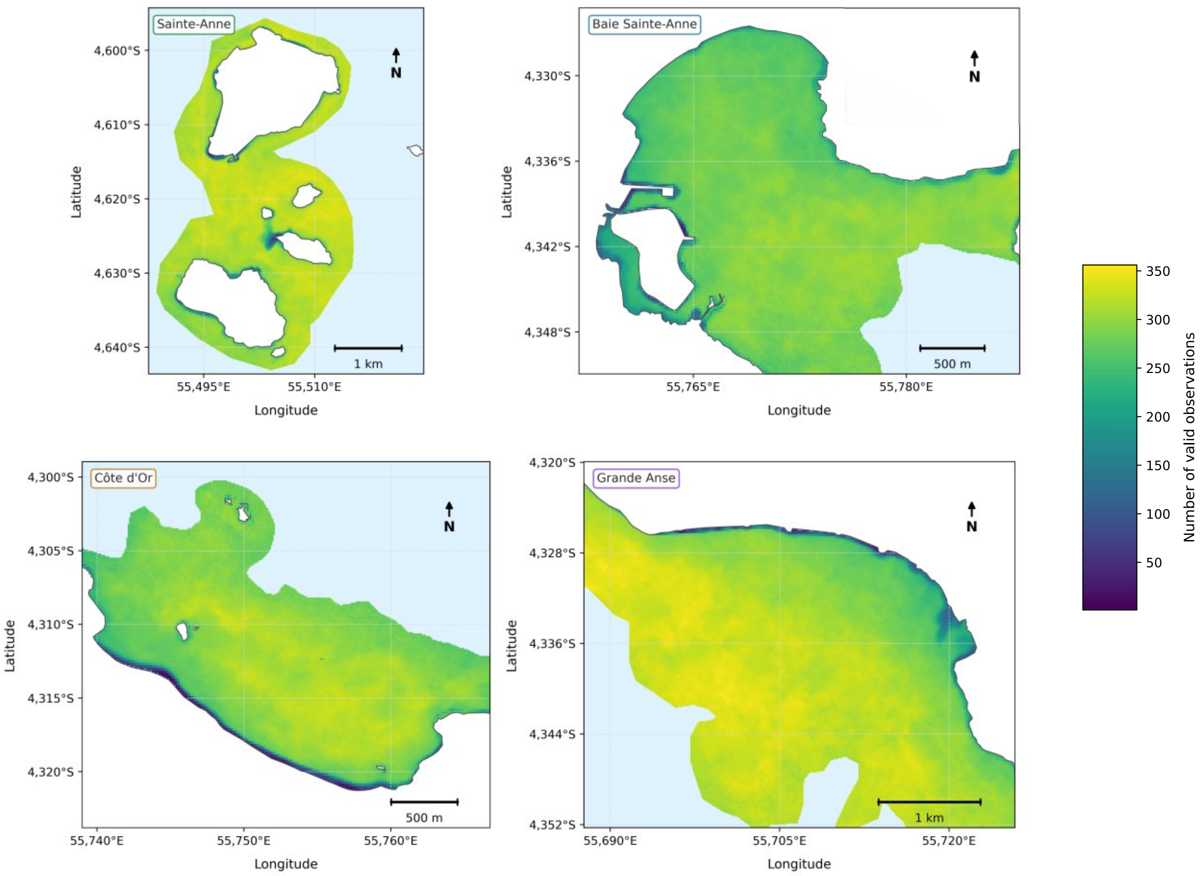

Figure 37 - Spatial distribution of valid Sentinel-2 observation counts at the four secondary sites. Pixel values indicate the number of valid observations after preprocessing and masking. Higher values indicate area where seagrass predictions and change maps are expected to be more reliable.

Most lagoon areas at the secondary sites show good valid-observation coverage. This indicates that the Sentinel-2 archive and the preprocessing workflow are sufficient to generate multi-temporal prediction products outside Anse-aux-Pins. In this sense, the observation availability supports the technical transferability of the workflow to other Seychelles reef-lagoon systems. However, lower counts are again found near coastlines, island margins and shallow lagoon edges. This pattern is visible at Sainte Anne and Baie Sainte Anne, but is especially clear at Côte d'Or and Grande Anse, where the nearshore beach zones show more irregular observation counts. These areas are the most optically difficult parts of lagoons, where bright sand, very shallow water, tide-related exposure or submersion and high bottom reflectance affect cloud masking and preprocessing.

This result does not limit the transferability of the method itself, but highlights an important condition to scale the workflow more robustly. The current pre-processing chain works well in most lagoon interiors, but very shallow and bright coastal areas need to be masked more carefully or adjusted by site-specific methods. Thus, predictions in areas with consistently observed lagoons can be interpreted with more confidence and predictions near low-count shorelines should be treated with more caution. Improving cloud and shoreline masking in bright shallow-water environments would be a key step to increase spatial reliability across heterogeneous lagoons for future application at the scale of the Seychelles EEZ.

4.4.2 Spatial coherence and site-specific generalization

After the valid-observation count analysis, the transferred predictions were compared with the MACCE reference map, the model-derived national seagrass cartography product (*Fig. 9*), and the Sentinel-2 satellite image for each secondary site (*Figs. 38-41*). As the original reference shapefile was unavailable, only screenshots of the reference maps were used for qualitative visual comparison. The objective is not to validate, but to assess if the model produce spatially coherent seagrass maps outside Anse-aux-Pins.

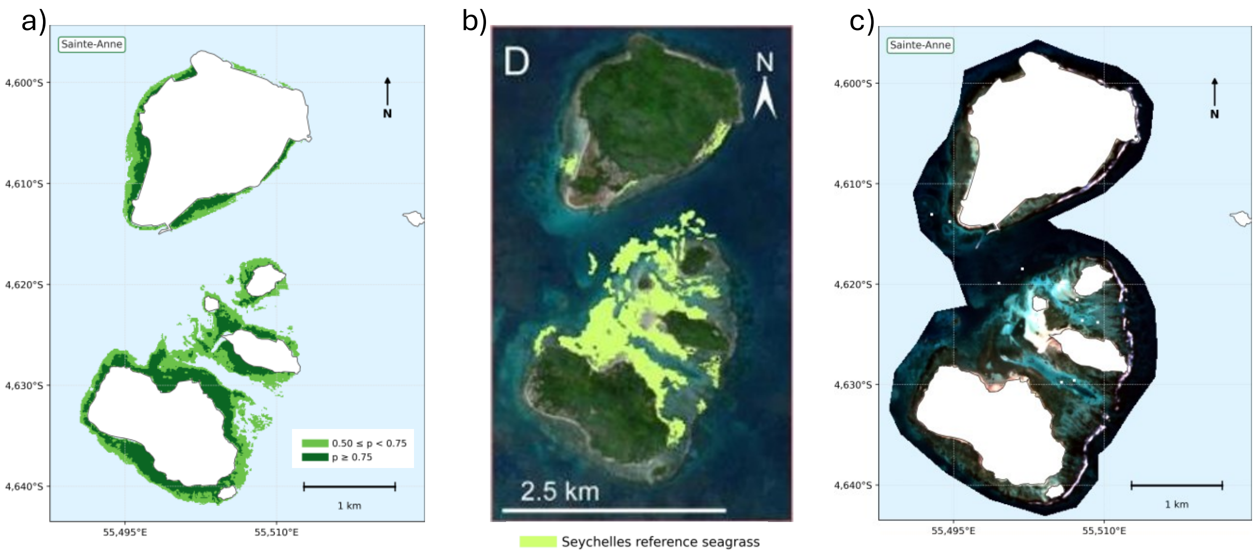

Figure 38 - Spatial transferability overview at Sainte Anne. The figure compares a) the transferred DSF + XGBoost + Macro-F1 mapped seagrass predictions with b) the MACCE reference map and c) the 2025-07-12 Sentinel-2 satellite image.

At Sainte Anne, the transferred model shows the most coherent spatial pattern (*Fig. 38*). Mapped seagrass is mainly located around and between the islands, in shallow lagoon and reef-flat areas. This is broadly consistent with the MACCE reference map and with the satellite image. Some differences remain near island margins, where the model sometimes detects mapped seagrass that is less visible in the reference map and sometimes misses areas mapped as seagrass in the reference. However, the satellite image suggests that several of these differences occur in areas, where depth and water clarity may change from Anse-aux-Pins. The general structure looks like a meadow and is spatially plausible. Sainte Anne therefore shows to be the strongest transferability case.

At Côte d'Or, the classifier shows a seagrass band parallel to the coast (*Fig. 39*). This pattern is partly coherent because it follows the shallow lagoon structure. However, the model also shows a clear shoreline problem. Mapped seagrass follows the bright beach zone almost continuously, whereas the reference map is more patchy and located slightly farther offshore. The satellite image supports the idea that this nearshore area is affected by bright sand, very shallow water and tide-related exposure or submersion. Thus, Côte d'Or is a partial transferability case. Some offshore and lagoonal detections may be plausible, but predictions close to the beach should be interpreted with caution.

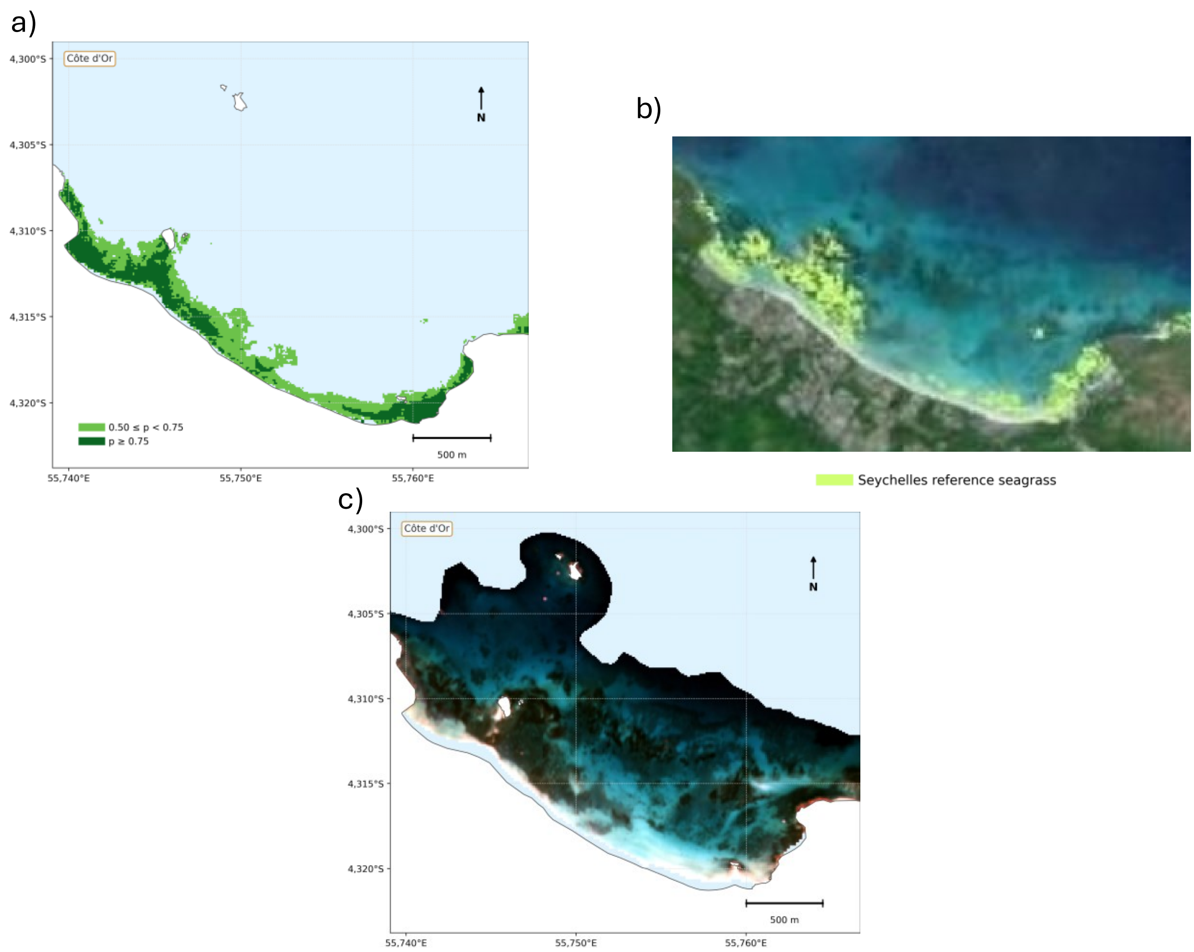

Figure 39 - Spatial transferability overview at Cote d'Or. The figure compares a) the transferred DSF + XGBoost + Macro-F1 mapped seagrass predictions with b) the MACCE reference map and c) the 2025-07-12 Sentinel-2 satellite image.

At Grande Anse, he spatial coherence of the transferred predictions is weaker (*Fig. 40*). The classifier mainly detects mapped seagrass along the coast and lagoon edges, while much of the inner-lagoon seagrass shown in the reference map is weakly detected or absent. Some detections, especially along bright shallow substrates or reef-sand mixtures, appear questionable when compared with the Sentinel-2 image. This suggests that the current classifier does not fully capture the optical or ecological state of Grande Anse. The weaker result does not indicate that the workflow cannot be applied to this site, but rather that the Anse-aux-Pins training dataset does not sufficiently represent this lagoon configuration or seagrass signal.

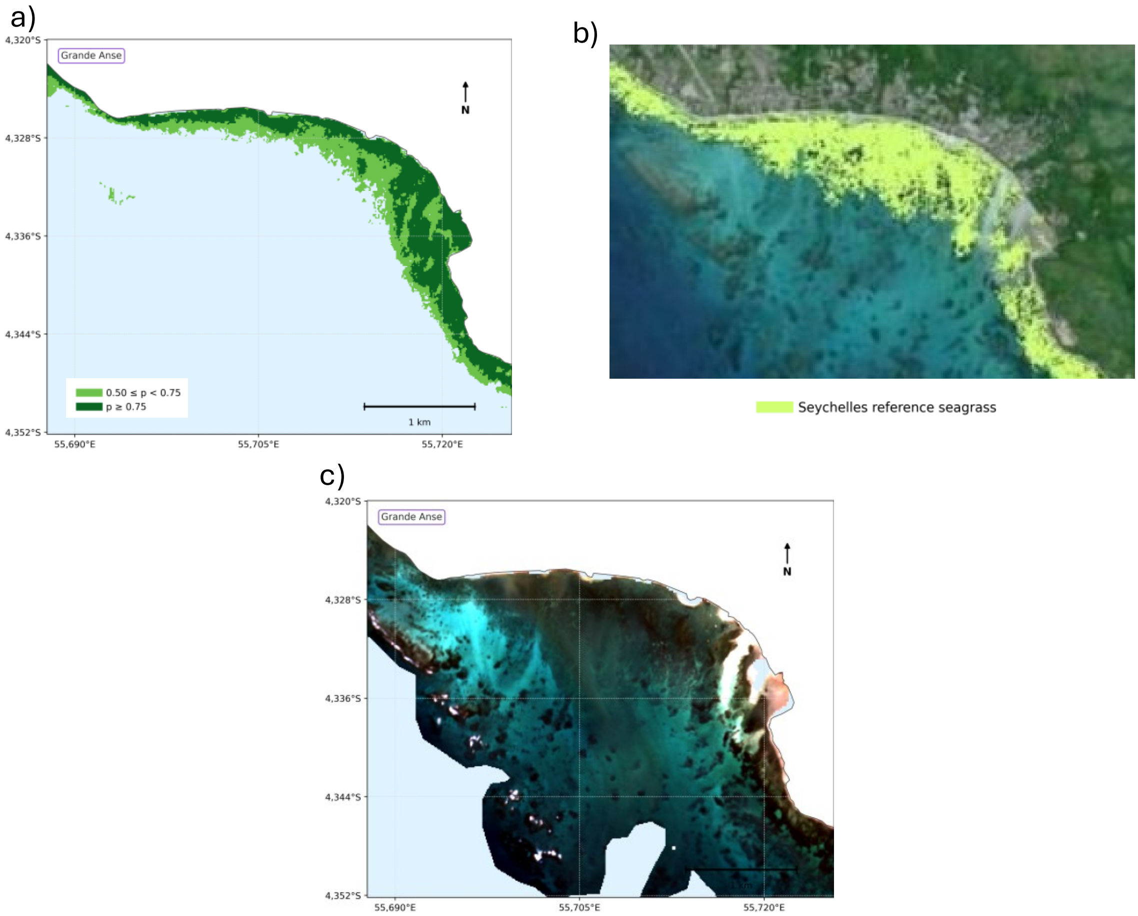

Figure 40 - Spatial transferability overview at Grande Anse. The figure compares a) the transferred DSF + XGBoost + Macro-F1 mapped seagrass predictions with b) the MACCE reference map and c) the 2025-07-12 Sentinel-2 satellite image.

The spatial result of Baie Sainte Anne is the most uncertain (Fig. 41). The transferred classifier only poorly detects the main inner-bay seagrass area visible in the reference map. Instead, detections are concentrated along the margins of the bay where optical confusion with shallow substrate, turbidity or mixed bottom types is more likely to occur. Some differences between transferred predictions and reference map, in this case, may reflect both classifier limitations and ecological differences between sites. Baie Sainte Anne should thus be read as the weakest transferability case of the four secondary sites.

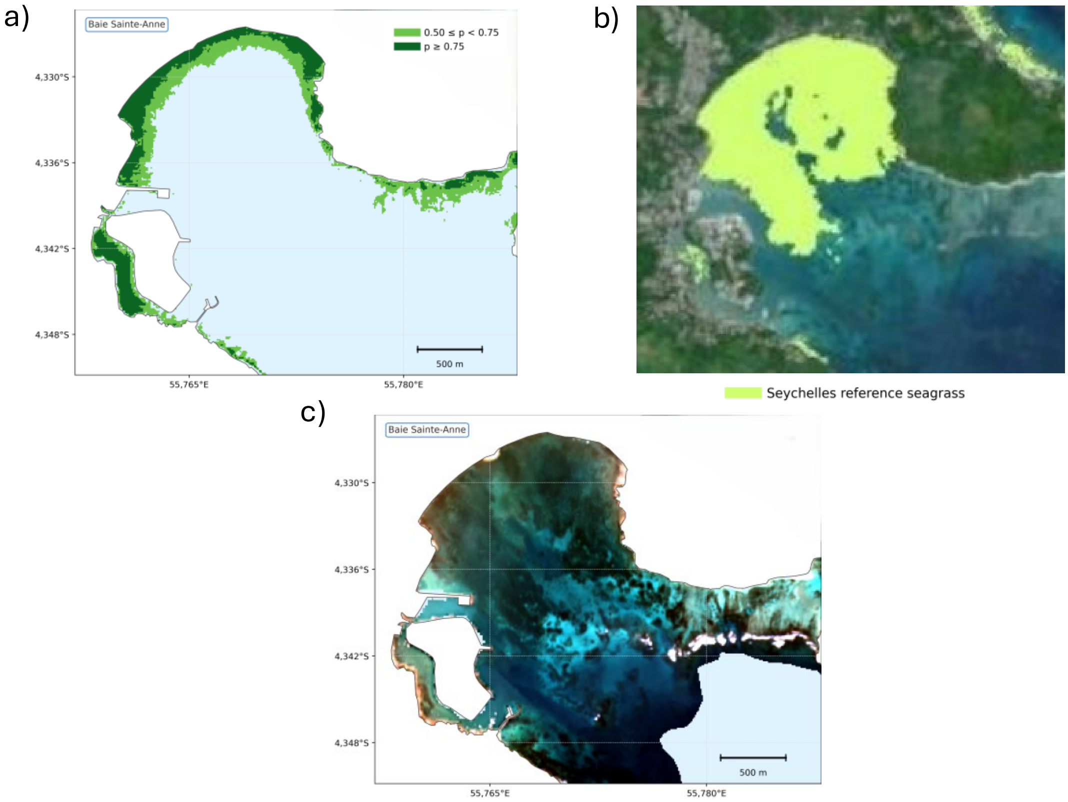

Figure 41 - Spatial transferability overview at Baie Sainte Anne. The figure compares a) the transferred DSF + XGBoost + Macro-F1 mapped seagrass predictions with b) the MACCE reference map and c) the 2025-07-12 Sentinel-2 satellite image.

Site-dependent differences can be explained by several uncertainties. First, secondary sites were not validated in-situ thus the comparison with the MACCE reference map and Sentinel-2 image is still a test of spatial coherence and not an independent quality analysis. Second, the model was trained from pixels extracted from a reference map, which may itself contain errors. If some training pixels did not correspond to true seagrass observations, the classifier may have learned part of this uncertainty and transferred it to other sites. Third, the secondary lagoons differ from Anse-aux-Pins in morphology, depth, substrate brightness, water clarity, tide influence and seagrass species composition. These factors are important because seagrass mapping is affected by the combined signal of the water column and the benthic substrate (*Section 3.4*) Future work should therefore aim to build a training dataset based on field observations, from as much lagoons, tide levels, depths, substrates and seagrass species as possible.

The four sites show a clear gradient of spatial coherence. Sainte Anne shows strong classifier generalization, Côte d'Or shows partial generalization with important shoreline confusion and Grande Anse and Baie Sainte Anne show weaker agreement with the reference map and satellite image. This gradient is a useful result for scaling the method to the Seychelles EEZ. It shows that the workflow can be applied to different reef-lagoon systems, but that robust spatial generalization requires a training dataset that includes a wider range of lagoon morphologies, depths, substrates, water-column conditions, tidal states and seagrass species.

4.4.3 Temporal and seasonal behavior of secondary sites

After the spatial comparison, the transferred time series are analyzed to evaluate if the secondary sites exhibit coherent chronological trajectories and seasonal cycles. This step must be read in conjunction with *Section 4.4.2*, as temporal curves are only meaningful if the mapped seagrass areas are spatially plausible. Thus, the objective is not to validate seagrass dynamics at the secondary sites, but to evaluate whether the Anse-aux-Pins-trained classifier produces temporally coherent outputs outside of its training site.

The chronological trajectories show strong variability at all four secondary sites (*Fig. 42*). None of the sites follows a simple monotonic long-term trend. This is similar to Anse-aux-Pins, where the mapped extent also showed repeated phases of expansion and contraction rather than a linear trajectory (*Section 4.3.2*). The similarity is clearest for the sites that showed better spatial transferability, especially Sainte Anne, where the curve shows lower values around 2019-2020, higher mapped extent between 2021 and 2025 and a decrease toward 2026. Côte d'Or and Grande Anse also show structured temporal changes, but with stronger instability or spatial uncertainty. Baie Sainte Anne shows repeated peaks and declines, although its temporal interpretation is more uncertain because of the weaker spatial agreement observed in *Section 4.4.2*.

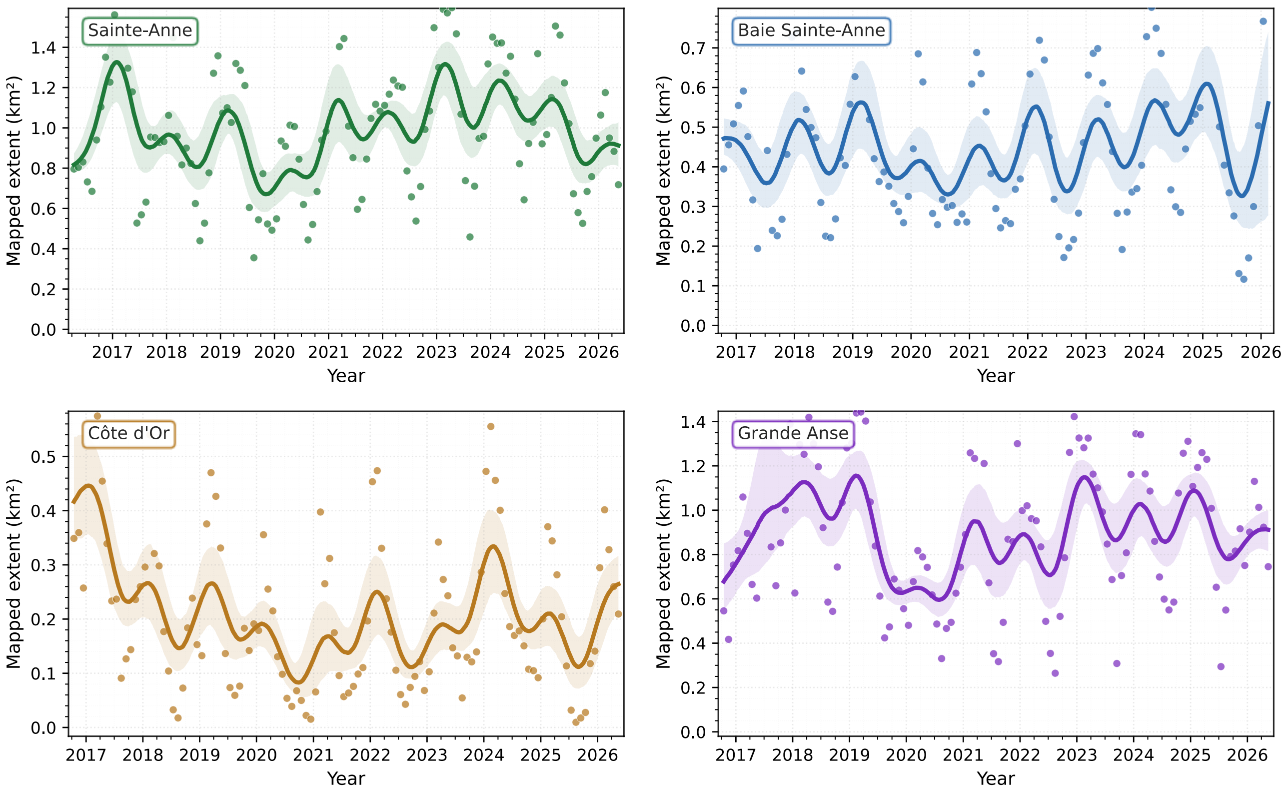

Figure 42 - Chronological trajectories of high-confidence mapped seagrass extent at the four secondary sites. Points are monthly Sentinel-2-estimates of mapped seagrass extent using the transferred model and a high-confidence threshold. The solid lines show smoothed temporal trajectories and the shaded envelopes show uncertainty from the smoothing procedure.

Such site-to-site variations should not necessarily be seen as errors. Local dynamics vary among seagrass meadows, depending on lagoon morphology, exposure, water depth, substrate type, hydrodynamics, species composition and water column conditions. Thus, a divergence of the chronological trajectories is expected even if the same regional seasonal forcing is acting on all sites. The important thing about transferability is that the curves should not all look like Anse-aux-Pins, but rather that they should have structured and interpretable behavior instead of random model noise.

Seasonal curves are more consistent between sites (*Fig. 43*). Mapped seagrass extent is generally highest between Feb-Apr and lowest around Aug-Sep before increasing again towards the end of the year. This timing is similar to the seasonal cycle observed at Anse-aux-Pins where high-confidence mapped seagrass extent peaked around February and was at a minimum around September-October (*Section 4.3.3*). The common seasonal pattern indicates that the transferred classifier is responding to a repeated seasonal signal in a number of Seychelles reef-lagoon systems.

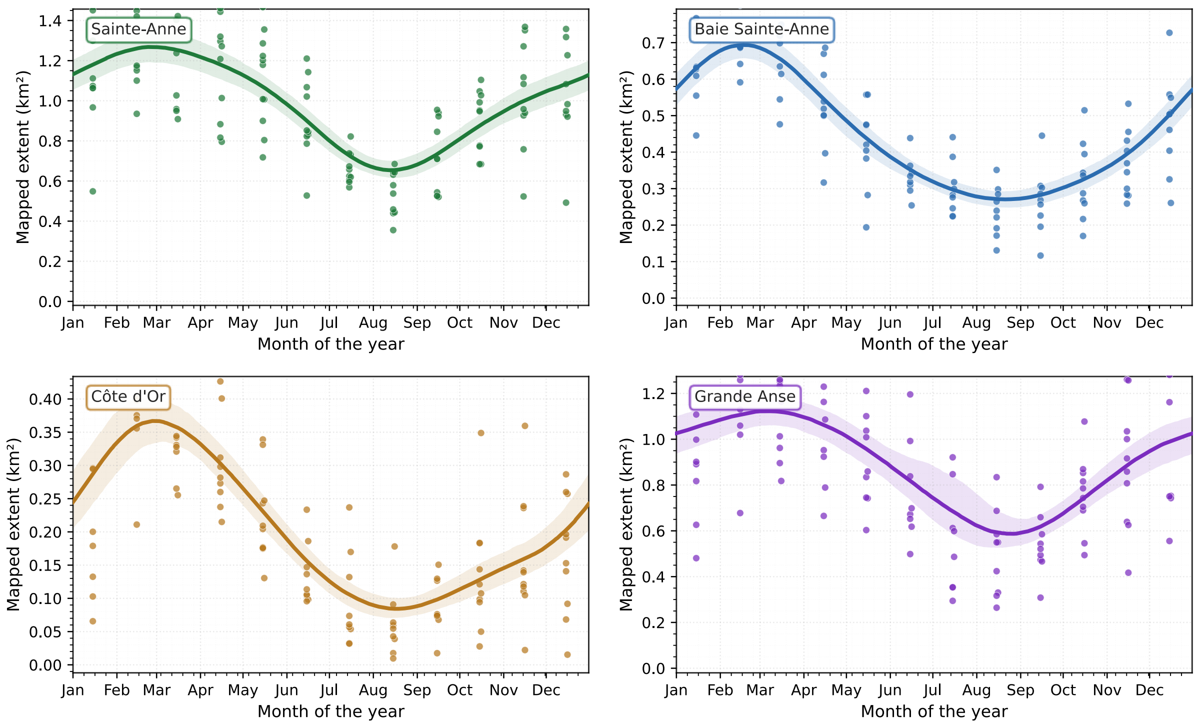

Figure 43 - Seasonal cycles of high-confidence mapped seagrass extent at the four secondary sites. Curves show the mean annual cycle of high-confidence mapped seagrass extent obtained by aggregating monthly composites across the Sentinel-2 time series.

However, similar seasonal timing does not prove identical ecological seasonality. The model may reflect real meadow dynamics, seasonal variation in optical detectability, or both. This is consistent with the basis of remote sensing detection of seagrass (*Section 3.4*). The temporal curves are thus most informative where the spatial predictions are coherent and more exploratory where a confusion of shoreline or spatial mismatch was found (*Section 4.4.2*).

Thus, the secondary sites show two important results. First, their chronological trajectories are not identical, which is expected because each meadow has its own local dynamics. Second, they share a common seasonal structure that is close to the Anse-aux-Pins pattern, especially for the more transferable sites. This is a positive result for scaling the method, as it demonstrates the workflow is capable of producing comparable temporal indicators across multiple Seychelles reef-lagoon systems. Future field observations across seasons, tide levels, depths, lagoon types and seagrass species would improve separation of true seagrass seasonality from seasonal variations in optical detectability.

4.5 General limitations and perspectives

The main uncertainties related to the Sentinel-2 workflow were identified in the previous sections, from feature interpretation and model selection to temporal analysis and transferability. Such uncertainties do not limit the relevance of the results, but rather define the conditions for the interpretation of the outputs and the improvements necessary for future operational monitoring.

The first important point is the reference data. The classifier was trained on the reference map of Anse-aux-Pins as the available data source for model development, not on a direct multi-season field dataset. Therefore the spectral analyses and performance metrics should be viewed as agreement with the available reference product rather than as direct field accuracy. This remains useful because it provides a consistent evaluation of the workflow and identifies where additional data would be most valuable. Future field data would help improve the model and better quantify its ecological accuracy. If no local observations are available, the first step could be to extend the calibration dataset with reference data from optically similar tropical reef-lagoon systems, before prioritizing targeted Seychelles observations in seasonal maxima and minima, stable cores, variable margins.

The second point is the feature set and the model structure. The full feature set was useful for comparing atmospheric correction, classifiers and thresholds under consistent conditions. However, the feature analysis and feature contribution results show that some predictors are more discriminative and temporally stable than others. Future work could thus reduce the current feature set, but also test new features that might increase robustness such as bathymetric or depth proxies, turbidity indicators or tide-related variables. The objective would be to keep variables which present a good separability of class, a temporal stability and a good transferability.

A third point concerns the ecological interpretation of mapped temporal patterns. The results are not to be interpreted as direct measurements of biomass, density, species composition or percentage cover. But this does not mean that the detected signal is meaningless. The spatial and temporal coherence of the trajectories, seasonal cycle and persistent core and recovery/loss zones suggest that they can be interpreted as indicators of mapped seagrass extent and detectability. Future work should include a more diverse calibration and validation dataset, including field observations across different seasons, meadow densities, species assemblages, water depths, tide levels and substrate types to strengthen their ecological interpretation. Such data would help to determine whether changes in mapped extent are associated with real seagrass dynamics, changes in canopy density or species composition, or seasonal changes in optical detectability.

A fourth perspective is about scaling. The transferability analysis shows that the same workflow can be applied to several Seychelles reef-lagoon systems and that some sites, especially Sainte Anne, produced coherent spatial and temporal outputs. The main requirement for more robust scaling is therefore not a different methodology but a larger and more representative training dataset. This would include field observations for various lagoon morphologies, depths, substrates, tide levels (during image acquisition) and dominant seagrass species (such as mixed meadows, *Thalassodendron*-dominated meadows and *Enhalus*-dominated meadows), which would improve classifier generalization across the Seychelles EEZ .

Therefore, future work should focus on multi-season field validation, independent reference data and a more diverse ecological calibration dataset of different meadow densities, assemblages of species, depths, tide levels and substrate types. In parallel, improved shoreline masking in bright shallow water zones and improving the feature set and enriching it with new complementary predictors could help to strengthen the workflow. Together, these improvements would support the development of an already working Sentinel-2 workflow toward long-term monitoring of Seychelles seagrass meadows.

5. Conclusion

This thesis aimed to develop a Sentinel-2-based workflow to map, monitor and analyze seagrass extent through time at Anse-aux-Pins and to identify the main requirements for broader application across Seychelles reef-lagoon systems. The work was motivated by the need to move beyond static seagrass maps and toward a reproducible time-series approach able to describe seasonal, interannual and spatial patterns of mapped seagrass extent.

The first contribution is methodological. A complete Sentinel-2 workflow was developed, from image preprocessing and atmospheric correction to feature extraction, supervised classification and temporal aggregation. The feature analysis shows that seagrass and non-seagrass pixels have coherent but overlapping optical signals, confirming that shallow-water seagrass mapping cannot rely on a single band or threshold. The most informative predictors are mainly related to the blue-green spectral contrast and local spatial context. Among the tested pipelines, the DSF + XGBoost model combined with the Macro-F1 optimized threshold provided the best compromise between performance, temporal stability, computation time and interpretability. The selected model reached a mean Macro-F1 of 0.808 ± 0.048 and a mean seagrass F1-score of 0.703 ± 0.063. These values indicate good agreement with the available reference map, while remaining dependent on the quality and representativeness of this reference product.

The second contribution is the reconstruction of the mapped seagrass extent dynamics at Anse-aux-Pins between 2016 and 2026. The Sentinel-2 archive had enough temporal coverage to analyze multi-year trends, especially between 2018 and 2025. The results show that Anse-aux-Pins is not a static meadow system. The mapped seagrass extent shows seasonal and interannual variability with repeated phases of expansion and contraction rather than a simple linear trend. We observed a weak increase in the extent of high-confidence mapped seagrass over the full period, but this trend is small compared to seasonal and interannual fluctuations.

The seasonal analysis reveals a clear annual cycle with high confidence mapped seagrass extent peaking at around February and lowest at around September-October. This seasonal signal was spatially structured, with a persistent core and a more variable marginal envelope. The persistent core can be considered as the most stable part of the mapped meadow, whereas the seasonal envelope includes areas where seagrass may be more continuous, denser or more detectable under favorable seasonal conditions.

The annual maps and recovery/loss analysis also show a coherent zone of apparent recovery or gain in the central to southern part of the lagoon, together with more localized apparent loss along some northern margins. These patterns suggest spatial reorganization of mapped seagrass extent rather than uniform change across the lagoon.

The transferability analysis shows that the same workflow can be applied to other Seychelles reef-lagoon systems. The methodology itself is therefore technically transferable, because the same preprocessing, feature extraction, classification and temporal aggregation steps were applied outside Anse-aux-Pins. However, classifier generalization was site-dependent. Sainte Anne shows the strongest spatial coherence, Côte d'Or shows partial transferability with shoreline confusion and Grande Anse and Baie Sainte Anne show weaker spatial agreement. These differences are likely related to lagoon morphology, substrate brightness, water-column conditions, tide influence and seagrass assemblages. Despite this variability, the secondary sites show a common seasonal structure, with higher mapped extent early in the year and lower mapped extent around August-September. This suggests that the workflow can produce comparable temporal indicators across several Seychelles reef-lagoon systems, although their ecological interpretation remains site-dependent.

Overall, the research question can therefore be answered positively, but with important conditions. A Sentinel-2 pipeline can be developed to map, monitor and analyze seagrass extent through time at Anse-aux-Pins. The workflow generated consistent spatial and temporal indicators including a persistent meadow core, a seasonal envelope, chronological trajectories and recovery/loss maps. It also showed promising transferability to secondary lagoon sites, particularly where site conditions were similar to those represented in the training data. However, the outputs should be viewed as mapped seagrass extent and detectability, not as direct measures of biomass, density, species composition or percentage cover.

So the main requirement for broader application across the Seychelles is not a totally different methodology, but a more solid calibration and validation basis. A multi-site and multi-season field dataset covering different lagoon morphologies, depths, substrates, tide levels, water conditions and seagrass assemblages would allow the classifier to generalize more robustly. Improving the shoreline masking in bright shallow water zones and optimizing the feature set i.e. via complementary predictors, would also strengthen the workflow. With these improvements, the approach developed in this thesis could support long-term Sentinel-2 based monitoring of Seychelles seagrass meadows and provide spatially explicit indicators for future conservation, restoration and blue-carbon monitoring.

References

Agate, J., Ballinger, R., & Ward, R. D. (2024). Satellite remote sensing can provide semi-automated monitoring to aid coastal decision-making. *Estuarine, Coastal and Shelf Science*, *298*, 108639. https://doi.org/10.1016/j.ecss.2024.108639

Amone-Mabuto, M., Bandeira, S., Hollander, J., Hume, D., Campira, J., & Adams, J. (2024). Monitoring seagrass meadows in Maputo Bay using integrated remote sensing techniques and machine learning. *Regional Studies in Marine Science*, *79*, 103816. https://doi.org/10.1016/j.rsma.2024.103816

Baker, S., Constant, N., & Nicol, P. (2023). Oceans justice: Trade-offs between Sustainable Development Goals in the Seychelles. *Marine Policy*, *147*, 105357. https://doi.org/10.1016/j.marpol.2022.105357

Belgiu, M., & Drăguţ, L. (2016). Random forest in remote sensing: A review of applications and future directions. *ISPRS Journal of Photogrammetry and Remote Sensing*, *114*, 24–31. https://doi.org/10.1016/j.isprsjprs.2016.01.011

Bennett, M., March, A., Raguain, J., & Failler, P. (2024). Blueprint for Blue Carbon: Lessons from Seychelles for Small Island States. *Oceans*, *5*(1), 81–108. https://doi.org/10.3390/oceans5010006

Breiman, L. (2001). Random Forests. *Machine Learning*, *45*(1), 5–32. https://doi.org/10.1023/A:1010933404324

Caballero, I., Fernández, R., Escalante, O. M., Mamán, L., & Navarro, G. (2020). New capabilities of Sentinel-2A/B satellites combined with in situ data for monitoring small harmful algal blooms in complex coastal waters. *Scientific Reports*, *10*(1), 8743. https://doi.org/10.1038/s41598-020-65600-1

Castagna, A., & Vanhellemont, Q. (2025). A generalized physics-based correction for adjacency effects. *Applied Optics*, *64*(10), 2719. https://doi.org/10.1364/AO.546766

Cavanaugh, K. C., Bell, T. W., Aerni, K. E., Byrnes, J. E. K., McCammon, S., & Smith, M. M. (2025). New Technologies for Monitoring Coastal Ecosystem Dynamics. *Annual Review of Marine Science*, *17*(Volume 17, 2025), 409–433. https://doi.org/10.1146/annurev-marine-040523-020221

Chen, T., & Guestrin, C. (2016). XGBoost: A Scalable Tree Boosting System. *Proceedings of the 22nd ACM SIGKDD International Conference on Knowledge Discovery and Data Mining*, 785–794. https://doi.org/10.1145/2939672.2939785

Cingano, P., Vuerich, M., Petruzzellis, F., Orzan, L., Trotta, G., Casolo, V., Asquini, E., Bacaro, G., & Boscutti, F. (2024). Seagrasses on the move: Tracing the multi-decadal species distribution trends in lagoon meadows using Landsat imagery. *Ecological Informatics*, *82*, 102685. https://doi.org/10.1016/j.ecoinf.2024.102685

Claverie, M., Ju, J., Masek, J. G., Dungan, J. L., Vermote, E. F., Roger, J.-C., Skakun, S. V., & Justice, C. (2018). The Harmonized Landsat and Sentinel-2 surface reflectance data set. *Remote Sensing of Environment*, *219*, 145–161. https://doi.org/10.1016/j.rse.2018.09.002

The Nature Conservancy. (2018). *Seychelles Protects 158,000 Square Miles of Ocean*. https://www.nature.org/en-us/about-us/where-we-work/africa/stories-in-africa/seychelles-conservation-commitment-comes-to-life/ Consulted on 14 November 2025

Davies, B. F. R., Oiry, S., Rosa, P., Zoffoli, M. L., Sousa, A. I., Thomas, O. R., Smale, D. A., Austen, M. C., Biermann, L., Attrill, M. J., Roman, A., Navarro, G., Barillé, A.-L., Harin, N., Clewley, D., Martinez-Vicente, V., Gernez, P., & Barillé, L. (2024a). A sentinel watching over inter-tidal seagrass phenology across Western Europe and North Africa. *Communications Earth & Environment*, *5*(1), 382. https://doi.org/10.1038/s43247-024-01543-z

Davies, B. F. R., Oiry, S., Rosa, P., Zoffoli, M. L., Sousa, A. I., Thomas, O. R., Smale, D. A., Austen, M. C., Biermann, L., Attrill, M. J., Roman, A., Navarro, G., Barillé, A.-L., Harin, N., Clewley, D., Martinez-Vicente, V., Gernez, P., & Barillé, L. (2024b). Intertidal seagrass extent from Sentinel-2 time-series show distinct trajectories in Western Europe. *Remote Sensing of Environment*, *312*, 114340. https://doi.org/10.1016/j.rse.2024.114340

Dekker, A., Brando, V., Anstee, J., Fyfe, S., Malthus, T., Karpouzli, E., Larkum, A., Orth, R., & Duarte, C. (2007). Remote Sensing of Seagrass Ecosystems: Use of Spaceborne and Airborne Sensors. In *Seagrasses: Biology, Ecology and Conservation* (pp. 347–359). https://doi.org/10.1007/978-1-4020-2983-7_15

Dekker, A. G., Phinn, S. R., Anstee, J., Bissett, P., Brando, V. E., Casey, B., Fearns, P., Hedley, J., Klonowski, W., Lee, Z. P., Lynch, M., Lyons, M., Mobley, C., & Roelfsema, C. (2011). Intercomparison of shallow water bathymetry, hydro-optics, and benthos mapping techniques in Australian and Caribbean coastal environments. *Limnology and Oceanography: Methods*, *9*(9), 396–425. https://doi.org/10.4319/lom.2011.9.396

Delegido, J., Verrelst, J., Alonso, L., & Moreno, J. (2011). Evaluation of Sentinel-2 Red-Edge Bands for Empirical Estimation of Green LAI and Chlorophyll Content. *Sensors*, *11*(7), 7063–7081. https://doi.org/10.3390/s110707063

Drusch, M., Del Bello, U., Carlier, S., Colin, O., Fernandez, V., Gascon, F., Hoersch, B., Isola, C., Laberinti, P., Martimort, P., Meygret, A., Spoto, F., Sy, O., Marchese, F., & Bargellini, P. (2012). Sentinel-2: ESA's Optical High-Resolution Mission for GMES Operational Services. *Remote Sensing of Environment, The Sentinel Missions - New Opportunities for Science*, *120*, 25–36. https://doi.org/10.1016/j.rse.2011.11.026

Duarte, C. M., Apostolaki, E. T., Serrano, O., Steckbauer, A., & Unsworth, R. K. F. (2025). Conserving seagrass ecosystems to meet global biodiversity and climate goals. *Nature Reviews Biodiversity*, *1*(3), 150–165. https://doi.org/10.1038/s44358-025-00028-x

Duarte, C. M., Middelburg, J. J., & Caraco, N. (2005). Major role of marine vegetation on the oceanic carbon cycle. *Biogeosciences*, *2*(1), 1–8. https://doi.org/10.5194/bg-2-1-2005

ESA (2023). *Sentinel-2 User Guide*. Accessed on 08 February 2026 https://sentinels.copernicus.eu/documents/247904/685211/Sentinel-2_User_Handbook

Fourqurean, J. W., Duarte, C. M., Kennedy, H., Marbà, N., Holmer, M., Mateo, M. A., Apostolaki, E. T., Kendrick, G. A., Krause-Jensen, D., McGlathery, K. J., & Serrano, O. (2012). Seagrass ecosystems as a globally significant carbon stock. *Nature Geoscience*, *5*(7), 505–509. https://doi.org/10.1038/ngeo1477

Friess, D. A., Rogers, K., Lovelock, C. E., Krauss, K., Hamilton, S. E., Lee, S. Y., Lucas, R., Primavera, J., Rajkaran, A., & Shi, S. (2019). The state of the world's mangrove forests: Past, present, and future. *Annual Review of Environment and Resources*, *44*, 16-16.27. https://doi.org/10.1146/annurev-environ-101718-033302

Fyfe, S. K. (2003). Spatial and temporal variation in spectral reflectance: Are seagrass species spectrally distinct? *Limnology and Oceanography*, *48*(1part2), 464–479. https://doi.org/10.4319/lo.2003.48.1_part_2.0464

Gillies, S. (2013). *Rasterio: Geospatial raster I/O for Python.* [Python]. rasterio. https://github.com/rasterio/rasterio (Original work published 2013)

Global Environmental Remote Sensing Laboratory. (2025). *GERSL/Fmask* [Python]. https://github.com/GERSL/Fmask (Original work published 2025)

Government of Seychelles. (2019). *Seychelles-coastal-management-plan*. https://www.gfdrr.org/sites/default/files/publication/seychelles-coastal-management-plan.pdf

Green, E., Edwards, A., & Clark, C. (2000). *Remote Sensing Handbook for Tropical Coastal Management*. http://digitallibrary.un.org/record/429234

GRID-Arendal. (2020). *Out of the Blue: The Value of Seagrasses to the Environment and to People | GRID-Arendal*. https://www.grida.no/publications/479

Guild, R., Wang, X. (Xander), & Quijón, P. (2025). Climate change impacts on coastal ecosystems. *Environmental Research: Climate*, *3*. https://doi.org/10.1088/2752-5295/ad9f90

Harris, C. R., Millman, K. J., van der Walt, S. J., Gommers, R., Virtanen, P., Cournapeau, D., Wieser, E., Taylor, J., Berg, S., Smith, N. J., Kern, R., Picus, M., Hoyer, S., van Kerkwijk, M. H., Brett, M., Haldane, A., del Río, J. F., Wiebe, M., Peterson, P., … Oliphant, T. E. (2020). Array programming with NumPy. *Nature*, *585*(7825), 357–362. https://doi.org/10.1038/s41586-020-2649-2

Hedley, J. D., Harborne, A. R., & Mumby, P. J. (2005). Technical note: Simple and robust removal of sun glint for mapping shallow-water benthos. *International Journal of Remote Sensing*, *26*(10), 2107–2112. https://doi.org/10.1080/01431160500034086

Hedley, J. D., Roelfsema, C., Brando, V., Giardino, C., Kutser, T., Phinn, S., Mumby, P. J., Barrilero, O., Laporte, J., & Koetz, B. (2018). Coral reef applications of Sentinel-2: Coverage, characteristics, bathymetry and benthic mapping with comparison to Landsat 8. *Remote Sensing of Environment*, *216*, 598–614. https://doi.org/10.1016/j.rse.2018.07.014

Hill, V. J., Zimmerman, R. C., Byron, D. A., & Heck, K. L. (2024). Mapping Seagrass Distribution and Abundance: Comparing Areal Cover and Biomass Estimates Between Space-Based and Airborne Imagery. *Remote Sensing*, *16*(23), 4351. https://doi.org/10.3390/rs16234351

Hughes, T. P., Anderson, K. D., Connolly, S. R., Heron, S. F., Kerry, J. T., Lough, J. M., Baird, A. H., Baum, J. K., Berumen, M. L., Bridge, T. C., Claar, D. C., Eakin, C. M., Gilmour, J. P., Graham, N. A. J., Harrison, H., Hobbs, J.-P. A., Hoey, A. S., Hoogenboom, M., Lowe, R. J., … Wilson, S. K. (2018). Spatial and temporal patterns of mass bleaching of corals in the Anthropocene. *Science (New York, N.Y.)*, *359*(6371), 80–83. https://doi.org/10.1126/science.aan8048

Hughes, T. P., Kerry, J. T., Álvarez-Noriega, M., Álvarez-Romero, J. G., Anderson, K. D., Baird, A. H., Babcock, R. C., Beger, M., Bellwood, D. R., Berkelmans, R., Bridge, T. C., Butler, I. R., Byrne, M., Cantin, N. E., Comeau, S., Connolly, S. R., Cumming, G. S., Dalton, S. J., Diaz-Pulido, G., … Wilson, S. K. (2017). Global warming and recurrent mass bleaching of corals. *Nature*, *543*(7645), 373–377. https://doi.org/10.1038/nature21707

ICRI/CORDIO (2024). Western Indian Ocean – Regional Coral Bleaching Report 2024. https://icriforum.org/wp-content/uploads/2024/07/WIO-bleaching-2024_summary-report.pdf

Ingram, J. C., & al. (2001). The impacts of a river effluent on the coastal seagrass habitats of Mahé, Seychelles. *South African Journal of Botany*, *67*(3), 483–487. https://doi.org/10.1016/S0254-6299(15)31167-4

IPBES. (2019). *Global assessment report on biodiversity and ecosystem services of the Intergovernmental Science-Policy Platform on Biodiversity and Ecosystem Services*. Zenodo. https://doi.org/10.5281/zenodo.6417333

Ju, J., Neigh, C., Claverie, M., Skakun, S., Roger, J.-C., Vermote, E., & Dungan, J. (n.d.). *Harmonized Landsat Sentinel-2 (HLS) Product User Guide*. https://lpdaac.usgs.gov/documents/1698/HLS_User_Guide_V2.pdf

Klemas, V. (2011). Remote Sensing Techniques for Studying Coastal Ecosystems: An Overview. *Journal of Coastal Research*, *27*(1), 2–17. https://doi.org/10.2112/JCOASTRES-D-10-00103.1

Lee, C. B., Martin, L., Traganos, D., Antat, S., Baez, S. K., Cupidon, A., Faure, A., Harlay, J., Morgan, M., Mortimer, J. A., Reinartz, P., & Rowlands, G. (2023). Mapping the National Seagrass Extent in Seychelles Using PlanetScope NICFI Data. *Remote Sensing*, *15*(18), 4500. https://doi.org/10.3390/rs15184500

Lee, Z., Carder, K. L., Mobley, C. D., Steward, R. G., & Patch, J. S. (1998). Hyperspectral remote sensing for shallow waters. I. A semianalytical model. *Applied Optics*, *37*(27), 6329–6338. https://doi.org/10.1364/AO.37.006329

Li, R.-R., Kaufman, Y. J., Gao, B.-C., & Davis, C. O. (2003). Remote sensing of suspended sediments and shallow coastal waters. *IEEE Transactions on Geoscience and Remote Sensing*, *41*(3), 559–566. https://doi.org/10.1109/TGRS.2003.810227

Li, Y., Bai, J., Chen, S., Chen, B., & Zhang, L. (2023). Mapping seagrasses on the basis of Sentinel-2 images under tidal change. *Marine Environmental Research*, *185*, 105880. https://doi.org/10.1016/j.marenvres.2023.105880

Liang, H., Wang, L., Wang, S., Sun, D., Li, J., Xu, Y., & Zhang, H. (2023). Remote sensing detection of seagrass distribution in a marine lagoon (Swan Lake), China. *Optics Express*, *31*(17), 27677–27695. https://doi.org/10.1364/OE.498901

Lizcano-Sandoval, L., Beck, M. W., Scolaro, S., Sherwood, E. T., & Muller-Karger, F. (2025). Cloud-based satellite remote sensing for enhancing seagrass monitoring and ecosystem management. *ISPRS Journal of Photogrammetry and Remote Sensing*, *227*, 508–518. https://doi.org/10.1016/j.isprsjprs.2025.06.034

LYZENGA, D. R. (1981). Remote sensing of bottom reflectance and water attenuation parameters in shallow water using aircraft and Landsat data. *International Journal of Remote Sensing*, *2*(1), 71–82. https://doi.org/10.1080/01431168108948342

Macreadie, P. I., Costa, M. D. P., Atwood, T. B., Friess, D. A., Kelleway, J. J., Kennedy, H., Lovelock, C. E., Serrano, O., & Duarte, C. M. (2021). Blue carbon as a natural climate solution. *Nature Reviews Earth & Environment*, *2*(12), 826–839. https://doi.org/10.1038/s43017-021-00224-1

March, A., Evans, T., Laing, S., & Raguain, J. (2024). Evaluating the World's First Sovereign Blue Bond: Lessons for Operationalising Blue Finance. *Commodities*, *3*(2), 151–167. https://doi.org/10.3390/commodities3020010

Mastrantonis, S., Radford, B., Langlois, T., Spencer, C., de Lestang, S., & Hickey, S. (2024). A novel method for robust marine habitat mapping using a kernelised aquatic vegetation index. *ISPRS Journal of Photogrammetry and Remote Sensing*, *209*, 472–480. https://doi.org/10.1016/j.isprsjprs.2024.02.015

Maxwell, A. E., Warner, T. A., & Fang, F. (2018). Implementation of machine-learning classification in remote sensing: An applied review. *International Journal of Remote Sensing*, *39*(9), 2784–2817. https://doi.org/10.1080/01431161.2018.1433343

McKenzie, L. J., Langlois, L. A., & Roelfsema, C. M. (2022). Improving Approaches to Mapping Seagrass within the Great Barrier Reef: From Field to Spaceborne Earth Observation. *Remote Sensing*,*14*(11), 2604. https://doi.org/10.3390/rs14112604

McKinney, W. (2010). Data Structures for Statistical Computing in Python. *SciPy 2010*. https://doi.org/10.25080/Majora-92bf1922-00a

Meyer, H., Reudenbach, C., Wöllauer, S., & Nauss, T. (2019). Importance of spatial predictor variable selection in machine learning applications – Moving from data reproduction to spatial prediction. *Ecological Modelling*, *411*, 108815. https://doi.org/10.1016/j.ecolmodel.2019.108815

MSPglobal. (2021). *MSPglobal: International guide on marine/maritime spatial planning (volume 1)—UNESCO Bibliothèque Numérique*. https://unesdoc.unesco.org/ark:/48223/pf0000379196

Mumby, P. J., Skirving, W., Strong, A. E., Hardy, J. T., LeDrew, E. F., Hochberg, E. J., Stumpf, R. P., & David, L. T. (2004). Remote sensing of coral reefs and their physical environment. *Marine Pollution Bulletin*, *48*(3–4), 219–228. https://doi.org/10.1016/j.marpolbul.2003.10.031

NASA/JPL. (2026). *Indian Ocean Dipole (IOD) Index | Vital Signs*. Ocean Surface Topography from Space. https://sealevel.jpl.nasa.gov/data/vital-signs/indian-ocean-dipole Consulted on 28 April 2026

NOAA CPC. (2026a). *Climate Prediction Center: ENSO Diagnostic Discussion*. https://www.cpc.ncep.noaa.gov/products/analysis_monitoring/enso_advisory/ensodisc.shtml Consulted on 28 April 2026

NOAA CPC. (2026b). *NOAA's Climate Prediction Center*. https://www.cpc.ncep.noaa.gov/products/analysis_monitoring/ensostuff/ONI_v5.php Consulted on 30 April 2026

Nordlund, L. M., Jackson, E. L., Nakaoka, M., Samper-Villarreal, J., Beca-Carretero, P., & Creed, J. C. (2018). Seagrass ecosystem services – What's next? *Marine Pollution Bulletin, Securing a Future for Seagrass*, *134*, 145–151. https://doi.org/10.1016/j.marpolbul.2017.09.014

Orth, R. J., Carruthers, T. J. B., Dennison, W. C., Duarte, C. M., Fourqurean, J. W., Heck, K. L., Hughes, A. R., Kendrick, G. A., Kenworthy, W. J., Olyarnik, S., Short, F. T., Waycott, M., & Williams, S. L. (2006). A Global Crisis for Seagrass Ecosystems. *BioScience*, *56*(12), 987–996. https://doi.org/10.1641/0006-3568(2006)56%5B987:AGCFSE%5D2.0.CO;2

Pahlevan, N., Sarkar, S., Franz, B. A., Balasubramanian, S. V., & He, J. (2017). Sentinel-2 MultiSpectral Instrument (MSI) data processing for aquatic science applications: Demonstrations and validations. *Remote Sensing of Environment*, *201*, 47–56. https://doi.org/10.1016/j.rse.2017.08.033

Pahlevan, N., Smith, B., Alikas, K., Anstee, J., Barbosa, C., Binding, C., Bresciani, M., Cremella, B., Giardino, C., Gurlin, D., Fernandez, V., Jamet, C., Kangro, K., Lehmann, M. K., Loisel, H., Matsushita, B., Hà, N., Olmanson, L., Potvin, G., … Ruiz-Verdù, A. (2022). Simultaneous retrieval of selected optical water quality indicators from Landsat-8, Sentinel-2, and Sentinel-3. *Remote Sensing of Environment*, *270*, 112860. https://doi.org/10.1016/j.rse.2021.112860

Palacios, D. M. M., & al. (2021). *Literature Review: Blue Carbon Research in the Tropical Western Indian Ocean (WIO).* Report submitted to SeyCCAT. https://www.bluecarbonlab.org/wp-content/uploads/2025/07/BlueCarbonLab_LitReport_Seychelles_20210301_final.pdf

Pedregosa, F., Varoquaux, G., Org, N., Gramfort, A., Michel, V., Fr, L., Thirion, B., Grisel, O., Blondel, M., Prettenhofer, P., Weiss, R., Dubourg, V., … Cournapeau, D. (2011). Scikit-learn: Machine Learning in Python. *MACHINE LEARNING IN PYTHON*. https://www.jmlr.org/papers/volume12/pedregosa11a/pedregosa11a.pdf

Qiu, S., Zhu, Z., & He, B. (2019). Fmask 4.0: Improved cloud and cloud shadow detection in Landsats 4–8 and Sentinel-2 imagery. *Remote Sensing of Environment*, *231*, 111205. https://doi.org/10.1016/j.rse.2019.05.024

Republic of Seychelles. (2020a). *Protected Planet | Anse Aux Pins Shell Reserve*. Protected Planet. https://www.protectedplanet.net/555643554

Republic of Seychelles. (2020b). *Seychelles Designates 30% of its EEZ as Marine Protected Area*. https://statehouse.gov.sc/news/4787/seychelles-designates-30-of-its-eez-as-marine-protected-area Consulted on 17 October 2025

Roberts, D. R., Bahn, V., Ciuti, S., Boyce, M. S., Elith, J., Guillera-Arroita, G., Hauenstein, S., Lahoz-Monfort, J. J., Schröder, B., Thuiller, W., Warton, D. I., Wintle, B. A., Hartig, F., & Dormann, C. F. (2017). Cross-validation strategies for data with temporal, spatial, hierarchical, or phylogenetic structure. *Ecography*, *40*, 913–929. https://doi.org/10.1111/ecog.02881

Roca-Mora, M., Peixoto-Dias, C. E., Vivanco-Bercovich, M., Lee, C. B., Fonseca, A. L., Caballero, I., Navarro, G., & Horta, P. (2026). Blending PlanetScope and Sentinel-2 imagery to assess subtidal seagrass changes in turbid waters. *Marine Pollution Bulletin*, *225*, 119228. https://doi.org/10.1016/j.marpolbul.2026.119228

Roelfsema, C. M., Lyons, M., Kovacs, E. M., Maxwell, P., Saunders, M. I., Samper-Villarreal, J., & Phinn, S. R. (2014). Multi-temporal mapping of seagrass cover, species and biomass: A semi-automated object based image analysis approach. *Remote Sensing of Environment*, *150*,172–187. https://doi.org/10.1016/j.rse.2014.05.001

Rowlands, G. (2024). *Seychelles Seagrass MACCE report*. https://seyccat.org/wp-content/uploads/2025/03/Seychelles_Seagrass_MACCE_report-1.pdf

Sebastian, T., Sreenath, K. R., Sreeram, M. P., & Ranith, R. (2023). Dwindling seagrasses: A multi-temporal analysis on Google Earth Engine. *Ecological Informatics*, *74*, 101964. https://doi.org/10.1016/j.ecoinf.2022.101964

SeyCCAT. (2024). *Final report: identify and test revenue generating possibilities of seagrass_consultants*. https://seyccat.org/wp-content/uploads/2025/03/Identify-and-test-revenue-generating-possibilities-of-seagrass_June2024.pdf

Seychelles MSP. (2020). Milestone 3—Gazetted Areas. *Seychelles Marine Spatial Plan Initiative*. https://seymsp.com/outputs/phase-3/milestone-3-gazetted-areas/

SeyVillas. (2025). *Beach "Anse aux Pins" Mahé (Seychelles)*. Seyvillas.Com. https://www.seyvillas.com/en/guide/beaches/mahe/21/anse-aux-pins Consulted on 10 October 2025

Short, F. T., & Neckles, H. A. (1999). The effects of global climate change on seagrasses. *Aquatic Botany*, *63*(3–4), 169–196. https://doi.org/10.1016/S0304-3770(98)00117-X

Thorhaug, A., Richardson, A., & Berlyn, G. (2007). Spectral reflectance of the seagrasses: Thalassia testudinum , Halodule wrightii , Syringodium filiforme and five marine algae. *International Journal of Remote Sensing*, *28*, 1487–1501. https://doi.org/10.1080/01431160600954662

Traganos, D., & Reinartz, P. (2018). Interannual Change Detection of Mediterranean Seagrasses Using RapidEye Image Time Series. *Frontiers in Plant Science*, *9*. https://doi.org/10.3389/fpls.2018.00096

UNEP, U. N. (2020, November 12). *Out of the Blue: The Value of Seagrasses to the Environment and to People | UNEP - UN Environment Programme*. https://www.unep.org/resources/report/out-blue-value-seagrasses-environment-and-people

Unsworth, R. K. F., McKenzie, L. J., Collier, C. J., Cullen-Unsworth, L. C., Duarte, C. M., Eklöf, J. S., Jarvis, J. C., Jones, B. L., & Nordlund, L. M. (2019). Global challenges for seagrass conservation. *Ambio*, *48*(8), 801–815. https://doi.org/10.1007/s13280-018-1115-y

Vanhellemont, Q. (2025). *ACOLITE User Manual 2025*. https://github.com/acolite/acolite/releases

Vanhellemont, Q. (2019). Adaptation of the dark spectrum fitting atmospheric correction for aquatic applications of the Landsat and Sentinel-2 archives. *Remote Sensing of Environment*, *225*, 175–192. https://doi.org/10.1016/j.rse.2019.03.010

Vanhellemont, Q., & Ruddick, K. (2018). Atmospheric correction of metre-scale optical satellite data for inland and coastal water applications. *Remote Sensing of Environment*, *216*, 586–597. https://doi.org/10.1016/j.rse.2018.07.015

Wartman, M., Palacios, M. M., Nourice, B., Macreadie, P. I., Constance, A., Waryszak, P., & Duarte de Paula Costa, M. (2025). Assessing blue carbon in mangrove ecosystems of Seychelles. *Journal of Environmental Management*, *374*, 123967. https://doi.org/10.1016/j.jenvman.2024.123967

Waycott, M., Duarte, C. M., Carruthers, T. J. B., Orth, R. J., Dennison, W. C., Olyarnik, S., Calladine, A., Fourqurean, J. W., Heck, K. L., Hughes, A. R., Kendrick, G. A., Kenworthy, W. J., Short, F. T., & Williams, S. L. (2009). Accelerating loss of seagrasses across the globe threatens coastal ecosystems. *Proceedings of the National Academy of Sciences of the United States of America*, *106*(30), 12377–12381. https://doi.org/10.1073/pnas.0905620106

Widya, L. K., Kim, C.-H., Do, J.-D., Park, S.-J., Kim, B.-C., & Lee, C.-W. (2023). Comparison of Satellite Imagery for Identifying Seagrass Distribution Using a Machine Learning Algorithm on the Eastern Coast of South Korea. *Journal of Marine Science and Engineering*, *11*(4), 701. https://doi.org/10.3390/jmse11040701

WMO. (2026, April 22). *WMO: Likelihood increases of El Niño*. World Meteorological Organization. https://wmo.int/media/news/wmo-likelihood-increases-of-el-nino

World Bank. (2018). *Seychelles launches World's First Sovereign Blue Bond*. World Bank. https://doi.org/10/29/seychelles-launches-worlds-first-sovereign-blue-bond

Xu, H. (2006). Modification of normalised difference water index (NDWI) to enhance open water features in remotely sensed imagery. *International Journal of Remote Sensing*, *27*(14), 3025–3033. https://doi.org/10.1080/01431160600589179

Zabarte-Maeztu, I., Matheson, F. E., Manley-Harris, M., Davies-Colley, R. J., & Hawes, I. (2021a). Fine sediment effects on seagrasses: A global review, quantitative synthesis and multi-stressor model. *Marine Environmental Research*, *171*, 105480. https://doi.org/10.1016/j.marenvres.2021.105480

Zhu, Z., Wang, S., & Woodcock, C. E. (2015). Improvement and expansion of the Fmask algorithm: Cloud, cloud shadow, and snow detection for Landsats 4–7, 8, and Sentinel 2 images. *Remote Sensing of Environment*, *159*, 269–277. https://doi.org/10.1016/j.rse.2014.12.014

Zhu, Z., & Woodcock, C. E. (2012). Object-based cloud and cloud shadow detection in Landsat imagery. *Remote Sensing of Environment*, *118*, 83–94. https://doi.org/10.1016/j.rse.2011.10.028

Zoffoli, M. L., Gernez, P., Rosa, P., Le Bris, A., Brando, V. E., Barillé, A.-L., Harin, N., Peters, S., Poser, K., Spaias, L., Peralta, G., & Barillé, L. (2020). Sentinel-2 remote sensing of Zostera noltei-dominated intertidal seagrass meadows. *Remote Sensing of Environment*, *251*, 112020. https://doi.org/10.1016/j.rse.2020.112020

Appendix

A. Software environment and Python libraries

Table 10 - Main software environment and Python libraries used

Software/Library	Version
Python	3.11.10
Numpy	1.26.4
pandas	2.2.3
geopandas	1.0.1
rasterio	1.4.3
shapely	2.0.6
scikit-learn	1.6.0

Software/Library	Version
xgboost	3.2.0
joblib	1.4.2
scipy	1.14.1
matplotlib	3.8.4
imageio	2.35.1
requests	2.32.3
aiohttp	3.11.10

B. Bounding boxes of the regions of interest

Table 11 - Bounding boxes of the study areas. Values are given as South, West, North, East in decimal degrees.

Site	Island	Bounding box (WGS84)
Anse-aux-Pins	Mahé	-4.733159, 55.511453, -4.681898, 55.541433
Côte d’Or	Praslin	-4.324406, 55.738376, -4.298374, 55.767424
Grande Anse	Praslin	-4.352977, 55.686788, -4.319168, 55.726630
Sainte Anne	Mahé	-4.648416, 55.483850, -4.589368, 55.528414
Baie Sainte Anne	Praslin	-4.351474, 55.756263, -4.324649, 55.788724

C. Fmask parameterization for Sentinel-2

Table 12 - Fmask parameterization for Sentinel-2

Parameter	Sentinel-2	Description
Minimum cloud size (pixels)	20	Minimum size of detected cloud objects
Cloud buffer distance (m)	20	Buffer applied around detected clouds
Shadow buffer distance (m)	40	Buffer applied around detected cloud shadows
Cloud probability threshold (%)	45	Threshold used to classify pixels as clouds
Mask clouds	Yes	Cloud pixels removed from analysis
Mask cloud shadows	No	Shadow pixels removed from analysis
Mask snow	No	Snow pixels removed (not relevant in study area)
Mask water	No	Water class retained for further processing

D. Hyperparameters used during nested cross-validation

In this appendix is presented the hyperparameter grids used in the inner CV loop for RF and XGBoost. The grids were evaluated independently in each outer fold and the best hyperparameter set was selected exclusively based on the training data of a fold.

Table 13 - RF hyperparameter grid tested during the inner CV loop. The grid had 96 combinations and was evaluated independently within each outer fold.

Parameter	Tested values	Meaning
n_estimators	500, 800	Number of trees in the forest. More trees is better for model stability in general, but longer computation time.
max_features	"sqrt", 0.5	Number of features to consider for each split "sqrt" is more conservative, 0.5 allows half of all input features to be considered.
max_depth	10, 20	Maximum depth for each tree. This controls model complexity and helps to reduce overfitting.
min_samples_leaf	1, 5, 10	Minimum number of samples required in a terminal leaf. Larger values produce smoother trees and reduce overfitting.
class_weight	"balanced", "balanced_subsample", {0: 1, 1: 2}, None	Weighting strategy used to account for possible imbalance between the non-seagrass and seagrass classes during training.

Table 14 - XGBoost hyperparameter grid tested during the inner CV loop. The grid had 384 combinations and was evaluated independently within each outer fold.

Parameter	Tested values	Meaning
n_estimators	300, 600	Number of boosting rounds, i.e. number of trees that are added in a sequence.
max_depth	4, 6, 8	Max depth of each tree. Higher values allow for more complex interactions, but also carry a higher risk of overfitting.
learning_rate	0.05, 0.1	Step size used in each boosting update. Smaller values tend to result in more gradual, stable learning.
subsample	0.8, 1.0	The fraction of training samples to build each tree. Values below 1.0 add randomness and can reduce overfitting.
colsample_bytree	0.8, 1.0	Fraction of input features used to build each tree. This may reduce the correlation between trees and improve generalization.
min_child_weight	1, 5	Minimum sum of instance weights required in a child node. Higher values make the model more conservative.
gamma	0, 1	Minimum loss reduction required to make an additional split. Higher values make tree growth more restrictive.
scale_pos_weight	1.0	Weight applied to the positive class. It was kept fixed because class imbalance was already handled during sampling.

E. Complete atmospheric-correction difference statistics

Table 15 - Median feature-distribution differences between RAdCor and DSF for all Sentinel-2 native bands and derived features. Values correspond to the median difference RAdCor − DSF, computed separately for non-seagrass and seagrass pixels. Positive values indicate higher feature values after RAdCor correction, while negative values indicate lower values.

Feature	Median Δ non-seagrass	Median Δ seagrass	Median Δ (%) non-seagrass	Median Δ (%) seagrass
B01	-0.000375	-0.001251	-1.67	-6.05
B02	-0.000052	-0.000560	-0.25	-2.46
B03	0.000064	-0.000024	0.27	-0.09
B04	-0.000010	-0.000034	-0.10	-0.18
B05	-0.000239	-0.000291	-2.14	-1.31
B08	-0.001134	-0.001765	-59.37	-39.83
B11	-0.000031	-0.000220	-52.73	-62.80
DIFF_B03_B02	0.000266	0.000522	4.27	4.99
DIFF_B04_B03	-0.000055	0.000048	-0.42	0.41
DIFF_B05_B03	-0.000254	-0.000163	-1.91	-1.65
DII_B01_B03	0.118088	0.082795	5.38	3.57
DII_B02_B03	0.130286	0.103027	25.17	14.36
DII_B03_B04	0.020924	0.008309	1.96	0.70
IDX_B03_B02	0.003409	0.011853	3.16	6.97
IDX_B04_B03	-0.004712	-0.001332	-1.37	-0.51
IDX_B05_B03	-0.011563	-0.005833	-2.71	-2.31
IDX_B05_B04	-0.010020	-0.005457	-10.74	-7.28
MEAN3x3_B03	0.000111	0.000016	0.45	0.06
MEAN3x3_B05	-0.000234	-0.000288	-2.03	-1.27
MEAN3x3_DII_B02_B03	0.130509	0.101912	25.28	14.24
MEAN3x3_NDWI	0.067761	0.067527	9.08	10.30
MEAN3x3_RATIO_B03_B02	0.011235	0.038015	0.95	2.67
RATIO_B03_B02	0.008195	0.034621	0.69	2.45
RATIO_B04_B03	-0.005144	-0.001670	-1.10	-0.29
RATIO_B05_B03	-0.011013	-0.007619	-2.95	-1.26
STD3x3_B03	0.000261	0.000283	7.43	7.22
STD3x3_B05	0.000042	0.000074	3.15	3.25
STD3x3_DII_B02_B03	0.005934	0.006199	11.97	14.14
STD3x3_NDWI	0.005776	0.002900	9.70	6.02
STD3x3_RATIO_B03_B02	0.007953	0.010974	15.25	20.18

F. Complete feature distribution boxplots

Due to the number of panels, they are intended primarily for consultation in the electronic version of the manuscript, where individual features can be examined by zooming in.

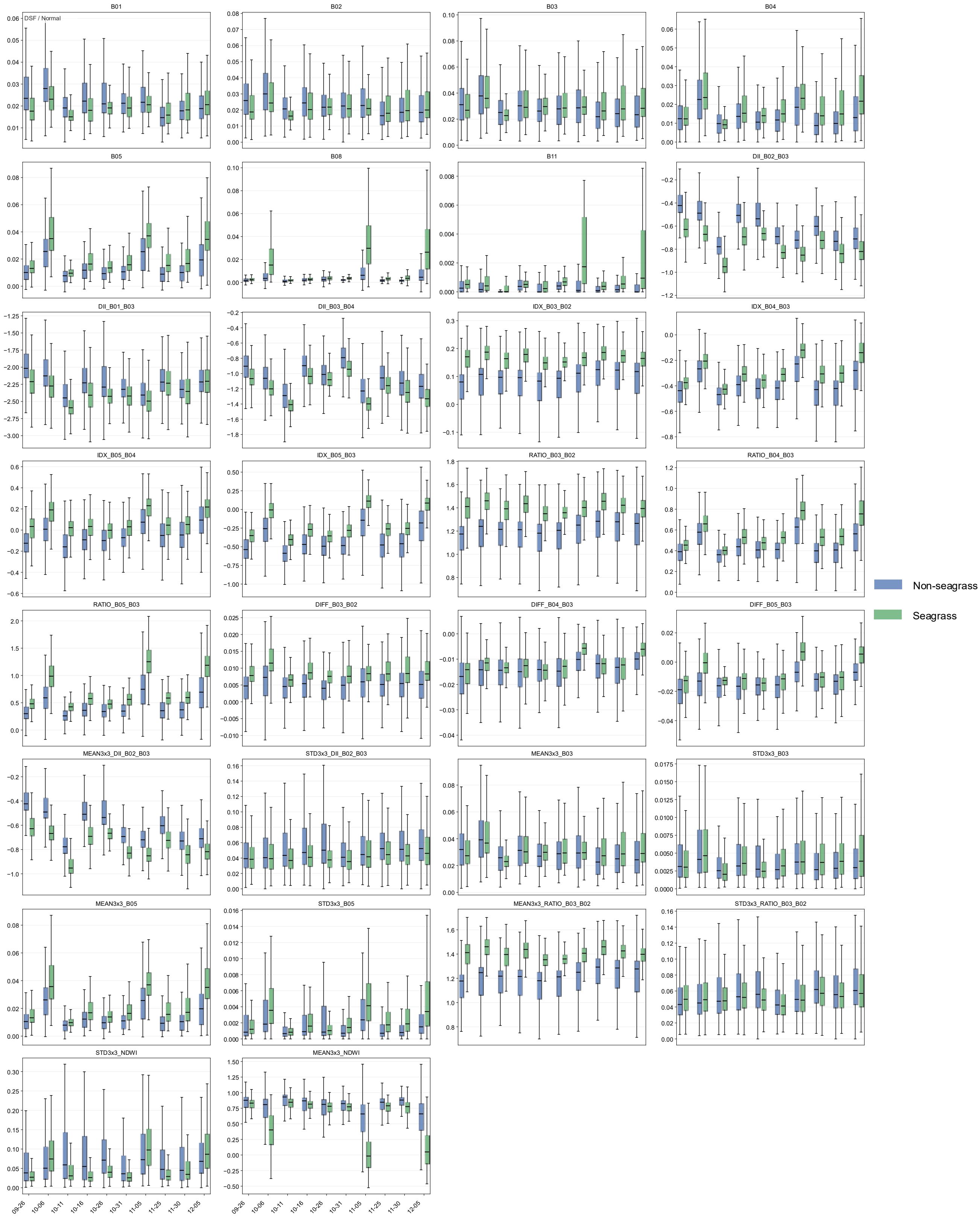

Figure 44 - Complete feature distribution boxplots for the DSF version dataset. Boxplots show the distributions of all extracted features for labelled seagrass and non-seagrass pixels across acquisition dates.

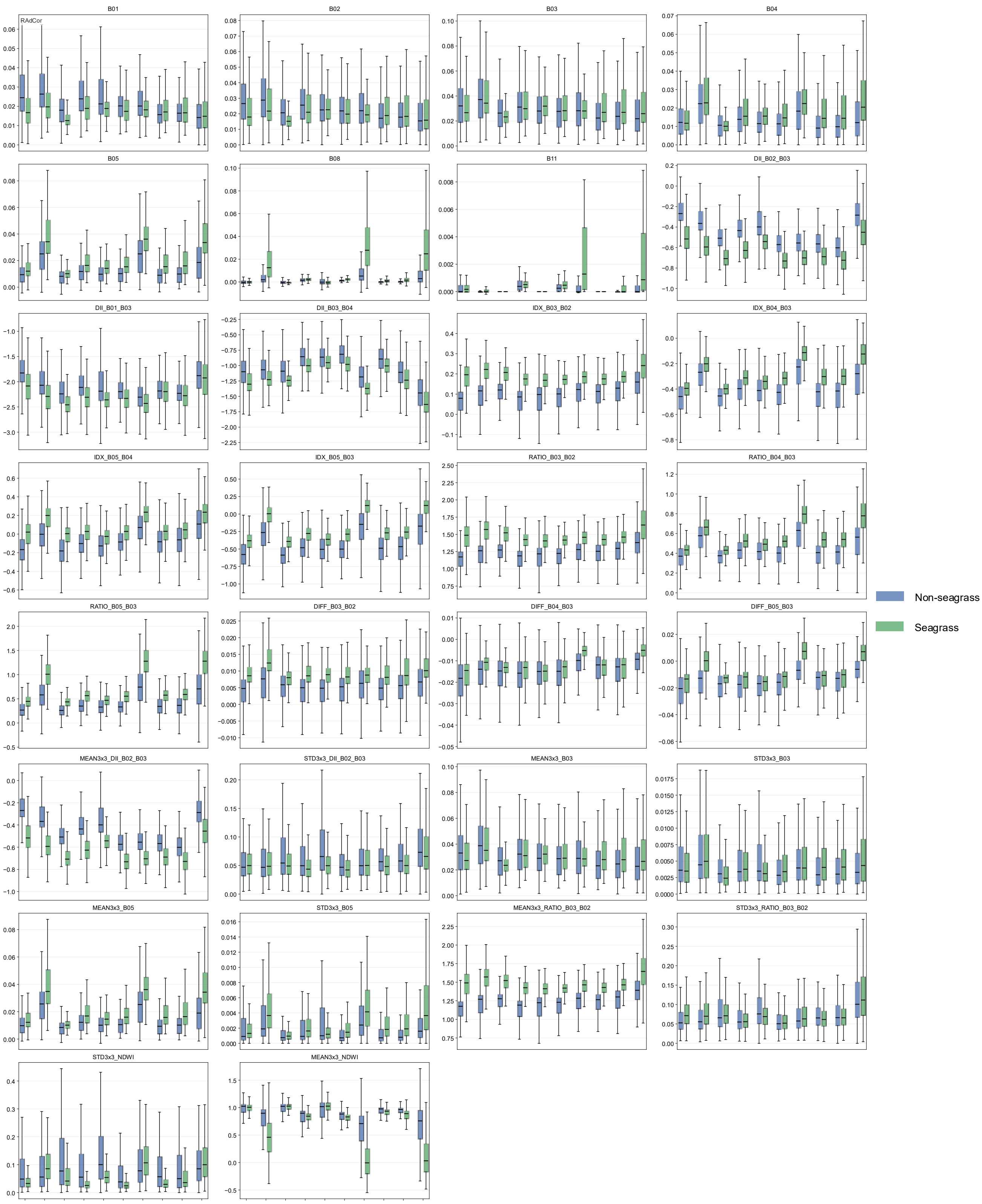

Figure 45 - Complete feature distribution boxplots for the RAdCor version dataset. Boxplots show the distributions of all extracted features for labelled seagrass and non-seagrass pixels across acquisition dates.

G. Models performance metrics and selected hyperparameters

Table 16 - Extended performance metrics for the 12 classification configurations.

Correction	Classifier	Strategy	Threshold	Macro-F1	F1 seagrass	Precision seagrass	Recall seagrass
DSF	RF	Fixed 0.5	0.500 ± 0.000	0.801 ± 0.065	0.700 ± 0.077	0.651 ± 0.157	0.812 ± 0.126
		Optimized Macro-F1	0.582 ± 0.010	0.808 ± 0.054	0.699 ± 0.066	0.701 ± 0.144	0.752 ± 0.158
		Optimized F1_1	0.563 ± 0.013	0.807 ± 0.055	0.700 ± 0.067	0.687 ± 0.147	0.768 ± 0.152
	XGBoost	Fixed 0.5	0.500 ± 0.000	0.801 ± 0.062	0.701 ± 0.073	0.651 ± 0.163	0.822 ± 0.134
		Optimized Macro-F1	0.586 ± 0.022	0.808 ± 0.048	0.703 ± 0.063	0.685 ± 0.152	0.781 ± 0.155
		Optimized F1_1	0.565 ± 0.018	0.806 ± 0.051	0.702 ± 0.064	0.679 ± 0.156	0.789 ± 0.154
RAdCor	RF	Fixed 0.5	0.500 ± 0.000	0.761 ± 0.123	0.662 ± 0.134	0.595 ± 0.201	0.834 ± 0.127
		Optimized Macro-F1	0.677 ± 0.040	0.773 ± 0.106	0.663 ± 0.124	0.645 ± 0.202	0.760 ± 0.153
		Optimized F1_1	0.643 ± 0.043	0.768 ± 0.110	0.661 ± 0.123	0.628 ± 0.199	0.783 ± 0.152
	XGBoost	Fixed 0.5	0.500 ± 0.000	0.770 ± 0.122	0.673 ± 0.131	0.611 ± 0.197	0.835 ± 0.139
		Optimized Macro-F1	0.655 ± 0.011	0.777 ± 0.102	0.669 ± 0.119	0.648 ± 0.195	0.775 ± 0.165
		Optimized F1_1	0.635 ± 0.018	0.778 ± 0.105	0.673 ± 0.121	0.644 ± 0.195	0.787 ± 0.160

Table 17 - Selected hyperparameters for the final trained Random Forest configurations.

Correction	Strategy	N estimators	Max features	Max depth	Min samples leaf	Class weight
DSF	Fixed 0.5	800	0.5	20	1	{0: 1, 1: 2}
	Macro-F1	800	sqrt	20	1	balanced
	F1_1	800	sqrt	20	1	balanced
RAdCor	Fixed 0.5	500	sqrt	20	1	{0: 1, 1: 2}
	Macro-F1	500	0.5	10	1	Balanced subsample
	F1_1	800	0.5	10	5	balanced

Table 18 - Selected hyperparameters for the final trained XGBoost configurations.

Correction	Strategy	N estimators	Max depth	Learning rate	subsample	Colsample bytree	Min child weight	gamma	Scale pos weight
DSF	Fixed 0.5	600	4	0.10	0.8	1.0	5	1	1.0
	Macro-F1	600	4	0.10	0.8	0.8	5	1	1.0
	F1_1	600	4	0.10	0.8	0.8	5	1	1.0
RAdCor	Fixed 0.5	600	8	0.05	1.0	0.8	1	0	1.0
	Macro-F1	300	8	0.05	1.0	1.0	1	0	1.0
	F1_1	300	8	0.05	1.0	1.0	1	0	1.0

H. Annual core seagrass maps from 2016 to 2026

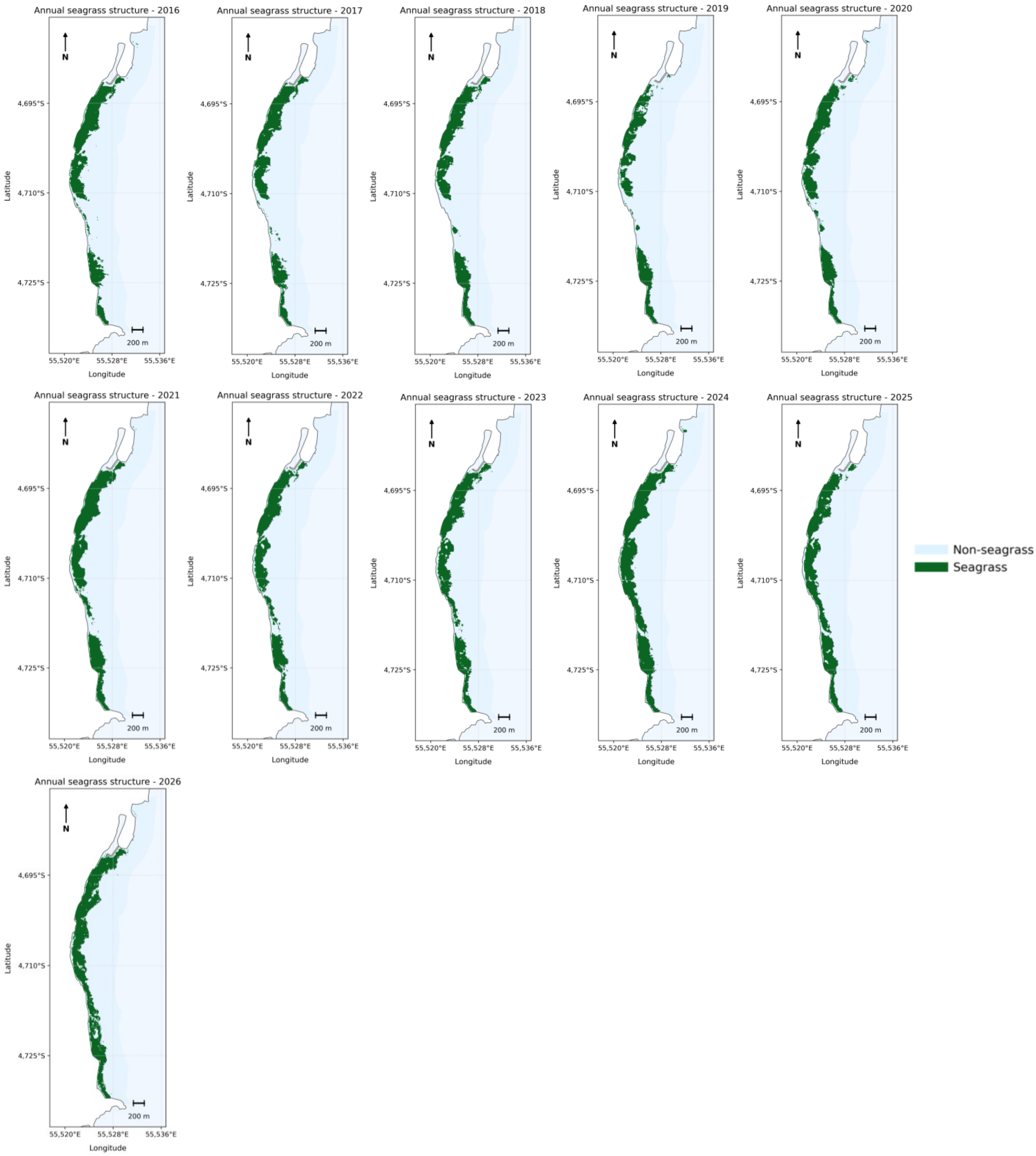

Figure 46 - Full annual series of core seagrass maps at Anse-aux-Pins from 2016 to 2026. Green pixels are annual core seagrass, light blue pixels are mapped non-seagrass. The series shows the yearly distribution of core seagrass detected with Sentinel-2 imagery. The incomplete years 2016 and 2026 should be interpreted with caution.

Mapping and monitoring seagrass meadows in Seychelles using Sentinel-2 imagery: Model training at Anse-aux-Pins and transferability to nearby lagoons

Mattis Peugeot

Seagrass meadows provide essential ecological functions, including habitat provision, sediment stabilization, carbon storage and coastal protection. In Seychelles, recent national mapping has improved knowledge of seagrass distribution, but temporal dynamics remain less documented. This thesis aimed to develop a reproducible Sentinel-2 workflow to map and monitor seagrass extent at Anse-aux-Pins, Mahé and assess its application to other reef-lagoon systems. The workflow combined Sentinel-2 preprocessing, ACOLITE correction, masking, feature extraction, classification and temporal aggregation. Several atmospheric correction, classifier and thresholding options were compared. The selected pipeline combined DSF correction, XGBoost classification and a Macro-F1 optimized threshold. It gave the best compromise between classification performance, temporal robustness and interpretability, reaching a mean Macro-F1 of 0.808 ± 0.048. Applied to the 2016-2026 archive, the workflow showed that mapped seagrass extent at Anse-aux-Pins was dynamic in space and time. The meadow did not follow a linear trend, but showed repeated phases of expansion and contraction. A clear seasonal cycle was detected, with mapped extent highest around February and lowest around September-October. Spatial outputs distinguished a persistent core, a seasonal envelope and an apparent recovery zone in the central-southern lagoon. The workflow was also applied to Sainte Anne, Côte d'Or, Grande Anse and Baie Sainte Anne. The method was technically transferable, but classifier generalization varied between sites, reflecting differences in lagoon morphology, substrate brightness, water-column conditions, tide influence and seagrass species. Overall, Sentinel-2 can give coherent indicators of mapped seagrass extent in Seychelles shallow lagoons. Broader use would mainly require multi-site and multi-season field data to improve calibration, validation and ecological meaning.

UNIVERSITÉ CATHOLIQUE DE LOUVAIN
Faculté des bioingénieurs
Croix du Sud, 2 bte L7.05.01, 1348 Louvain-La-Neuve, Belgique | www.uclouvain.be/agro